INFORMATION TO USERS

This manuscript has been reproduced from the microfilm master. UMI films the text directly from the original or copy submitted. Thus, some thesis and dissertation copies are in typewriter face, while others may be from any type of computer printer.

The quality of this reproduction is dependent upon the quality of the copy submitted. Broken or indistinct print, colored or poor quality illustrations and photographs, print bleedthrough, substandard margins, and improper alignment can adversely affect reproduction.

In the unlikely event that the author did not send UMI a complete manuscript and there are missing pages, these will be noted. Also, if unauthorized copyright material had to be removed, a note will indicate the deletion.

Oversize materials (e.g., maps, drawings, charts) are reproduced by sectioning the original, beginning at the upper left-hand corner and continuing from left to right in equal sections with small overlaps.

Photographs included in the original manuscript have been reproduced xerographically in this copy. Higher quality 6" x 9" black and white photographic prints are available for any photographs or illustrations appearing in this copy for an additional charge. Contact UMI directly to order.

A DIFFERENTIAL CARRIER-PHASE NAVIGATION SYSTEM COMBINING GPS WITH LOW EARTH ORBIT SATELLITES FOR RAPID RESOLUTION OF INTEGER CYCLE AMBIGUITIES

A DISSERTATION SUBMITTED TO THE DEPARTMENT OF ELECTRICAL ENGINEERING AND THE COMMITTEE ON GRADUATE STUDIES OF STANFORD UNIVERSITY IN PARTIAL FULFILLMENT OF THE REQUIREMENTS FOR THE DEGREE OF DOCTOR OF PHILOSOPHY

Matthew Rabinowitz

December 2000

UMI Number: 3000087

Copyright 2001 by
Rabinowitz, Matthew
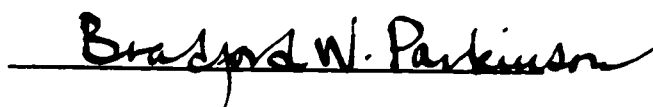
All rights reserved.

UMI®

I certify that I have read this dissertation and that, in my opinion, it is fully adequate in scope and quality as a dissertation for the degree of Doctor of Philosophy.

Bradford Parkinson

I certify that I have read this dissertation and that, in my opinion, it is fully adequate in scope and quality as a dissertation for the degree of Doctor of Philosophy.
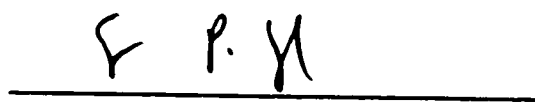
Gene Franklin

I certify that I have read this dissertation and that, in my opinion, it is fully adequate in scope and quality as a dissertation for the degree of Doctor of Philosophy.

Stephen Boyd

Approved for the University Committee on Graduate Studies:

.

Abstract

This thesis describes the theory and implementation of a high-performance navigation system which combines GPS with Low Earth Orbit Satellites (LEOS). Our objective is to rapidly acquire centimeter-level position, without placing constraints on the motion of the navigated platform. When tracking the carrier phase of satellite downlinks, the primary obstacle to accurate positioning is the resolution of cycle ambiguities, which arise since phase can only be measured modulus 2π. The rapid change in the line-of-sight vectors from the receiver to the LEO signal sources, due to the orbital motion of the LEOS, enables the robust resolution of these cycle ambiguities on the GPS signals as well as parameters related to the cycle ambiguities on the LEO signals. These parameters, once identified, enable real-time centimeter-level differential positioning of a user receiver several miles from a reference station. The technique requires no specialized navigation electronics, such as atomic oscillators, on-board the LEO satellites. As such, it can accommodate instabilities in the crystal oscillators on the satellites, multiple beam configurations of satellite links, bent-pipe communication architectures, and TDMA downlinks. A set of techniques have been developed for achieving centimeter-level navigation using pre-existent LEO transceiver hardware, designed for low cost data communication. The issues addressed include synchronization of the LEO and GPS hardware for errors below the centimeter level, precise time-tagging of carrier-phase measurements without the use of hardware accumulators

and latches, an efficient data reduction algorithm for resolving cycle ambiguities while accommodating different frequency-dependent phase-lags in the receiver front ends, and the ability to scale the number of LEOS tracked, and the number of navigation antennas used, in software. By a combination of experimentation and simulation, we describe the system performance in terms of accuracy and integrity of navigation solutions. We also describe potential advantages provided by LEO satellites for meter-level navigation in high-loss environments, or multipath-prone environments.

Acknowledgment

Contents

List of Tables

List of Figures

Chapter 1

Introduction

1.I Overview of the Problem

Conventional satellite-based positioning techniques are based on the use of special navigation signals transmitted from multiple navigational satellites. In the global positioning system (GPS), for example, a constellation of GPS satellites transmit L1 (1575MHz) and L2 (1227MHz) carrier signals modulated with C/A and P code signals. By measuring the incident phase of these code signals, a user receiver can determine its position to an accuracy of about 6 meters.

To determine the user position with higher accuracy, a differential technique can be used. A reference receiver having a known position also tracks the satellite down-links and calculates its position. The reference receiver then calculates a differential correction by comparing its known position with the calculated position, and transmits this correction to the user receiver. This differential correction suppresses errors which are correlated in the user and reference measurements, such as ionospheric and tropospheric delays, and satellite ephemeris errors. Assuming the user receiver is near the reference station, the differential correction data can improve the accuracy of its

position estimate to approximately 1 meter.

Various proposed techniques provide positioning accuracy on the order of 1 centimeter. In addition to tracking code phase, these techniques also measure the incident carrier phase of the signals from GPS navigational satellites. Typically, this carrier phase positioning technique uses differential carrier phase correction data from a reference station in order to improve performance. There is, however, a difficulty inherent to this technique since phase can only be measured modulus 2π. When tracking a carrier signal of a navigational satellite transmission, one can precisely measure the phase of the signal, but one cannot determine by direct measurement how many complete integer cycles have elapsed between the times of signal emission and reception. The measured carrier signal thus has an inherent *integer cycle ambiguity* which must be resolved in order to use the carrier phase measurements for positioning. Consequently, much research in the art of satellite-based positioning has focused on resolving these cycle ambiguities in carrier phase measurements from satellite signals.

1.II   Prior Research

MacDoran and Spitzmesser [42] describe a method for deriving pseudoranges to GPS satellites by successively resolving integers for higher and higher signal frequencies with measurements independent of the integers being resolved. The first measurement resolves the number of C/A code cycles; these integers provide for independent measurements to resolve the number of P code cycles, and so on for the L2 and L1 carrier cycles. This technique, however, assumes exact correlation between satellite and user frequency standards (i.e., the user requires an atomic clock), and provides

2

no means of correcting for atmospheric distortions.

A similar technique, called dual-frequency wide-laning, involves multiplying and filtering the L2 and L1 signals from a GPS satellite. This process produces a beat signal of nominal wavelength 86 *cm*, which is longer than either that of the L1 signal (19 *cm*) or the L2 signal (24 *cm*). Integer ambiguities are then resolved on this longer wavelength signal. These dual frequency techniques still have inherently low integrity. This is because there are typically many combinations of integer ambiguities which will accommodate a given set of observations. With the noise inherent to wide-laning range measurements, it is difficult to resolve the correct integer set without substantial change in the line of site vector between the receiver and the satellites. Nonetheless, these techniques are receiving more attention with the anticipated augmentation of GPS to three civilian frequencies. This will, to some extent, improve the integrity of wide-laning techniques [24].

Hatch [45] described a technique for resolving integer ambiguities using measurements from redundant GPS satellites. Initial carrier-phase data is collected from the minimum number of GPS satellites needed to resolve the relative position between two antennas. From these measurements, a set of all possible integer combinations is derived. Using carrier phase measurements from an additional GPS satellite, the unlikely integer combinations are systematically eliminated. This technique is suited to the context of attitude determination where both receivers use the same frequency standard and the distance between the antennas is fixed. This approach, however, is ill-adapted for positioning over large displacements, where the initial set of satellites is four and the distance between the receivers is not known *a priori* - the technique is then extremely susceptible to noise, and computationally intensive. Knight [12] details an approach similar to that of Hatch, except that a more efficient technique is

derived for eliminating unlikely integer combinations from the feasible set. Knight's technique also assumes that the two receivers are on the same clock standard.

Counselman [7] discloses a technique for GPS positioning that does not resolve integer cycle ambiguities but rather finds the baseline vector between two fixed antennas by searching the space of possible baseline vectors. The antennas track the GPS satellite signals for a period of roughly 30 minutes. The baseline is selected that best accounts for the phase changes observed with the motion of the GPS satellites. This technique, however, assumes that the baseline vector remains constant over the course of all the measurements during the 30 minute interval, and is therefore only suitable for surveying applications. Moreover, it also assumes that the clock offset between user and reference receivers remains constant over the measurement interval.

A motion-based method for aircraft attitude determination has been described by Cohen [10]. This method involves placing antennas on the aircraft wings and tail, as well as a reference antenna on the fuselage. The integer ambiguities between the antennas can be rapidly resolved as the changes in aircraft attitude alter the antenna geometry relative to the GPS satellite locations. This approach, however, is limited to attitude determination and is not suitable for precise absolute positioning of the aircraft itself.

Current state-of-the art kinematic carrier phase GPS navigation systems for absolute positioning have been described by Cohen [15, 17, 16, 14] and by Pervan [8, 5]. These systems achieve rapid resolution of cycle ambiguities using ground-based navigational pseudo satellites (pseudolites) which transmit either an additional ranging signal (Doppler Marker) or a signal in phase with one of the satellites (Synchrolites). These techniques achieve robust resolution of cycle ambiguities due to the *geometric*

diversity provided by the pseudolites, or the rapid change in the line-of-site vectors from the receiver to the signal sources. Consequently, the approach can only achieve rapid, accurate positioning when the navigated platform moves nearby the ground-based pseudolites. Besides placing these constraints on the motion of the user, the ground-based infrastructure of pseudolites on which this technique depends is costly to maintain.

Therefore, each of the existing techniques for satellite-based navigation suffers from one or more of the following drawbacks: (a) it does not provide centimeter-level accuracy, (b) it does not quickly resolve integer cycle ambiguities, (c) it is not suitable for kinematic applications, (d) it provides only attitude information and does not provide absolute position information, (e) it does not have high integrity, (f) it requires the deployment and maintenance of substantial ground-based infrastructure, (g) its performance is limited to users in a small geographical area near pseudolites, or (h) it requires the user receiver and/or the reference receiver to have an expensive highly stable oscillator.

In view of the above, it is a goal of this dissertation to describe a system for *centimeter*-level kinematic positioning with rapid acquisition times and high integrity, and which does not suffer from any of the drawbacks (a)-(h) listed above. In order to obtain high-integrity estimation of integer cycle ambiguities, carrier-phase measurements must be made for a time interval long enough that the direction vectors between the user and the signal sources undergo substantial change. The time required to acquire precise position can be considerably reduced by using the signals from low earth orbit satellites (LEOS), which are not necessarily intended for navigational use. The short orbital periods of these LEOS rapidly provide the required change in geometry for resolution of cycle ambiguities with high reliability. In the preferred embodiment

5

of the system, an initial estimate of the user position and clock offset is provided by conventional code-phase differential GPS techniques. However the methodology is not in general limited to augmenting GPS. In fact, with enough LEOS one can achieve a stand-alone system independent of the Global Position System.

Chapter 2

System Overview

2.I General System Concept

An overview of the joint GPS/LEO system [34, 35, 19, 33, 32] is presented in Figure 2.1. The user and reference receivers track the incident phase of the LEO and GPS signals. In addition, the reference receives up-to-date ephemeris information from
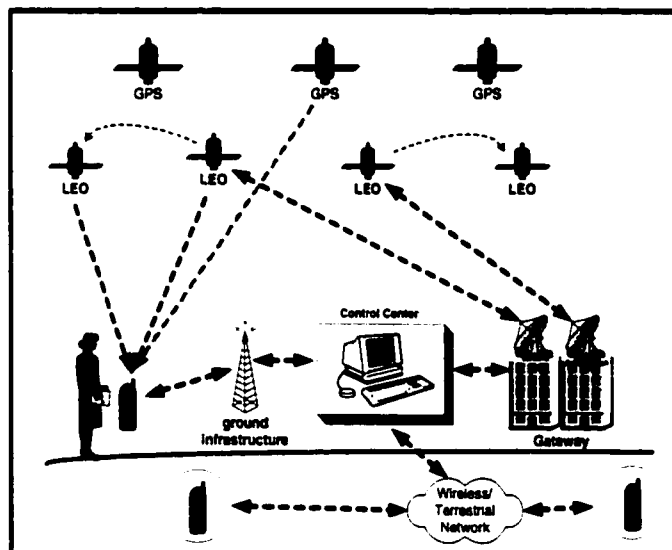
Figure 2.1: Architectural overview of the LEO concept

7

the relevant satellites[1]. The reference information is conveyed to a control center where the differential corrections, and other navigational aids, are computed. This differential data is conveyed to the user receiver[2] via a satellite data channel, or via terrestrial infrastructure. Thus far, only a terrestrial data connection has been employed. By using reference code or carrier prediction techniques, the data channel need be active in bursts, at most every 5 seconds, where each burst conveys under 1 Kbit of data.

For precision navigation, the receivers track the absolute carrier phase of the LEO and GPS signal. The geometric diversity achieved primarily by the motion of the LEOS enables the user receiver to resolve the integer cycle ambiguities on the GPS satellite signals as well as parameters related to the cycle ambiguities on the LEO signals, and consequently to position itself with centimeter-level accuracy in the absence of multipath. In most applications, however, centimeter-level accuracy is redundant, and multipath dominates the noise equation. If the LEO is transmitting a Code-Division-Multiple-Access (CDMA) signal, as in the case of Globalstar, that signal can be used to position the user, even when GPS is not available, such as for high-loss indoor environments. Ideally, a receiver would track at least 2 LEO satellites, 100% of the time. We will focus our attention on Orbcomm and Globalstar, which are the only constellations currently in operation.

2.II   Embodiment of the Precision Navigation Method

We describe below the steps involved in the general navigation technique. It will also be clear from the ensuing description how these steps would be adjusted for a static

---

[1]Most LEOS have on-board GPS receivers - see table 8.1

[2]Or to the point, such as a cellular base-station, where user position is computed

user, or an attitude determination problem where user and reference receivers are driven by a common oscillator and are separated by a baseline of constant magnitude.

- The reference and user receivers obtain up-to-date satellite ephemeris information for both GPS and LEO satellites.

- Both reference and user receiver measure the code phase delay on the signals transmitted by the GPS satellites. This measurement is known as the raw pseudorange.

- Based on the code phase measurement, the user and reference correlate their clocks to within 1 μsec of GPS time [41].

- In a preferred embodiment, the reference receiver calculates differential corrections for the code-phase measurements and conveys them to the user receiver over a real-time communication link. The user receiver then positions itself with meter-level accuracy relative to the reference receiver using the differentially corrected code-phase measurements.

- The user and reference receiver simultaneously track the absolute carrier phase of GPS satellite signals and LEO satellite signals.

- If necessary, the reference receiver calibrates the LEO satellite oscillators using the technique described in Section 6.III.

- The reference receiver conveys to the user its carrier phase measurements and measurement correction data.

- The user corrects for deterministic errors in the carrier phase measurement. These are second order phase errors which are not compensated for in the differential correction - see Sections 4.I, 6.II, 6.III, 9.I

9

- The user employs the data-reduction technique described in Section (4.II) to identify the integer cycle ambiguities on the GPS satellites signals, and parameters related to the integer cycle ambiguities on the LEOS signals. The technique described also involves analyzing the integrity with which these parameters can be computed. In this way, we protect for cases in which LEO/GPS geometry is not sufficient for precise positioning.

- Once these parameters are identified, the user receiver can be positioned in real-time, with centimeter-level accuracy relative to the reference receiver.

2.III   Various Implementations of System Data Links

The methods by which data is transferred in the system are, of course, application dependent. However, as part of the general overview, we will discuss some approaches to realizing the primary data links.

2.III.A   The Link from Reference to User (LRU)

For a mobile user, the differential data link from reference to user is best implemented with a real-time radio connection. For an attitude determination problem, the LRU can be implemented with a real-time cable connection, and for static surveying applications, the LRU could be off-line. For the mobile user the most efficient LRU implementation uses the same basic frequency and modulation scheme of either the GPS signals, or the LEO satellite signals[3]. In this way, existing receiver front-end hardware - as described later in Figure 3.1 - can be used for the LRU.

---

[3]This assumes that some multiple-access scheme such as CMDA, TDMA, FDMA facilitates the additional data channel

The radio LRU can be implemented by transmitting a signal directly to the user via a reference station transmitter, or by using an existing LEO satellite data link. The central function of the LRU, which determines the necessary data rates, is to convey carrier phase measurements made at the reference station to the user. If the user receiver knows the location of the reference station, it is able to accurately predict the phase measurements that the reference receiver will make for up to several seconds[4]. Consequently, the LRU needs to be active every few seconds, for bursts of roughly 10ms (assuming 9600 baud) over the duration of navigation. In addition to the carrier phase information, the LRU can convey to the user the following information:

- The satellite ephemerides. This would be necessary for an implementation where the ephemerides are not known to the user, and cannot be obtained by a directly broadcast satellite data link.

- An estimate of the reference receiver's clock offset. This can be used to correct the differential measurement as described in Section 4.I.

- Differential corrections for code-phase measurement. In order to achieve an initial differential position estimate which is accurate to within meters, the reference would send to the user a set of corrections for the range measurements to improve the code phase performance of GPS. The technique of deriving these corrections is well understood [40].

- The position of the reference station antenna phase center. The user receiver finds the centimeter-level position between its antenna and the reference receiver antenna. Therefore, the universal accuracy of the user's derived position

---

[4]The prediction interval could be as long as 3 seconds for centimeter-level performance when Selective Availability (S/A) was active on the GPS signals. Without S/A, the prediction interval will be considerably longer.

11

depends on the accuracy of the reference antenna position information. In addition, data reduction techniques which correct for deterministic errors caused by certain LEO systems architectures, depend upon the user knowing the rough location of the reference station antenna.

- Status information on the satellites. The reference station can also send the user information about the health and signal characteristics of each of the satellites being tracked.

- Error correction information. This information is employed by the user to minimize residual errors of differential phase measurement, or second order effects which can be modeled deterministically, for example those due to ionospheric and tropospheric delays, severe satellite oscillator instabilities, and Doppler effects between a ground-up-link station and the satellite in a bent-pipe architecture.

2.III.B   Communicating the LEO Satellite Ephemerides

The navigation capability of the system hinges on the user knowing the location of the LEO signal sources to reasonably high accuracy - see Section 8.IV. There are two general approaches to obtaining the satellite position as a function of time. The first approach uses a set of ephemeris parameters which characterize the satellite's orbit, and changes to that orbit over time. The canonical format for this information is the *Keplarian Two Line Elements* (TLEs). Using orbit-prediction software, the location of the satellite can be predicted several days into the future. The TLE format, and the orbital prediction software written for our experimental work are briefly discussed in Appendix B. TLEs can be updated daily over the Internet from Norad or other

tracking centers. For example, automatic down-loads can be arranged from sites such as *http://oig1.gsfc.nasa.gov*. Although this technique was used in experiments with the Transit satellites, the accuracy of the method is ill-suited to centimeter-level navigation when user-reference baselines are longer than a few hundred meters. The second approach, as used by the Navstar Satellites and the Orbcomm Satellites, is the communication from the satellite in real-time of satellite positions, or a set of parameters modeling the satellite position as a function of time, which are valid for a single satellite pass. This preferred technique was applied in experiments with the Orbcomm satellites, as detailed in Section 9.
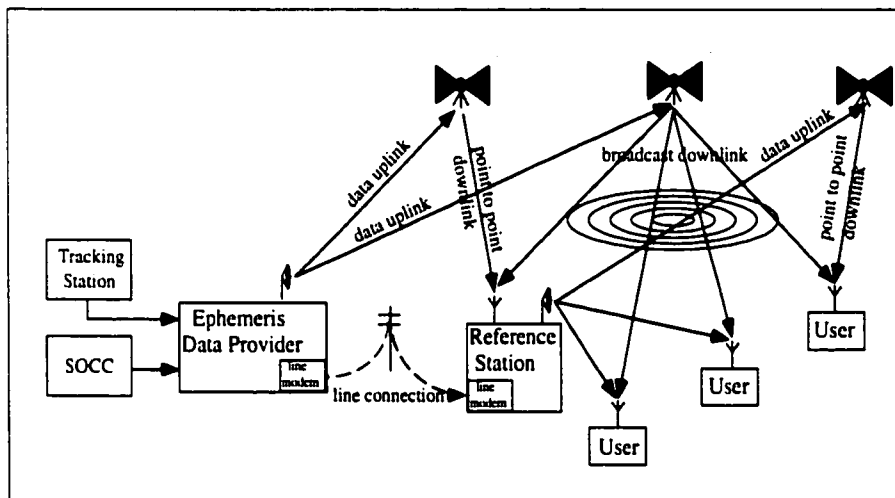
Figure 2.2: Various approaches to communicating the LEO satellite position to the user. Any sequence of arrows from the SOCC or tracking station to the user is a viable approach.

Figure 2.2 displays the different mechanisms by which the satellite position or ephemeris data may be conveyed to the user. Any sequence of arrows leading from the satellite operations and control center (SOCC), or tracking station, to the user is possible. The position sensing for the ephemeris data can be achieved either by position sensors on the satellites - such as GPS receivers which are present on Orbcomm

13

and Globalstar Satellites - or by a tracking station processing Doppler information from ground receivers at surveyed locations to calculate the LEOS' orbital parameters. Whether the information is attained from the SOCC, or from a separate tracking station, the data is conveyed to an ephemeris data provider which makes the information accessible to the user. A simple implementation connects the reference to the ephemeris provider via line modems over a regular land telephone line or using the Internet backbone. Alternatively, the information can be obtained by the reference over a LEO satellite data link, as we describe for Orbcomm in Section 9. The reference would then convey this information to the user via the LRU. Another embodiment has the LEO satellite broadcasting ephemeris data on a dedicated broadcast channel which is received by both the reference and the user. The techniques for deriving ephemeris data from satellite position sensors, or from Doppler-tracking satellites, are well understood, as are the implementations of these different methods for conveying that information to the user.

Chapter 3

Description of the LEO Navigation Receiver

Before exploring hardware details, we will consider a generic architecture for the combined GPS/LEO navigation receiver. Figure 3.1 illustrates the block-wise components for a reference or user receiver, assuming that transmissions are receivable from the Navstar Constellation (N) as well as LEO constellations (L_1, L_2, L_3). Only one LEO constellation is necessary for the system, however three are assumed in this diagram to illustrate the scalable nature of the concept. While the overall structure of this receiver is fairly generic, the individual modules identified in Figure 3.1 can be implemented in a variety of ways, depending on size, performance, and budgetary constraints. We will touch upon some of these issues in the discussion that follows.

3.I Antenna Subsystem

The antenna subsystem must be resonant at the downlink bands of each constellation being tracked. In our description of the data reduction technique (Section 4.I), we assume that this subsystem consists of a single antenna which is resonant at the
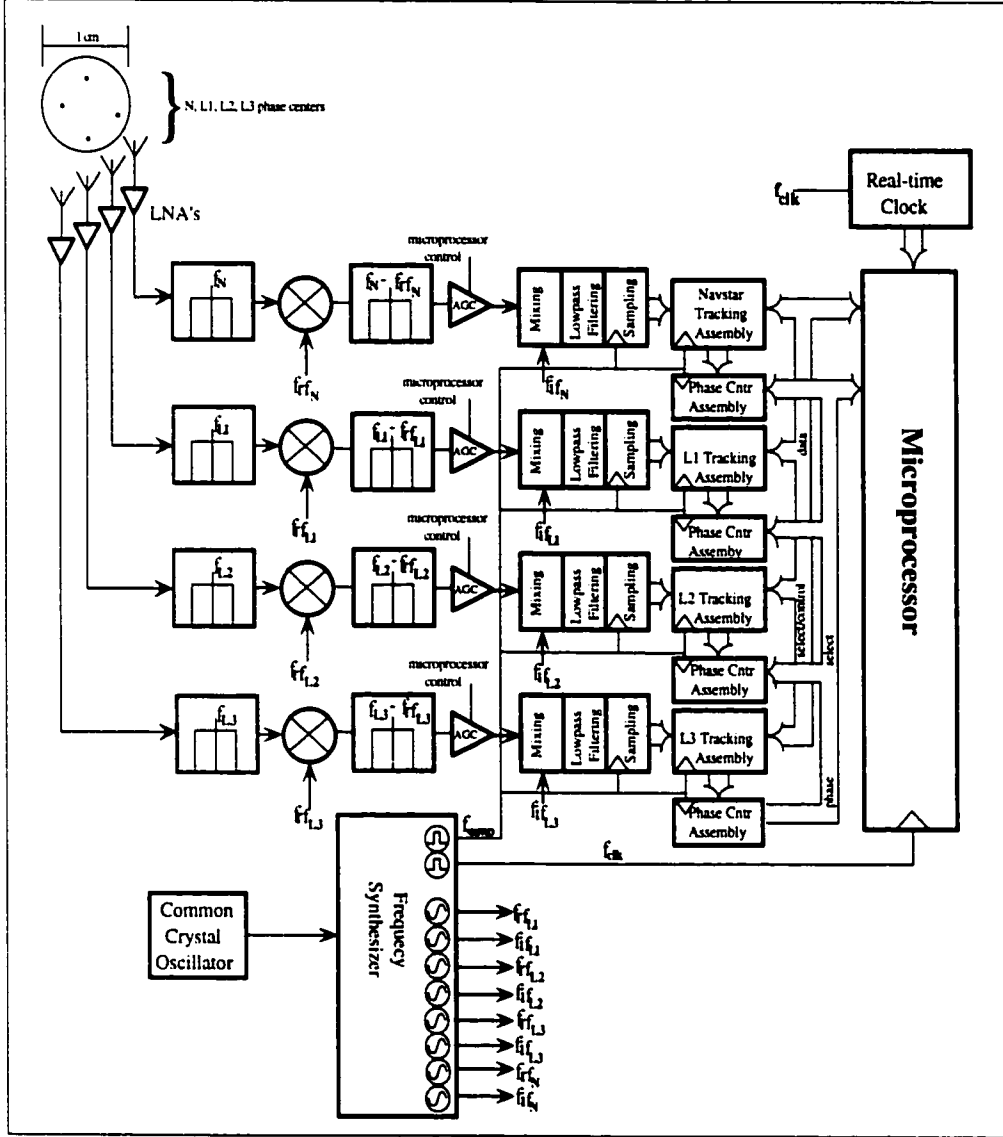
Figure 3.1: Block architecture of a generic user or reference receiver, tracking GPS and three LEO constellations

relevant frequencies and has phase centers for the respective bands which may be treated as co-located (see for example [31], [55]). This assumption, however, is not essential to the system. The design of such an antenna would present a substantial challenge for frequency ranges from UHF to S-band. In fact, in order for a phase-center to be stationary as satellites traverse the sky, the gain pattern of an antenna

16

must be perfectly semi-hemispherical. The underlying model of a microstrip antenna, based on a pair of resonant cavities at each end of the patch [4, 43], indicates why such a gain pattern is infeasible. Although the errors resulting from phase-center drift are not large for $L1$ band, the effect will cause errors $> 1cm$ for UHF frequencies. Consequently, this issue is significant for centimeter-level applications. In Section 9.I we detail an experimental technique by which this effect is measured.

In situations where the orientations of the user and reference antenna subsystems are substantially different, and where the phase centers are separated, or change with satellite angle, the resultant phase effects need to be removed from the data. Since the effects can be deterministically modeled, software can correct the carrier phase measurements - see Equation (4.4) - to take this separation into account. This involves either assuming an orientation of the antenna subsystem, or for attitude-determination problems, iteratively making the correction based on the estimated orientation of the vehicle on which the antenna subsystem is mounted. If the antenna is symmetrically fed, as in Section 9.I, the effect may be modeled as a function of elevation angle, θ, and not of azimuth angle, ϕ, hence simplifying the correction.

The technique of correcting phase in software requires that the change in phase-center with satellite elevation angle, θ, be deterministic[1]. In general, the phase center of a patch antenna tends to drift in an unpredictable way as the higher-order modes of the antenna are excited. Experimentally, it is found that these modes can be largely suppressed by feeding an antenna symmetrically with multiple feeds, and maintaining the perfect geometry (square or circular) of the patch.

Figure 3.2 illustrates the design of a stacked patch antenna, resonant at 400MHz

---

[1]Within, of course, the limits of multipath, which is often the dominant effect.
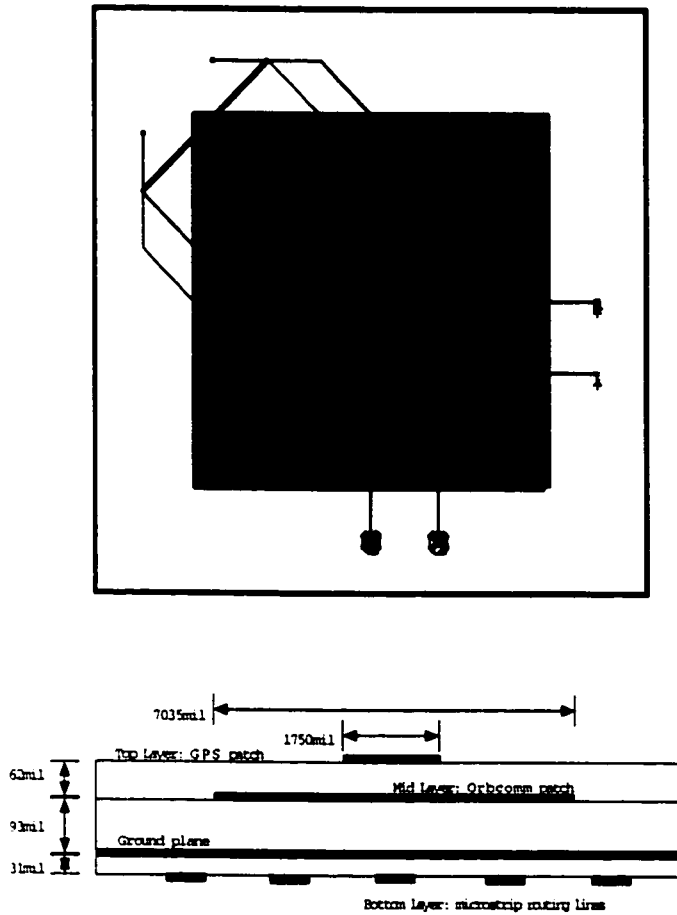
Figure 3.2: Stacked patch antenna design for tracking GPS together with a UHF circularly polarized signal. The upper patch resonates at 1.575GHz, the lower at 400MHz. Notice that each patch is fed with a quadrature hybrid power combiner, and quarter-wave impedance transformers are used to match 50 Ohms to input impedance of the patch edges. The phase centers for the two bands are relatively closely spaced in this design.

and 1575MHZ. Notice that the upper patch (L1) uses the lower patch (UHF) as a resonant ground plane. The antenna uses quarter-wave impedance transformers to match the 50 Ohm line to the impedance seen at the edge of the patch, without insetting the feed points and ruining the resonant cavity geometry. In addition, a quarter-wave junction power splitter (combiner) is used since this shifts the relative phase of the two signal path by 90° and enables circular polarization of the antenna.

18

This antenna achieves relatively close spacing between the phase centers of the UHF and L1 bands, so that the *similar orientation* assumption for the user and reference antennas can be made. While this was constructed in the lab, it was not fabricated for the experimental work due to budgetary constraints.

3.II   Receiver Hardware

3.II.A   Overview of Receiver Architecture

We will consider, in general terms, the signal path in our receiver if Figure 3.1 for one of the LEO constellations, L1. The total signal amplification by the receiver is on the order of 120dB, spread over gain at high, intermediate and low frequencies. A crucial component which largely determines the receivers noise figure [29], is the Low Noise Amplifier LNA at the antenna output. This should not have a noise figure exceeding 3.0dB. The discussion that follows will indicate some noise figures which were achieved experimentally. The LNA output is bandpass filtered and then down-converted by mixing with a locally generated Radio Frequency (rf), $f_{rf_{L1}}$. Note that all local oscillator signals, whether for mixing analogue signals or clocking digital phase tracking hardware, are tied to a single crystal oscillator. An intermediate frequency (if) bandpass filter (and amplifier) at the mixer output remove the unwanted upper sideband. A microprocessor- controlled Automatic Gain Control (AGC) then adjusts the magnitude of the signal to achieve optimal use of the available sampling bits. There are situations where this adjustable gain is redundant. For example, when a signal is hidden in bandpass noise of substantially larger power, such as arises with spread spectrum modulation methods, the SNR forfeited by sampling with one bit is roughly 1.96dB [26]. Alternatively, if the signal is sampled with 8 bits or more,

the large dynamic range of the sampler typically renders the AGC redundant. A common variation on this architecture is to place a low noise AGC at the input to the rf bandpass filter to substitute for the LNA.

The if signal enters a mixing stage, followed by a filtering stage and a sampling stage. The exact means of implementing the down-converting, filtering and sampling the signal at the if stage varies substantially with the signal structure and designer's preference. Figures 3.3a and 3.3b illustrate two general architectures for these processes. Both of these schemes would be possible for Binary-Phase-Shift-Keyed (BPSK) and Quadrature-Phase-Shift-Keyed (QPSK) signals. In the scheme of Figure 3.3a, only a single mixer and filter are used, and the sampling Section outputs a single sample. Since the tracking assemblies vary substantially for different signal structures, we will discuss these blocks in the context of particular satellite downlinks.
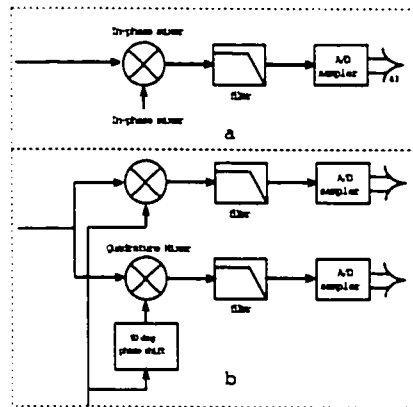
Figure 3.3: Two generic if mixing, filtering, sampling architectures

3.II.B   Design of Receiver Hardware - MarkI: Transit

Figure 3.4 displays the *Mark I* hardware which was implemented for tracking the Transit satellites of the old Navy Navigation Satellite System. Although the sys-
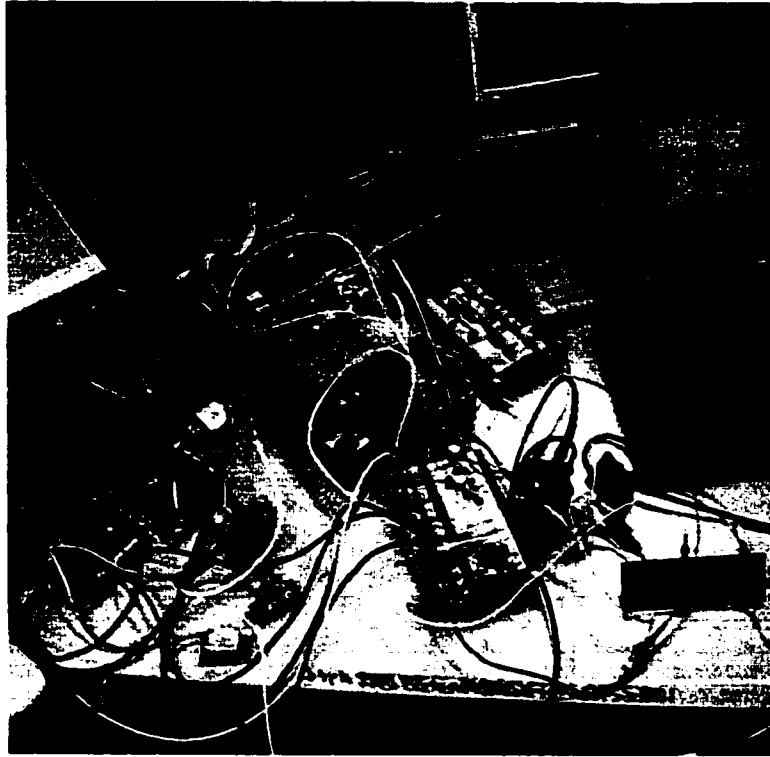
Figure 3.4: Receiver hardware, *Mark I*, designed for Transit satellite downlink. Both user and reference receivers are shown.

tem had been officially retired at the time of this research, the satellites were being operated by the Department of Electrical Engineering at the University of Texas at Austin, as part of an ionospheric research project. The downlink frequencies used by these satellites are similar to those used by a host of *Little LEO* constellations. The band was allocated for mobile satellite services by the World Administrative Radio Conference in February 1992. Consequently, a long-term approach was adopted. Much of the rf circuitry was designed at the component level, rather than using off-the-shelf subsystems[2], laying foundations for the construction of a pc-board receiver that tracks commercial LEO systems. A discussion of this hardware design as well as

---

[2]This was also motivated by budgetary constraints.

21

some salient details of the Transit downlink is placed in Appendix A. Discussion of the pc-board design of the Mark II hardware follows.

3.II.C   Design of the Receiver Hardware - Mark II: Orbcomm

Applying the lessons of Mark I, the hardware for Orbcomm was re-designed to fit onto a single pc-board, so that the joint GPS-LEO receiver could be co-located in a single rf-shielded $20cm \times 12cm \times 10cm$ box. Figure 3.5 shows the Mark II hardware for tracking the 400 MHz UHF downlink of the Orbcomm satellites. The combined GPS-LEO receiver, with the microprocessor on a separate board, is illustrated in Figure 3.6.

Figure 3.7 illustrates the components for the rf amplification and mixing circuitry. Note that this circuitry - shown at the bottom left of Figure 3.5 - is laid out to achieve the shortest possible distance for all rf lines. The width of the rf strip-lines is also set to achieve 50Ω impedance matching. Before being input to the MAN-1LN amplifier (of noise figure 3.1dB and gain 28dB), the antenna output is amplified by an LNA (of noise figure 2.2dB and gain 14dB), and then bandpass filtered to avoid *noise aliasing*. The SM4T mixer has a noise figure of roughly $8dB$, and a conversion loss of only 6.5dB, so long as the local oscillator input is adjusted to a power of 10dBm, which is achieved by applying a power divider to the output of the VCO of Figure 3.8. The resultant noise figure for the receiver front end is 2.5dB.

The frequency generation for the receiver is achieved using a Mitel SP8852 Parallel Load Synthesizer, the circuitry for which is illustrated in Figure 3.8. The frequency plan for the Orbcomm receiver is plotted in Figure 3.9. The reference frequency, f_{REF}, for the synthesis circuitry is sourced from the GPS receiver, and is buffered as

22
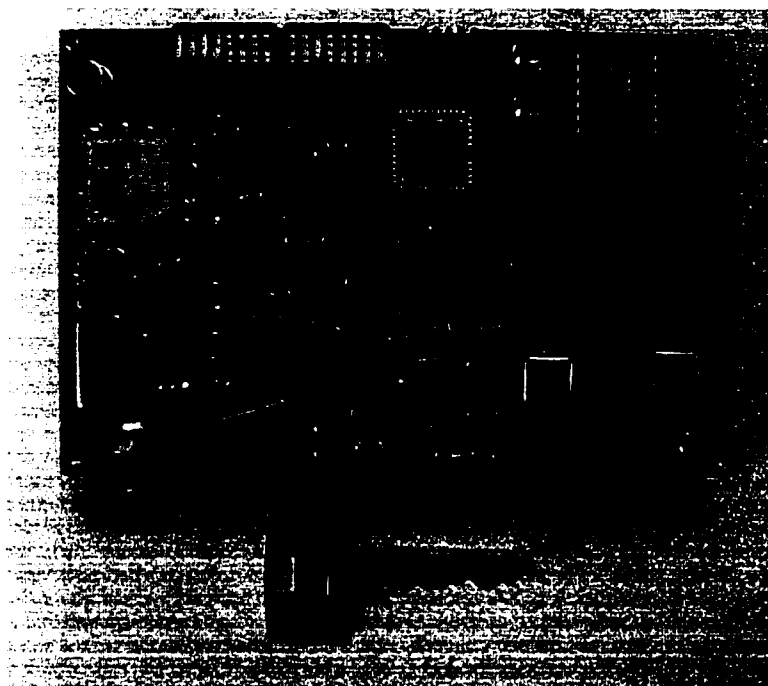
Figure 3.5: Mark II - Receiver hardware for tracking GPS together with the Orbcomm downlink. The board is designed for co-location with a GPS receiver in a single box. The various Sections of the board include digital synchronization circuitry, high-frequency filtering and amplification, intermediate frequency circuitry, signal mixing section, programmable frequency synthesis circuitry, tunable low frequency gain and filtering section

shown in Figure 3.10. The SP8852 is an integer-N synthesizer [29]; consequently the synthesized frequency is related to the reference frequency by

$$f_{VCO} = \frac{8M + A}{B} f_{REF} \tag{3.1}$$

where B is the reference divide ratio, and M, A determine the division ratio for f_{VCO} before the signal is input to the phase comparator. Obtaining a clean mixing tone is a challenge with this scheme, since the output of the VCO is modulated

23
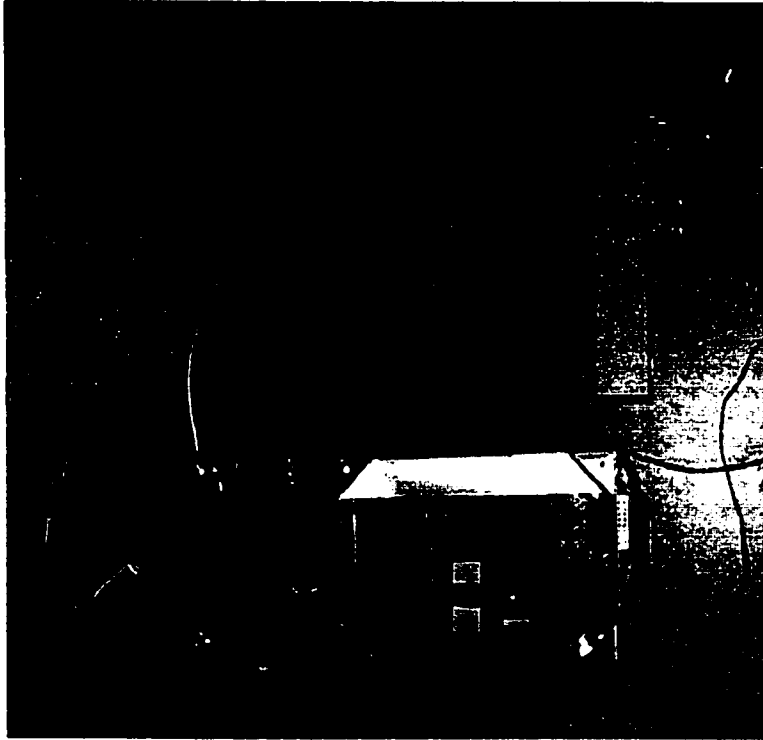
Figure 3.6: A single user or reference receiver, which tracks the Orbcomm satellites together with GPS. A Trimble Galileo II chipset is used for GPS segment. Notice that the LEO microprocessor, a TMS320, is placed on a separate board, and is driven by timing signals and interrupts generated by the digital synchronization hardware.

by the control voltage ripple of frequency $\frac{f_{REF}}{B}$. If the sidebands carry too much power, they will mix into the signal bands a host of interference signals which exist close to 400MHz. The solutions are three-fold. Firstly, a combination of integers, B, M and A are selected such that B is as small as possible, while preserving the necessary accuracy of f_{VCO}. Secondly, the bandwidth of the synthesizer phase-locked-loop (PLL) must be made as small as possible, while retaining robustness to audio-frequency disturbance. The PLL analog control is implemented using the OP37 and tuned using FC1, FC2 and FR1; roughly 20 KHz bandwidth was selected. Thirdly, extensive capacitative coupling to ground is used to ensure that the signal entering the phase comparator is decoupled from the output of the VCO. A plot of the resultant

24
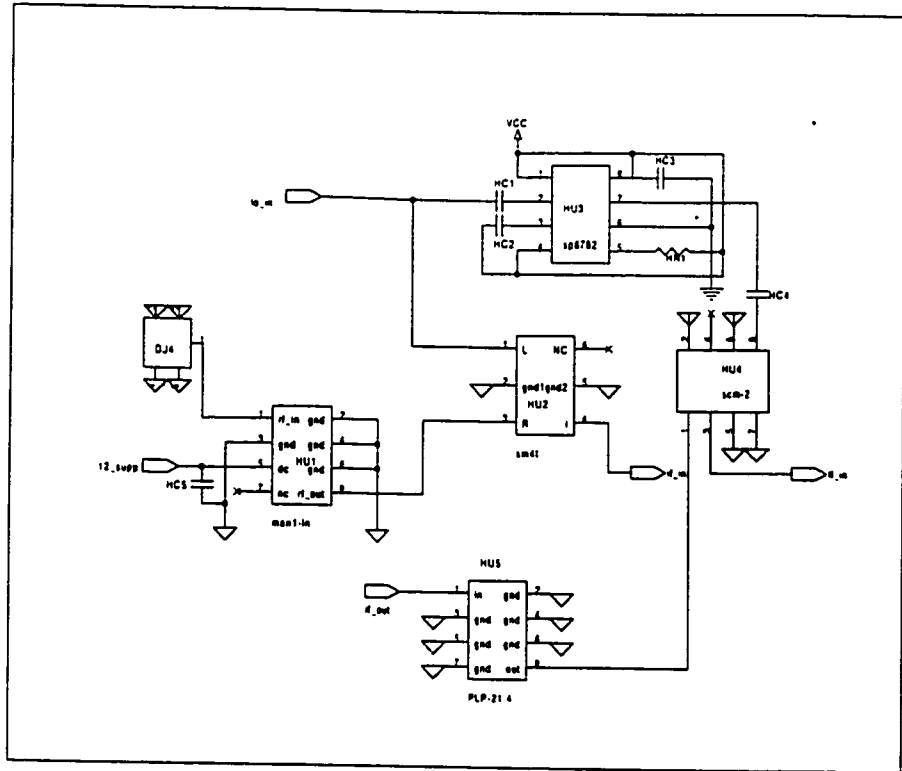
Figure 3.7: rf amplification, and mixing circuitry for the Orbcomm receiver

output of the VCO is shown in Figure 3.11.

Active filtering is combined with amplification for the intermediate frequency (Figure 3.13) and low-frequency (Figure 3.14) circuitry. The synthesizer was made programmable and the low-frequency circuitry tunable so that the receiver front end can accommodate a host of signals generated by Little LEO constellations. Tuning is also necessary to avoid interference signals which can disrupt acquisition of the of the satellite signal as described in Section 7.II. Figure 3.12 illustrates the interference signals output from the receiver front end, when the low-frequency filters are tuned to a central frequency of 500kHz, and a 3dB bandwidth of 10kHz.

The digital synchronization circuitry of Figure 3.10 has three primary tasks
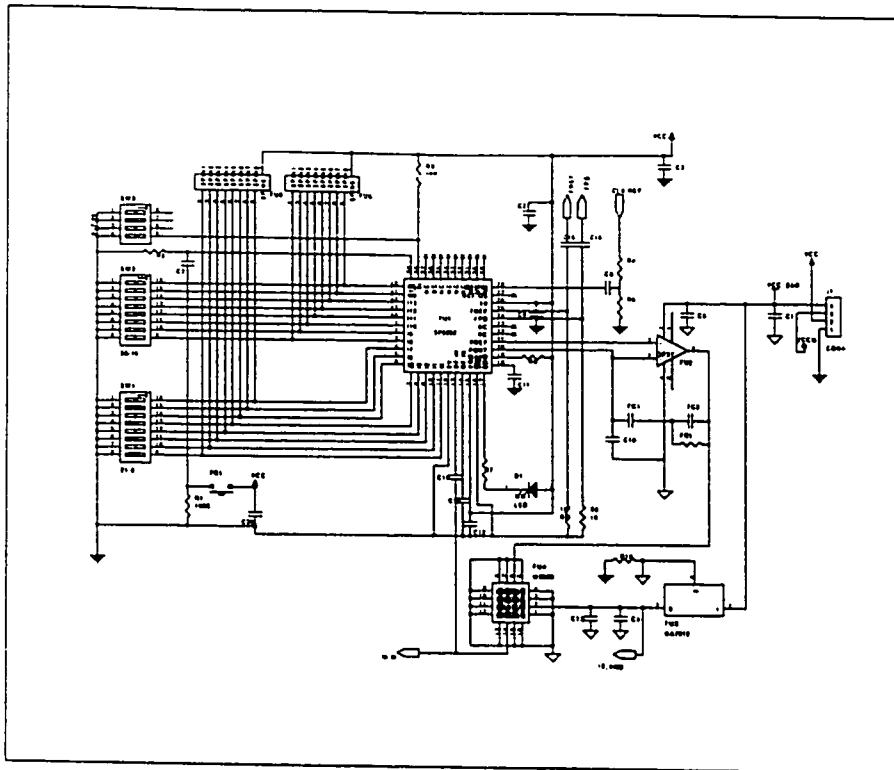
Figure 3.8: Frequency synthesis circuitry for the Orbcomm receiver
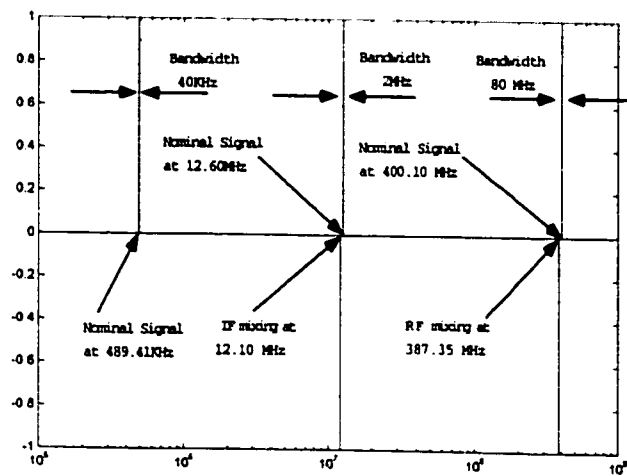
Figure 3.9: Frequency plan for the Orbcomm receiver
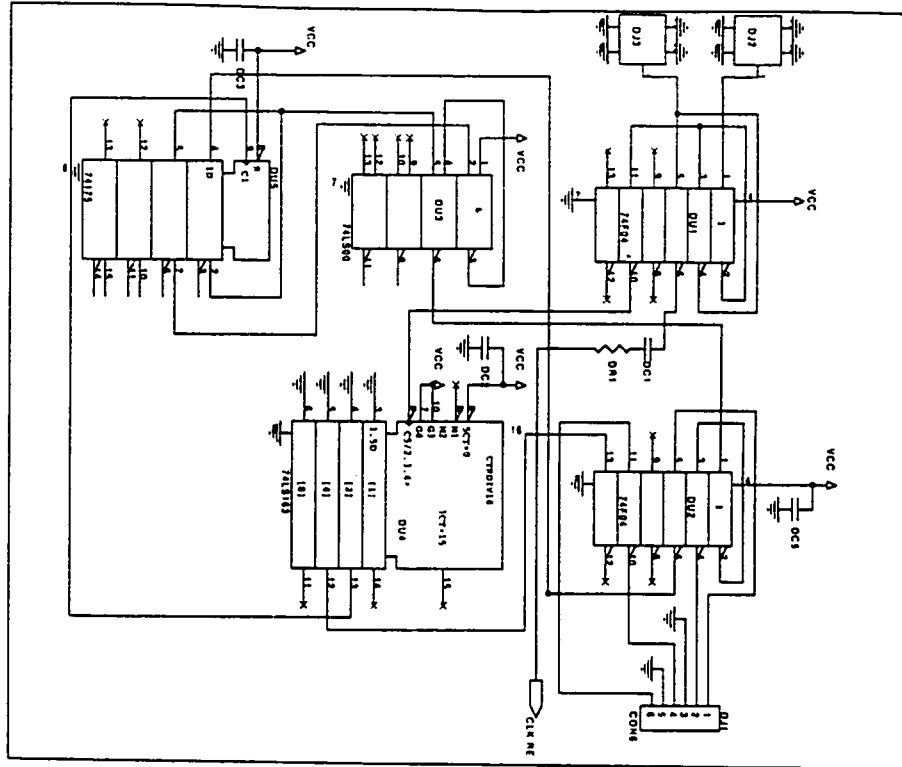
Figure 3.10: Digital synchronization circuitry for the Orbcomm receiver

- Buffering the timing pulses, and the reference clock signal from the GPS receiver.

- Generating interrupt signals for the microprocessor so that phase timing can be synchronized - see Section 7.I.D.

- Generating clock signals to drive the hardware, all synchronized to the GPS receiver clock.

A problem arises when the digital signals couple to other signals driving the receiver, namely the lines driving the microprocessor interrupts, and the lines carrying low-power rf signals. In the former case, noise on the line generates spurious interrupts; in the latter case, rf interference couples with the digital signals and enters some of the

27
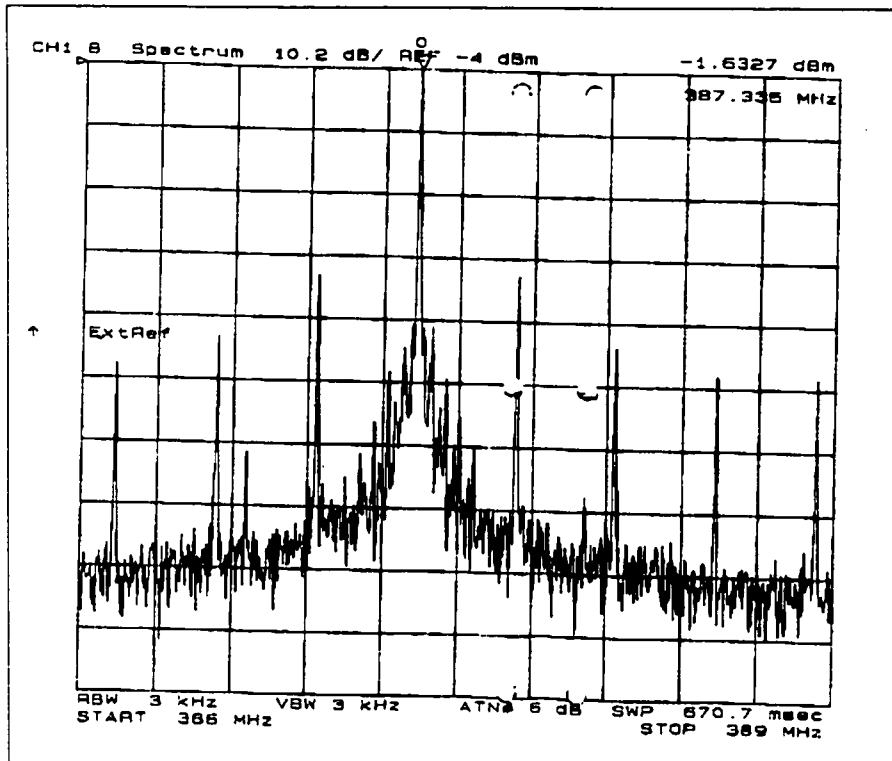
Figure 3.11: Output of the frequency synthesis circuitry, generating a UHF mixing signal

filtered bands shown in Figure 3.9. The primary solutions which were implemented are:

- Digital lines that source significant current must be coupled to ground with large capacitors.

- The interrupt signals are filtered using an RC network to eliminate high-frequency disturbances.

- Sensitive rf lines are laid out far from (and preferably perpendicular to) high current signals.

- rf lines are all enclosed within a *Faraday cage* formed using copper pour on
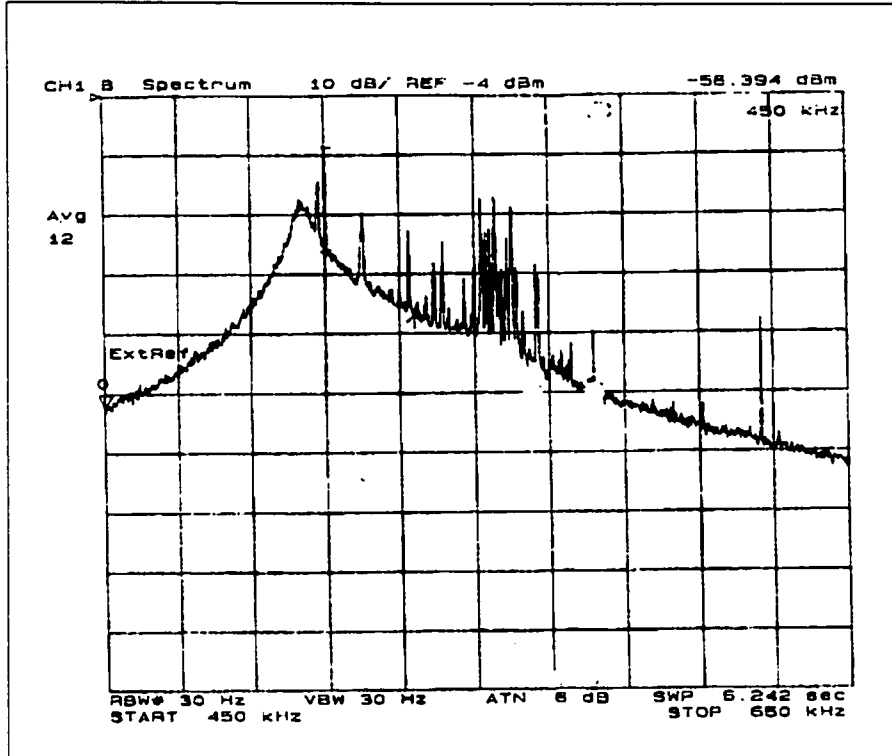
Figure 3.12: Spectral plot of interference on the signal emerging from the front end, with low-frequency filters tuned to 500kHz

the top and bottom layers of the 4-layer board. This also minimizes the effect of ambient disturbance radiation on the receiver.

- Analog ground and digital ground are separate, and are joined only at one point with a 10Ω resistor.

3.II.D   Design of Receiver Hardware - Mark III: Globalstar

The front end built for a Globalstar receiver, which is capable of achieving centimeter-level performance, is shown next to a cell-phone in Figure 3.15. Since our data reduction technique (Section 4.II) determines the frequency-dependent phase lags of the receiver front end in real time, there is no need for precisely calibrated rf

29
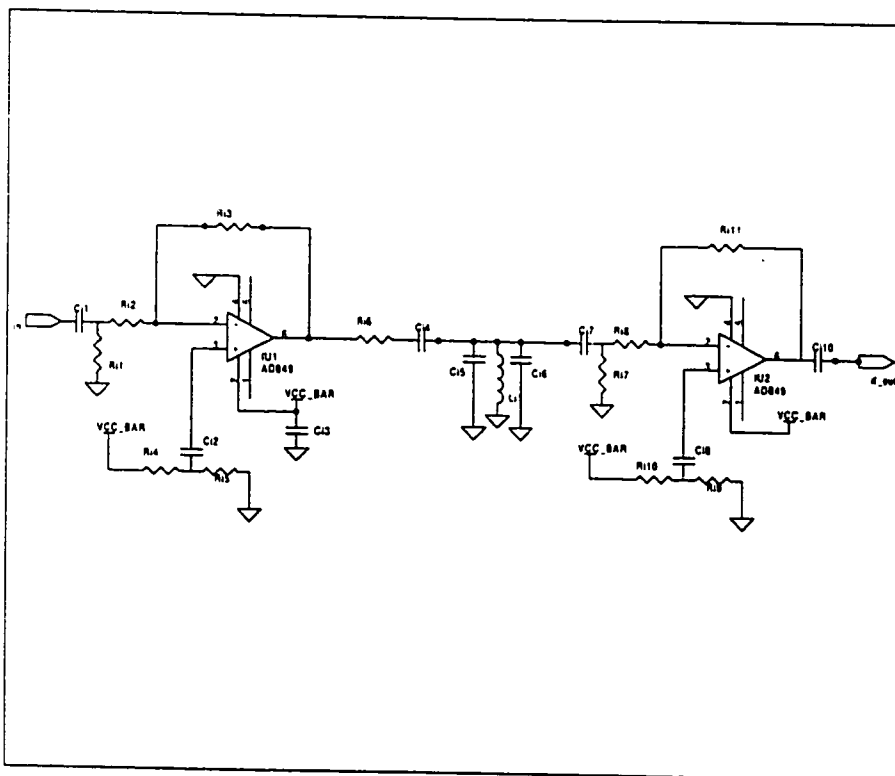
Figure 3.13: Intermediate frequency amplification and filtering
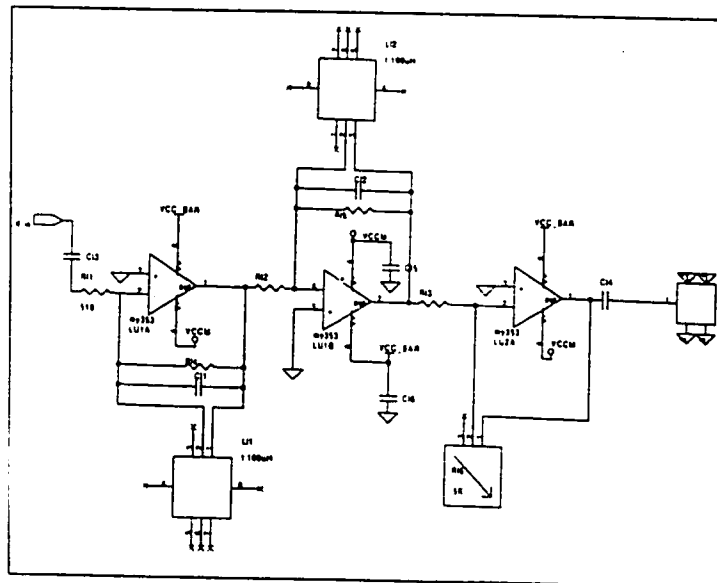
Figure 3.14: Tunable low frequency amplification and filtering

30

circuitry[3]. This front end uses only VLSI's designed for cell-phones which collectively cost under $10. Details motivating this design cannot be disclosed due to proprietary information relationships with Globalstar. However, in Appendix C, we estimate the phase-tracking performance of a Globalstar navigation receiver.

Figure 3.15: Front end for a Globalstar navigation receiver

3.II.E   Digital Signal Processing

The digital signal processing shown in Figure 3.16 was implemented using an AS-TRA SCM2001 Programmable Spread Spectrum Transceiver ASIC, administered by firmware operating on a Texas Instruments TMS320 16 bit microprocessor. We selected the ASTRA chip primarily for its ability to track Pseodo-random Noise (PN)

---

[3]We do require, however, that the phase lags of the front end vary at a much slower rate than the typical satellite tracking interval

codes of the type transmitted by the Globalstar satellites. However, in this section, we focus on those settings relevant for tracking the Orbcomm satellites. The A/D converters are driven by a sampling NCO which outputs an oversampling frequency, f_o, controlled by firmware. After sampling, the digital signal is mixed with the sine/cosine outputs of a mixing NCO. Typically, this NCO is controlled by firmware to close a phase-locked loop. However, in the case of a software PLL (Section 7.II) this simply functions as a down-converter. The signal is filtered by an accumulator, and then down-sampled by a decimation factor, D. In order to prevent overflow of the correlators, the signal is down-shifted before being applied to the chip-matched filter, CMF. The CMF filters the signal to a one-sided bandwidth of roughly half the chipping rate[1]. The output of the CMF is then downsampled by 8 for inputting into the early, late and prompt correlators. In the case of a CDMA signal, the correlators implement a delay-locked loop. In the case of Orbcomm, the correlator codes are of length $L = 16$, and are set to all ones. Consequently, they implement a low-pass filter, with frequency response shown in Figure 3.17. The output of the correlators are sampled by the microprocessor at the symbol rate, R.

Assume that the frequency of the signal emerging from the A/D converter is f_{if}. In order to preserve the integrity of this signal, and due to the hardware construction, certain restrictions apply to the selection of R, D and L, in relation to f_{if}. From the operations in Figure 3.16, it can be seen that

$$f_0 = 8RDL \qquad (3.2)$$

In order to avoid aliasing of disturbance signals, either the upper sideband output

---

[1]A similar filtering technique is applied to some spread spectrum signals to enhance noise characteristics and decrease signal bandwidth
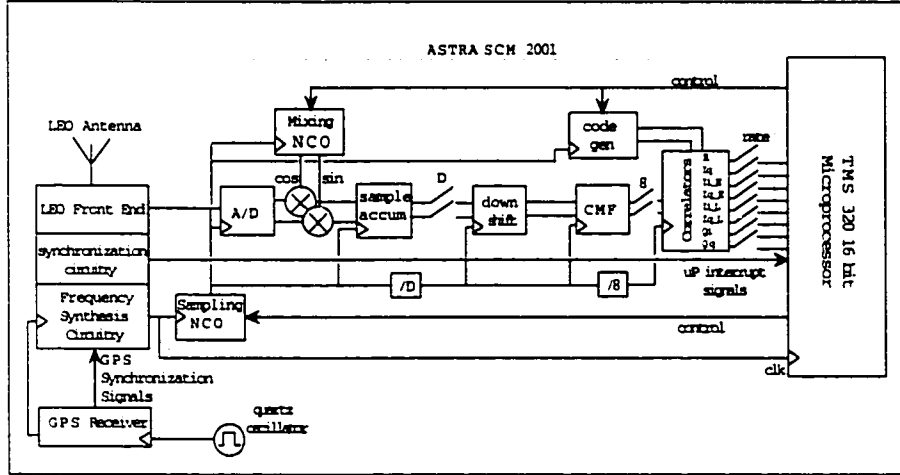
Figure 3.16: Digital signal processing implemented on the ASTRA SCM2001
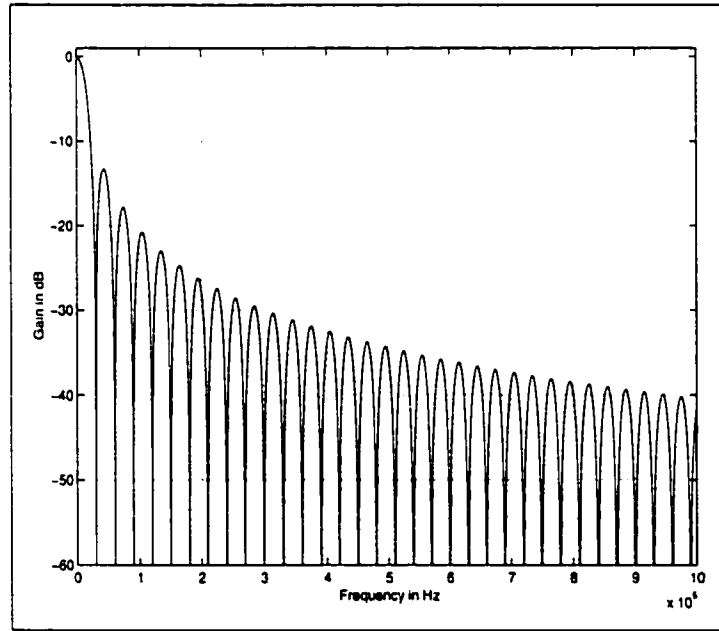
Figure 3.17: Filtering implemented by an all-zero code for the Orbcomm signal

from the mixer should be less than half the down-sampling rate, in which case

$$2f_{if} \ll \frac{1}{2}8RL \qquad (3.3)$$

33

or the upper sideband is filtered out by the D sample accumulator, in which case

$$2f_{if} \gg 8RL \qquad (3.4)$$

.

Lastly. due to the operation of the sampling NCO, the sampling rate cannot exceed the clocking frequency

$$f_o < f_{clk} \qquad (3.5)$$

Subject to these limitations, the parameters R, D and L can be freely determined in firmware. Similarly, the phase-locked loop control law can be adjusted in firmware based on the satellite being tracked. Since we use Doppler-aiding, a second order PLL with a closed loop bandwidth of 10Hz is sufficient to track the incident phase with sub-centimeter accuracy (Appendix C). The root locus design plot, and the closed loop bode plot for the second-order PLL are shown in Figure 3.18. A lead-lag network is used to improve transient response.

3.III   Receiver Software

In this section. we provide a high-level overview of the different modules which are necessary for a fully integrated precision navigation system. The algorithmic details of navigation software will be discussed in later Sections. These modules can be decomposed as illustrated in the block diagrams of Figure 3.19. Note that for the prototype system used in the experimental work of Section 9, these operations were
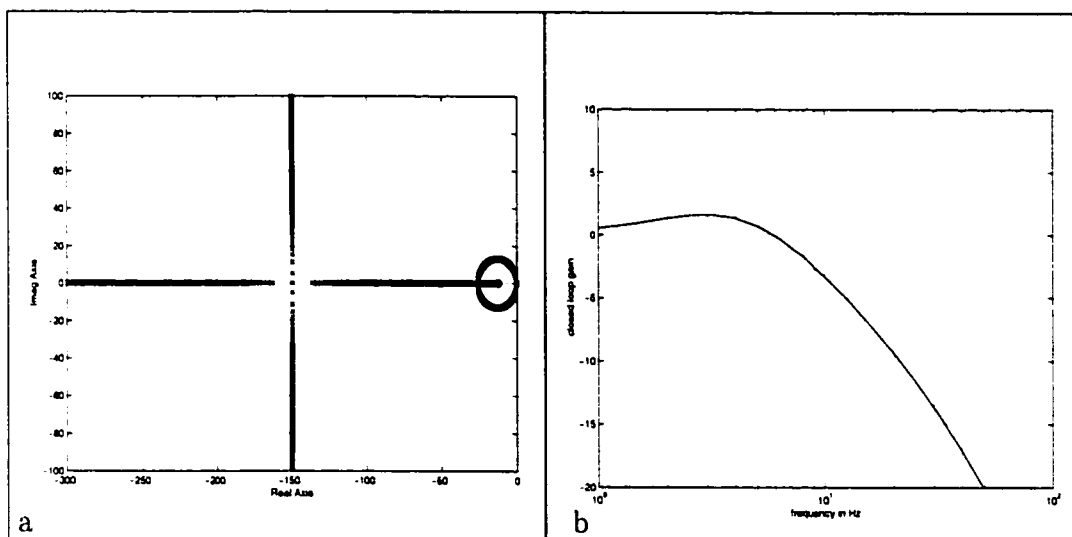
Figure 3.18: Root locus (a) and Bode plot (b) for the phase locked loop
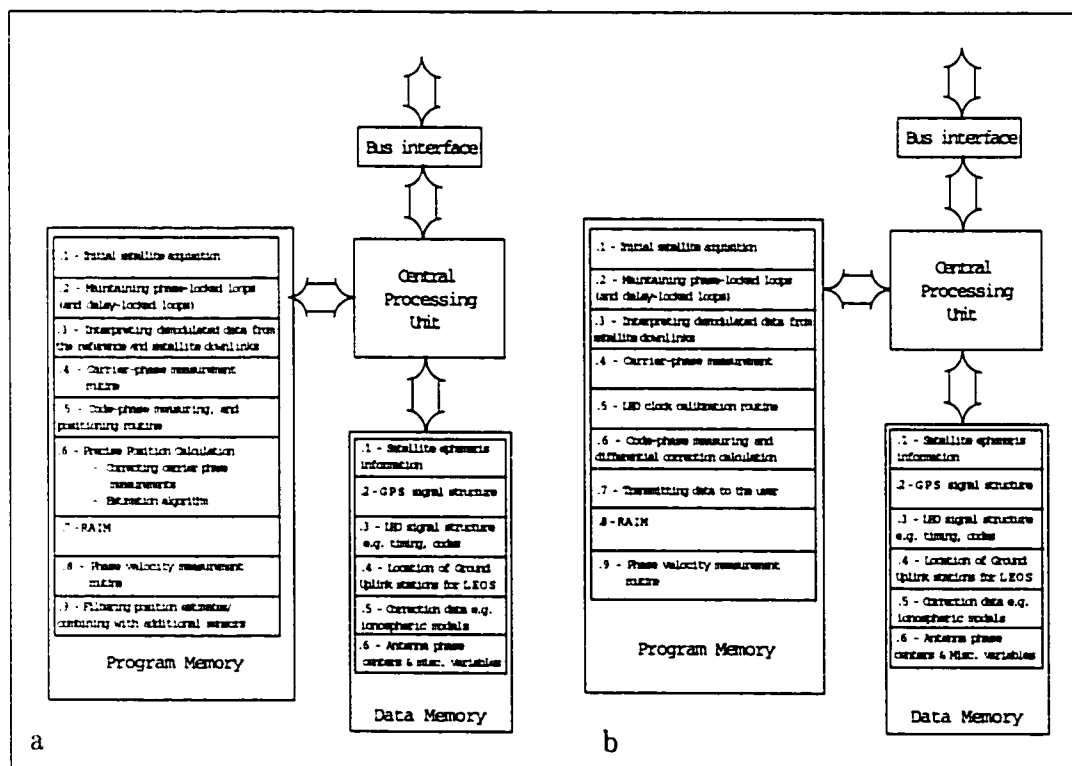
Figure 3.19: Overview of the receiver software modules. a) User receiver. b) Reference receiver.

35

distributed among a GPS receiver microprocessor (M68340), a LEO receiver micro-processor (TMS320), and a navigation processor (Intel Pentium II). In addition, not all the modules mentioned were necessary for the experimental work.

1 - The initial acquisition algorithm performs a search routine to establish phase-lock on satellite signals. This involves using the satellite ephemeris data, the GPS signal structure data, the LEO signal structure data, possibly the location of ground uplink stations, together with data from the tracking assemblies to control the tracking modules such that phase lock is established on the available satellite signals. A detailed description of initial acquisition of the Orbcomm satellites for a firmware tracking assembly is described in Section 7.II.

2 - The maintenance of phase-locked loops involves controlling the components of the tracking assemblies so that phase lock is maintained on all relevant signals. The microprocessor implements a control law for closing the phase-locked loops, and possibly, delay-locked loops for each of the tracking modules in use.

3 - Interpreting and demodulating data from the satellite downlinks involves using the data about the LEO and GPS signal structures to read and interpret the outputs of the tracking modules.

4 - The carrier phase measurement routine is the process whereby carrier phase data is read from the phase counters of each of the phase-counting assemblies and interpreted to produce phase measurements that can be input into the data-reduction routines.

5 - The code phase measuring and positioning routine is the process whereby code phase data is read from the GPS tracking assembly, corrected using the differential

corrections received from the reference and processed to obtain a meter-level position estimate and clock offset estimate.

6 - The position calculation routine involves the correction of carrier phase measurements as well as an estimation algorithm. The correction of carrier-phase measurements is the process whereby carrier-phase data is corrected for deterministic disturbances based on information received from the reference, satellite ephemeris information, possibly the location of ground uplink stations and possibly error prediction data. The nature of these corrections are discussed in Sections (4.I,6.I,6.II). The estimation algorithm is the key process by which data is processed to identify the integer cycle ambiguities for the GPS satellites as well as related parameters for the LEO satellites, and to subsequently position the user with centimeter-level precision relative to the reference receiver. The algorithm employs the satellite ephemeris information, the GPS signal structure data, the LEO signal structure data, and possibly the location of ground uplink stations.

7 - Receiver autonomous integrity monitoring may be used by the receiver to independently check the validity of the position solution using the satellite ephemeris information. This technique is described in more detail in Section 8.III.

8 - A phase velocity measurement routine may be employed to enhance the precision of position estimation while reducing the required bandwidth of the LRU. By estimating the phase velocity of the reference receiver, the user can predict the phase data from the reference station for several seconds. Consequently, data burst rates from the reference station may be as low as one every few seconds.

9 - Filtering position estimates involves applying to the position data a digital filter, which takes into account known aspects of the user's motion, such as bandwidth

37

constraints, in order to generate more accurate, noise-free, position estimates. This could also involve the use of Kalman-filtering techniques to combine the carrier-phase position estimates with data obtained from other sensors such as accelerometers and gyros.

We turn our attention now to the reference receiver of Figure 3.19b, to discuss those routines which are not necessarily applicable for the user receiver.

5 - The LEO clock calibration routine is used to identify frequency offsets of the LEO satellite oscillators. The algorithm makes use of the satellite ephemeris information, the GPS signal structure data, the LEO signal structure data and possibly the location of ground uplink transmitters to identify the frequency offset of the LEO downlink due to the long-term instability of the satellite oscillator. The technique is detailed in Section 6.III.

6 - The code phase measurements and differential correction calculation involve reading the code phase measurements from the GPS tracking assembly and combining this information with the known position data for the reference antenna, to calculate differential corrections for the user.

7 - Transmitting data to the user is the process of coding and transmitting the data destined for the user receiver in terms of the data communications protocol of the LRU.

Chapter 4

Precise Position Calculation

4.I Details of the Differential Carrier Phase Measurement

The scenarios in which centimeter-level positioning accuracy is required within roughly one minute of system initialization include surveying, construction, precise control of land vehicles, as well as high-integrity tasks such as attitude determination and automatic landing of aircraft. Similar data reduction techniques can be applied in all cases, with simplifications in the context of a user receiver that is stationary in *Earth-Based-Earth-Fixed* (EBEF) coordinates, or of a user receiver that is synchronized to the same clock as the reference receiver. We will focus our attention on the more general case of a mobile user receiver, which is driven by an oscillator that is distinct from that of the reference receiver. The purpose of this section is to determine the specifications on the hardware and firmware which synchronously measure the carrier phase of the incident satellite signals. The specifications are set such that all deterministic errors in the system are below the centimeter-level.

We denote the nominal carrier frequency of the satellite downlink as ω_s. The phase

of the satellite frequency synthesizer at time t_s can be described:

$$\Psi_s(t_s) = \omega_s t_s + \int^{t_s} \Delta\omega_s(\alpha)d\alpha \tag{4.1}$$

where $\Delta\omega_s(t_s)$ models the deviation from nominal frequency due to drift of the crystal oscillator on board the satellite. We model this drift as a time-varying offset in the satellite clock, $\tau_s(t_s) = \frac{1}{\omega_s}\int^{t_s} \Delta\omega(\alpha)d\alpha$. Consequently,

$$\Psi_s(t_s) = \omega_s[t_s + \tau_s(t_s)] \tag{4.2}$$

Similar clock offsets occur at the user and reference receivers. At true times t_u and t_r, the user and reference receivers respectively record times $t_u + \tau_u(t_u)$ and $t_r + \tau_r(t_r)$. Therefore, the phase output from the crystal oscillator of the user's receiver at time t_u is

$$\Psi_X(t_u) = \omega_X[t_u + \tau_u(t_u)] \tag{4.3}$$

where ω_X is the nominal oscillator frequency. The frequency synthesizer of the receiver generates the rf and if mixing signals by multiplying $\Psi_X(t_u)$ by factors α_{rf} and α_{if}, respectively. We denote the phase of the satellite signal emerging from the user receiver's LNA at time t_u as $\Psi_{su}(t_u)$. The output of the first mixer after bandpass filtering has phase $\Psi_1(t_u) = \Psi_{su}(t_u) - \alpha_{rf}w_X[t_u + \tau_u(t_u)]$. We assume for simplicity of explanation that the scheme of Figure 3.3a is employed. Hence, the second mixer, after filtering, generates a signal with phase $\Psi_2(t_u) = \Psi_{su}(t_u) - (\alpha_{rf} + \alpha_{if})w_X[t_u + \tau_u(t_u)]$. This phase is tracked by the phase-locked loop of the tracking module for satellite s,

and is read from the corresponding phase counter by the microprocessor. Since the nominal satellite frequency is ω_s, the nominal offset frequency of the signal tracked by the PLL is $\omega_o = \omega_s - (\alpha_{rf} + \alpha_{if})\omega_X$. The microprocessor differences the phase it reads, $\Psi_2(t_u)$, with the phase component caused by this offset frequency, ω_0. Since the microprocessor's measure of time interval is directly affected by crystal instability, it calculates this phase component as $\omega_0 [t_u + \tau_u(t_u)]$. The resulting phase measurement is

$$
\begin{aligned}
\phi_{su}(t_u) &= \omega_0 [t_u + \tau_u(t_u)] - \Psi_2(t_u) - N_{su}2\pi \\
&= \omega_s [t_u + \tau_u(t_u)) - \Psi_{su}(t_u) - N_{su}2\pi
\end{aligned}
\tag{4.4}
$$

where we have included an integer cycle phase ambiguity, N_{su}, since the microprocessor's initial phase measurement is modulus 2π. Consider now the phase of the incident satellite signal, Ψ_{su}. The signal is affected by phase disturbances on the satellite-to-user path, as well as frequency-dependent phase lags in the receiver. In addition, the phase measured depends on the position of the satellite, $\mathbf{r}_s$, at the time of transmission, rather than at the time of reception. Applying these factors to Equation (4.2), the phase of the signal from satellite s emerging from the LNA of the user receiver at time t_u is:

$$
\Psi_{su}(t_u) = \omega_s \left[t_u - \frac{1}{c}p_{su}\left(t_u - \frac{p_{su}(t_u - ...)}{c} \right) \right] + \omega_s \tau_s \left(t_u - \frac{p_{su}(t_u - \cdots)}{c} \right) - \mu_{su} - n_{su}
\tag{4.5}
$$

where μ_{su} is the frequency-dependent phase lag from the antenna phase-center to the A/D sampling circuitry of the receiver. n_{su} Represents the error due to ionospheric

41

and tropospheric delay as well as thermal noise and imperfect carrier-phase tracking in the receiver. n_{su} Is actually time-varying, but we ignore this time dependence for now. In order to represent the signal path length, we have denoted by $p_{su}(t_0)$ the distance from user's current position at time t_u to the satellite position at transmission time t_0, $p_{su}(t_0) = | \mathbf{r}_u(t_u) - \mathbf{r}_s(t_0) |$. Since we cannot know exactly the location from where a satellite transmitted if we do not know t_0, the precise calculation of t_0 requires an infinite regression. However, one can make the simplifying approximation

$$
t_u - \frac{1}{c} p_{su} \left(t_u - \frac{p_{su}(t_u - \cdots)}{c} \right) \approx t_u - \frac{1}{c} p_{su}(t_u) \tag{4.6}
$$

which generates a worst-case ranging error $< 2\ mm$ for satellites at 1400 km (the Globalstar nominal orbital altitude). Therefore, from Equation 's (4.4) and (4.5) we estimate the user's phase measurement at time t_u

$$
\mathcal{O}_{su}(t_u) = \frac{\omega_s}{c} p_{su} \left(t_u - \frac{p_{su}(t_u)}{c} \right) + \omega_s \left[\tau_u(t_u) - \tau_s \left(t_u - \frac{p_{su}(t_u)}{c} \right) \right] - N_{su} 2\pi + \mu_{su} + n_{su}
$$

$$
\tag{4.7}
$$

The receiver assigns a timetag, t, to the measurement made at time t_u. Since the user receiver does not know true time t_u, the timetag will be affected by the clock offset of the receiver. The measurement must therefore be recast in terms of the clock of the user's receiver. If a user receiver makes code-phase measurements on the GPS signals, the clock offset in the receiver, $\tau_u(t_u)$, can be estimated to within $1 \mu sec$. Once $\tau_u(t_u)$ has been estimated, two algorithmic approaches are possible. Firstly, one can use this estimate to select the times at which phase data is read from the phase counters in the receiver, so as to continually correct for the receiver's clock offset. This

42

clock steering technique limits the magnitude of the timetag error, $|t - t_u|$, to roughly $1\mu sec$. Secondly, one can use the estimate of $\tau_u(t_u)$ to actively correct for any errors which would arise in the differential phase measurement. Since these approaches are conceptually very similar, we will describe the latter approach in more detail.

Assume the user receiver estimates its clock offset to be $\hat{\tau}_u$ using code-phase measurements. We assume for now that $\hat{\tau}_u$ is time-independent since it need not be continually updated. We define $\Delta\tau_u(t_u) = \tau_u(t_u) - \hat{\tau}_u$. For phase data read at true time t_u, the user receiver assigns a timetag, $t = t_u + \Delta\tau_u(t_u) + T_u$, where T_u is a residual error in sampling time, distinct from the clock bias, resulting from the digital logic's imperfect precision in reading phase at the particular instant of time identified by the microprocessor. Recasting the measurement in terms of timetag t:

$$
\begin{aligned}
\phi_{su}(t_u) = {}& \frac{\omega_s}{c}p_{su}\left(t - \Delta\tau_u(t_u) - T_u - \frac{1}{c}p_{su}\left(t - \Delta\tau_u(t_u) - T_u\right)\right) \\
& + \omega_s\tau_u\left(t - \Delta\tau_u(t_u) - T_u\right) - N_{su}2\pi + \mu_{su} + n_{su} \\
& - \omega_s\tau_s\left(t - \Delta\tau_u(t_u) - T_u - \frac{1}{c}p_{su}\left(t - \Delta\tau_u(t_u) - T_u\right)\right)
\end{aligned}
\tag{4.8}
$$

Since $|\Delta\tau_u(t_u) + T_u|$ is of the order of a few μsec, we may Taylor-expand to first order in $\Delta\tau_u(t_u) + T_u$, with negligible error in dropping the higher-order terms,

$$
\phi_{su}(t_u) \approx
\tag{4.9}
$$

$$
\frac{\omega_s}{c}p_{su}\left(t - \frac{p_{su}(t)}{c}\right) + \omega_s\tau_u(t) - \frac{\omega_s}{c}\frac{\partial p_{su}(t)}{\partial t}[\Delta\tau_u(t) + T_u]
$$

$$
-\omega_s\tau_s(t - \frac{p_{su}(t)}{c}) - N_{su}2\pi + \mu_{su} + n_{su}
$$

Note that for highly unstable oscillators, one might include in this expansion the

43

terms $-\omega_s \frac{\partial \tau_u(t)}{\partial t}[\Delta \tau_u(t) + T_u]$ and $-\omega_s \frac{\partial \tau_s(t)}{\partial t}[\Delta \tau_u(t) + T_u]$, which could be incorporated into the estimation algorithm. However, these terms are negligible in most implementations of the system.

A similar approach to the reference receiver's phase measurement yields the expansion

$$\phi_{sr}(t_r) \approx \qquad\qquad\qquad\qquad\qquad\qquad\qquad\qquad (4.10)$$

$$\frac{\omega_s}{c} p_{sr}\left(t - \frac{p_{sr}(t)}{c}\right) + \omega_s \tau_r(t) - \frac{\omega_s}{c} \frac{\partial p_{sr}(t)}{\partial t}[\Delta \tau_r(t) + T_r]$$

$$-\omega_s \tau_s(t - \frac{p_{sr}(t)}{c}) - N_{sr} 2\pi + \mu_{sr} + n_{sr}$$

The reference receiver's phase measurement is timetagged with a time, t, and transmitted (or otherwise communicated) to the user. The user matches the timetags on the data and performs a single difference, which we now index with the timetag, t, rather than a true time. The differential measurement is then

$$\phi_s(t) = \phi_{su}(t_u) - \phi_{sr}(t_r) \qquad\qquad\qquad\qquad (4.11)$$

$$\approx \frac{\omega_s}{c} p_{su}\left(t - \frac{p_{su}(t)}{c}\right) - \frac{\omega_s}{c} p_{sr}\left(t - \frac{p_{sr}(t)}{c}\right)$$

$$+ \omega_s \left[\tau_s\left(t - \frac{p_{sr}}{c}\right) - \tau_s\left(t - \frac{p_{su}}{c}\right)\right] + \omega_s \left[\tau_u(t) - \tau_r(t)\right]$$

$$- \frac{\omega_s}{c} \frac{\partial p_{su}(t)}{\partial t}[\Delta \tau_u(t) + T_u] + \frac{\omega_s}{c} \frac{\partial p_{sr}(t)}{\partial t}[\Delta \tau_r(t) + T_r]$$

$$- (N_{su} - N_{sr}) 2\pi + (\mu_{su} - \mu_{sr}) + (n_{su} - n_{sr})$$

We may rewrite the terms involving $\frac{\partial p_{su}}{\partial t}$ and $\frac{\partial p_{sr}}{\partial t}$ as

$$\frac{\omega_s}{c} \frac{\partial p_{sr}(t)}{\partial t} \left[\tau_r(t) - \tau_u(t)\right] - \frac{\omega_s}{c} \frac{\partial p_{sr}(t)}{\partial t} \left[\hat{\tau}_r - \hat{\tau}_u\right]$$

$$+ \frac{\omega_s}{c} \frac{\partial p_{sr}(t)}{\partial t} \left[T_r - T_u\right] + \left(\frac{\partial p_{sr}(t)}{\partial t} - \frac{\partial p_{su}(t)}{\partial t}\right) \frac{\omega_s}{c} \left[\Delta\tau_u(t) + T_u\right] \qquad (4.12)$$

or equivalently as

$$\frac{\omega_s}{c} \frac{\partial p_{su}(t)}{\partial t} \left[\tau_r(t) - \tau_u(t)\right] - \frac{\omega_s}{c} \frac{\partial p_{su}(t)}{\partial t} \left[\hat{\tau}_r - \hat{\tau}_u\right]$$

$$+ \frac{\omega_s}{c} \frac{\partial p_{su}(t)}{\partial t} \left[T_r - T_u\right] + \left(\frac{\partial p_{sr}(t)}{\partial t} - \frac{\partial p_{su}(t)}{\partial t}\right) \frac{\omega_s}{c} \left[\Delta\tau_r(t) + T_r\right] \qquad (4.13)$$

We will adopt the representation shown in Equation (4.12). It will be obvious from the discussion how the issues we describe can be applied to the representation of Equation (4.13). The first term in Equation (4.12) can lead to large errors and is incorporated into the estimation strategy. The second term in Equation (4.12) can be directly calculated, and subtracted from the differential measurement. If the user and reference receivers are implemented with similar digital logic, the term $|T_r - T_u|$ can be made less than $.1\mu sec$. Hence the third term can be ignored with distance-equivalent errors $< 1mm$. Now consider the fourth term. For a satellite at $1400km$, and a stationary user receiver $10km$ from the reference, the term $\left(\frac{\partial p_{sr}(t)}{\partial t} - \frac{\partial p_{su}(t)}{\partial t}\right) <$ $50m/s$. To ensure that the fourth term produces a worst-case distance-equivalent error $< 1mm$ we must have $|\Delta\tau_u(t_u) + T_u| < 18\mu sec$, so that the term can be safely ignored. If we consider the phase-reading scheme displayed in Figure C.1, the time interval required to read all of the active phase-counters of all of the active phase counter assemblies contributes to the magnitude of the differentially uncompensated term $|\Delta\tau_u(t_u) + T_u|$. Hence, for a static user, this time interval should be roughly

$< 18\mu sec.$ However, for a mobile user receiver moving at, say, $250m/s$, the term $\left(\frac{\partial p_{sr}(t)}{\partial t} - \frac{\partial p_{su}(t)}{\partial t} \right) < 300m/s$, and the time period should be roughly $< 3\mu sec.$

The rate at which the estimate, $\hat{\tau}_u$, needs to be updated so that $\Delta \tau_u(t)$ remains small depends on the stability of the receiver oscillator. For example, for a long-term oscillator stability of $1 : 10^7$, updates every 2 minutes and every 20 seconds are sufficient for the static user and mobile user, respectively.

The terms in Equation (4.11) relating to the satellite clock offset can be expanded to first order

$$\omega_s \left[\tau_s \left(t - \frac{p_{sr}(t)}{c} \right) - \tau_s \left(t - \frac{p_{su}(t)}{c} \right) \right] \approx \frac{\partial \tau_s(t)}{\partial t} \frac{\omega}{c} (p_{sr}(t) - p_{su}(t)) \qquad (4.14)$$

For a satellite oscillator with long-term frequency stability of $1 : 10^6$ we expect $\frac{\partial \tau_s(t)}{\partial t}$ to get as large as 10^{-6}. This could cause distance-equivalent errors as large as $1cm$. In Section 6.III, we describe a technique for calibrating the frequency offset of the LEO satellite oscillator so that the first-order expansion of Equation (4.14) can be calculated and subtracted out of the phase measurement.

Eliminating all terms from measurement Equation (4.11) which are either negligible, or actively subtracted out of the measurement, the estimate of the resulting measurement is

$$\bar{o}_s(t) \approx \frac{\omega_s}{c} p_{su} \left(t - \frac{p_{su}(t)}{c} \right) - \frac{\omega_s}{c} p_{sr} \left(t - \frac{p_{sr}(t)}{c} \right) + \omega_s \left(1 - \frac{1}{c} \frac{\partial p_{su}(t)}{\partial t} \right) [\tau_u(t) - \tau_r(t)]$$
$$- (N_{su} - N_{sr}) 2\pi + (\mu_{su} - \mu_{sr}) + (n_{su} - n_{sr}) \qquad (4.15)$$

To clarify the estimation strategy, we redefine the components of this measurement

as follows:

$$\tau(t) = \tau_u(t) - \tau_r(t) \tag{4.16}$$

$$N_s = N_{su} - N_{sr} \tag{4.17}$$

$$\mu_s = \mu_{su} - \mu_{sr} \tag{4.18}$$

$$n_s = \frac{\lambda_s}{2\pi}(n_{su} - n_{sr}) \tag{4.19}$$

where λ_s is the nominal wavelength of the satellite carrier. Multiplying Equation (4.15) by $\frac{\lambda_s}{2\pi}$ to convert phase to a distance measurement, we then have

$$y_s(t) = p_{su}\left(t - \frac{p_{su}(t)}{c}\right) - p_{sr}\left(t - \frac{p_{sr}(t)}{c}\right) \tag{4.20}$$
$$+ \left(1 - \frac{1}{c}\frac{\partial p_{su}(t)}{\partial t}\right)c\tau(t) - N_s\lambda_s + \frac{\lambda_s}{2\pi}\mu_s + n_s$$

4.II   Estimation Strategy

If one attempts to estimate all of the integer components, $\{N_s\}$, as well as user position, $\mathbf{r}_u(t)$, and clock biases, $\tau(t)$, the complete set of parameters would be almost *unobservable*. The resulting estimation matrix would be poorly conditioned and highly susceptible to measurement noise, n_s. Consequently, we select one of the Navstar satellites, say Satellite 1, to be a *reference* satellite for differencing. We make an initial approximation of the associated integer, $\hat{N}_1$, using Equation (4.15), based on our estimate of position and clock offset using code-phase measurements. Then, we adjust the measurement

$$\bar{y}_s(t) = y_s(t) + \hat{N}_1 \tag{4.21}$$

47

and we redefine the parameters we seek to estimate as follows:

$$\bar{N}_s = \left(N_s - \frac{\mu_s}{2\pi}\right) - \frac{\lambda_1}{\lambda_s}(N_1 - \frac{\mu_1}{2\pi})$$

$$\bar{\tau}(t) = \tau(t) - \frac{\lambda_1}{c}\left(N_1 - \hat{N}_1 - \frac{\mu_1}{2\pi}\right) \tag{4.22}$$

If $\mid N_1 - \hat{N}_1 - \frac{\mu_1}{2\pi} \mid < 200$ *cycles*, the redefinition (4.22) leads to a maximum distance-equivalent error of $< 1mm$ for satellites at $1400km$. For the Navstar satellites, the new parameter, $\bar{N}_s$, simply reduces to $N_s - N_1$ since all GPS satellites are transmitting similar frequencies. For the LEO satellites, however, the phase-delays do not cancel and the parameters, $\bar{N}_s$, cannot be regarded as having integer values. However, the *difference* between the parameters, $\bar{N}_s$, for LEOS of the same constellation will be integer valued. For estimation techniques which exploit the integer nature of cycle ambiguities parameters, we preserve this information by selecting one of the LEO constant parameters, say $\bar{N}_S$, as a real-valued parameter which accommodates the unknown phase-lag terms. The $\bar{N}_s$ parameters for the other LEOS of the same constellation are then decomposed into a real-valued and integer-valued part. For example, assuming satellite $S - 1$ is in the same LEO constellation as S, $\bar{N}_{S-1} \rightarrow \bar{N}_S + \bar{N}_{S-1}$ where $\bar{N}_{S-1} \in \mathbf{Z}, \bar{N}_S \in \mathfrak{R}$. For clarity, we will not assume this redefinition occurs for the coming explanation, where we'll assume either that only one LEO is being tracked or that the parameters are all treated as real numbers. Special mention will be made of some crucial algorithmic issues which come to bear when this is not the case.

The measurement can now be approximated:

$$\bar{y}_s(t) = p_{su}\left(t - \frac{p_{su}(t)}{c}\right) - p_{sr}\left(t - \frac{p_{sr}(t)}{c}\right)$$

$$+ \; \left(1 - \frac{1}{c}\frac{\partial p_{su}(t)}{\partial t}\right) c\bar{\tau}(t) - \bar{N}_s\lambda_s + n_s \qquad (4.23)$$

where $\bar{N}_1$ is by definition 0.

The set of time-dependent parameters which we seek to estimate is

$$\boldsymbol{\Theta}(t) = \left[\mathbf{r}_u(t)^T \; c\bar{\tau}(t)\right]^T \qquad (4.24)$$

.

We create an *observation matrix* for these parameters based on our estimates of the line-of-sight vectors to the satellites

$$\mathbf{h}_s(t) = \left[\frac{\hat{\mathbf{p}}_{su}\left(t - \frac{\hat{p}_{su}(t)}{c}\right)^T}{\hat{p}_{su}\left(t - \frac{\hat{p}_{su}(t)}{c}\right)} \quad 1 - \frac{1}{c}\frac{\partial \hat{p}_{su}(t)}{\partial t}\right] \qquad (4.25)$$

For a current set of estimates, $\hat{\boldsymbol{\Theta}}(t)$ and $\hat{\bar{N}}_s$, we can construct an estimate of our prediction error for satellite s:

$$\begin{aligned}
\Delta y_s(t) \;=\; & \hat{p}_{su}\left(t - \frac{\hat{p}_{su}(t)}{c}\right) - p_{sr}\left(t - \frac{p_{sr}(t)}{c}\right) \\
& + \left(1 - \frac{1}{c}\frac{\partial \hat{p}_{su}(t)}{\partial t}\right) c\hat{\bar{\tau}}(t) - \hat{\bar{N}}_s\lambda_s - \bar{y}_s(t)
\end{aligned} \qquad (4.26)$$

Estimation matrices and prediction errors for all visible satellites are stacked into combined matrices,

49

$$H(t) = \begin{bmatrix} h_1(t) \\ h_2(t) \\ \vdots \\ h_S(t) \end{bmatrix} \quad \Delta Y(t) = \begin{bmatrix} \Delta y_1(t) \\ \Delta y_2(t) \\ \vdots \\ \Delta y_S(t) \end{bmatrix} \tag{4.27}$$

where S is the total number of satellites visible. The batch measurement equation, involving measurements from t_1 through t_N and the batch parameter update, $\Delta\hat{\Theta}$, can then be expressed as

$$\Delta Y = H\Delta\hat{\Theta} + V \tag{4.28}$$

with the matrix structures

$$\Delta Y = \begin{bmatrix} \Delta Y(t_1) \\ \Delta Y(t_2) \\ \vdots \\ \Delta Y(t_N) \end{bmatrix} \quad \Delta\hat{\Theta} = \begin{bmatrix} \Delta\dot{\Theta}(t_1) \\ \Delta\dot{\Theta}(t_2) \\ \vdots \\ \Delta\hat{\Theta}(t_N) \\ \Delta\hat{N}_2 \\ \vdots \\ \Delta\hat{N}_S \end{bmatrix}$$

$$H = \begin{bmatrix} H(t_1) & 0 & \cdots & & -\bar{\Lambda} \\ 0 & H(t_2) & 0 & \cdots & -\bar{\Lambda} \\ \vdots & & \ddots & & \vdots \\ 0 & \cdots & & H(t_N) & -\bar{\Lambda} \end{bmatrix} \tag{4.29}$$

where

$$\bar{\Lambda} = \begin{bmatrix} 0 & \cdots & \cdots & 0 \\ \lambda_2 & 0 & \cdots & 0 \\ 0 & \lambda_3 & \cdots & 0 \\ 0 & & \ddots & 0 \\ 0 & \cdots & \cdots & \lambda_S \end{bmatrix} \tag{4.30}$$

50

Note, in the case where LEO integer parameters, say for satellite $S - 1$, have been decomposed into an integer and real part, as discussed above, $\bar{\Lambda}$ becomes:

$$
\bar{\Lambda} = \begin{bmatrix}
0 & \cdots & \cdots & \cdots & 0 \\
\lambda_2 & 0 & \cdots & \cdots & 0 \\
0 & \lambda_3 & \cdots & \cdots & 0 \\
0 & & \ddots & \cdots & 0 \\
0 & \cdots & \cdots & \lambda_{S-1} & \lambda_S \\
0 & \cdots & \cdots & 0 & \lambda_S
\end{bmatrix}
\tag{4.31}
$$

The disturbance matrix $\mathbf{V}$ contains errors due to each satellite's measurement noise $n_s(t)$ - which we may reasonably assume is uncorrelated with distribution $n_s(t) \sim \mathcal{N}(0, \sigma_{n_s}^2)$ - as well as ephemeris errors $e_s(t)$ due to imperfect knowledge of the satellite's position which affects calculation of $\hat{p}_{su}$ and p_{sr}. Combining these two noise sources, the disturbance matrix has the form:

$$
\mathbf{V} = \begin{bmatrix}
n_1(t_1) + e_1(t_1) \\
\vdots \\
n_S(t_1) + e_S(t_2) \\
n_1(t_2) + e_1(t_2) \\
\vdots \\
n_S(t_2) + e_S(t_2) \\
\vdots
\end{bmatrix}
\tag{4.32}
$$

It should be noted that the matrix structures and parameters described above can be altered if the user receiver is static relative to the reference receiver. This situation pertains, for example, in surveying applications, or any problem where a vehicle can remain stationary until good integer estimates are available. In such scenarios we need only estimate the 3 coordinates of $\mathbf{r}_u(t_1)$. Given an estimate of the initial position, $\hat{\mathbf{r}}_u(t_1)$, our estimate of the position at time t_n is simply $\mathbf{G}(t_n - t_1)\hat{\mathbf{r}}_u(t_1)$, where $\mathbf{G}$ is a rotation about the z-axis in Earth-Centered Inertial (ECI) coordinates,

51

which accounts for the earth's rotation between time t_n and t_1[1]. To account for the reduction in the number of parameters, we define for each time t two separate stacked observation matrices:

$$\mathbf{H}_1(t) = \begin{bmatrix} \hat{p}_{1u}\left(t - \frac{\hat{p}_{1u}(t)}{c}\right)^T \\ \hline \hat{p}_{1u}\left(t - \frac{\hat{p}_{1u}(t)}{c}\right) \\ \vdots \\ \hat{p}_{Su}\left(t - \frac{\hat{p}_{Su}(t)}{c}\right)^T \\ \hline \hat{p}_{Su}\left(t - \frac{\hat{p}_{Su}(t)}{c}\right) \end{bmatrix} \quad \mathbf{H}_2(t) = \begin{bmatrix} 1 - \frac{1}{c}\frac{\partial \hat{p}_{1u}(t)}{\partial t} \\ \vdots \\ 1 - \frac{1}{c}\frac{\partial \hat{p}_{Su}(t)}{\partial t} \end{bmatrix} \qquad (4.33)$$

We then structure the batch estimation matrix, $\mathbf{H}$, as

$$\mathbf{H} = \begin{bmatrix} \mathbf{H}_1(t_1) & \mathbf{H}_2(t_1) & 0 & \cdots & & -\bar{\Lambda} \\ \mathbf{H}_1(t_2)\mathbf{G}(t_2 - t_1) & 0 & \mathbf{H}_2(t_1) & 0 & \cdots & -\bar{\Lambda} \\ \vdots & & 0 & \ddots & & \vdots \\ \mathbf{H}_1(t_N)\mathbf{G}(t_N - t_1) & 0 & \cdots & & \mathbf{H}_2(t_N) & -\bar{\Lambda} \end{bmatrix} \qquad (4.34)$$

and the batch parameter update matrix, $\Delta\hat{\Theta}$, as

$$\Delta\hat{\Theta} = [\Delta\hat{r}_x(t_1) \ \Delta\hat{r}_y(t_1) \ \Delta\hat{r}_z(t_1) \ c\Delta\hat{\tau}(t_1) \ \dots \ c\Delta\hat{\tau}(t_N) \ \Delta\hat{\tilde{N}}_2 \ \dots \ \Delta\hat{\tilde{N}}_S]^T \qquad (4.35)$$

and we may proceed with a batch measurement equation as in (4.28) above.

The parameter solution to Equation 4.28 becomes well conditioned as satellites are observed over a wide range of viewing angles. Sufficient conditioning can be achieved far more rapidly due to the geometric diversity resulting from the motion of the LEOS. This geometric diversity decreases the condition number of the estimation matrix $\mathbf{H}$

---

[1]If all positions in the system are calculated in Earth-Centered Earth Fixed Co-ordinates, $\mathbf{G}$ can simply be replaced by the identity matrix.

$$\kappa(\mathbf{H}) = \frac{\sigma_{max}(\mathbf{H})}{\sigma_{min}(\mathbf{H})} \tag{4.36}$$

where $\sigma_{min}(\mathbf{H})$ and $\sigma_{max}(\mathbf{H})$ are the minimum and maximum singular values of $\mathbf{H}$. The condition number indicates the sensitivity of the parameter solution to disturbances $\mathbf{V}$ as well as to errors in the estimation matrix, $\delta\mathbf{H}$. This concept can be made more concrete by considering the $\|\ \|_2$ norm of the parameter estimate errors for a simple least-squares parameter solution. Imagine $\Delta\hat{\Theta}_*$ is the parameter update solution of the least-squares problem with the error sources $\delta\mathbf{H}$ and $\mathbf{V}$ removed:

$$\Delta\hat{\Theta}_* = \arg \min_{\Delta\Theta \in \Re^{4N+S-1}} \|(\mathbf{H} - \delta\mathbf{H})\Delta\Theta - (\Delta\mathbf{Y} - \mathbf{V})\|_2 \tag{4.37}$$

while $\Delta\hat{\Theta}_{LS}$ is the actual least-squares solution found

$$\Delta\hat{\Theta}^{LS} = \arg \min_{\Delta\Theta \in \Re^{4N+S-1}} \|\mathbf{H}\Delta\Theta - \Delta\mathbf{Y}\|_2 \tag{4.38}$$

It can be shown [20] that if

$$\epsilon = \max\left\{\frac{\|\delta\mathbf{H}\|_2}{\|\mathbf{H}\|_2}, \frac{\|\mathbf{V}\|_2}{\|\Delta\mathbf{Y}\|_2}\right\} < \kappa(\mathbf{H}) \tag{4.39}$$

and

$$\sin\beta = \frac{\|\mathbf{H}\Delta\Theta_{LS} - \Delta\mathbf{Y}\|_2}{\|\Delta\mathbf{Y}\|_2} \tag{4.40}$$

then

$$\frac{\|\Delta\Theta_{LS} - \Delta\Theta_*\|_2}{\|\Delta\Theta_{LS}\|_2} \le \epsilon\kappa(\mathbf{H})\left(\frac{2}{\cos(\beta)} + \tan(\beta)\kappa(\mathbf{H})\right) \qquad (4.41)$$

Equation (4.41) indicates how small $\kappa(\mathbf{H})$ should be for a given ϵ in order to achieve a desired level of accuracy in the parameter estimates[2].

Many different mathematical methods can yield a solution to the problem posed in Equation (4.28). A method can be chosen depending on the processing power available in the receiver and the requirements of the specific application. Some different approaches are discussed below. We begin by describing two canonical approaches to the estimation problem which treat the integer parameters as real numbers. We then describe a combined smoothing and integer search methodology that efficiently resolves frequency-dependent phase lags as well as a set of integer parameters. Although designed for the combined LEO-GPS architecture, the performance of the latter algorithm suggests that it has application to a very wide range of cycle ambiguity resolution problems.

4.III   Maximum Likelihood Update

We assume now that our estimated parameter set $\hat{\Theta}$ is near enough the true parameter solution that there are negligible errors due to higher order terms incurred in linearizing the measurement equation to derive (4.28). Based thereupon, we seek the maximum likelihood update:

---

[2]This analysis does not require that $\mathbf{V}$ be serially uncorrelated, and is relevant to ephemeris and multipath disturbance.

$$\Delta \hat{\Theta}_{ML} = \arg \max_{\Delta \Theta \in \Re^{4N+S-1}} \text{Prob}\left\{\Delta \mathbf{Y} \mid \Delta \hat{\Theta}\right\} \tag{4.42}$$

This ML update requires knowledge of the measurement covariance matrix. Since the ephemeris errors are strongly correlated, the covariance matrix, $\mathbf{C} = E\left\{\mathbf{V}\mathbf{V}^T\right\}$, has non-diagonal structure. Over the course of five minutes of tracking, one can roughly model the satellite position generated from the ephemeris data as

$$\hat{\mathbf{r}}_s(t) = \mathbf{r}_s(t) + \Delta \mathbf{r}_s \tag{4.43}$$

where $\Delta \mathbf{r}_s$ is a constant offset, modeling the difference between a satellite's true position and the position estimate based on the ephemeris data. We describe this offset vector in terms of normally distributed components:

$$\Delta \mathbf{r}_s = [\Delta x_s \quad \Delta y_s \quad \Delta z_s]^T, \quad \Delta x_s, \Delta y_s, \Delta z_s \sim N\left(0, \sigma_e^2\right) \tag{4.44}$$

This error in the ephemeris data would result in an ephemeris disturbance (see Equation (4.32)):

$$e_s(t) = (p_{su}(t) - p_{sr}(t)) - (\hat{p}_{su}(t) - \hat{p}_{sr}(t)) \tag{4.45}$$

$$\approx -\frac{\Delta \mathbf{r}_s(t)^T \mathbf{r}_{ru}(t)}{r_{su}(t)} \tag{4.46}$$

where $\mathbf{r}_{ru} = \mathbf{r}_{sr} - \mathbf{r}_{su}$ and the approximation is achieved with a first-order expansion, assuming that $\|\Delta \mathbf{r}_s\|_2, \|\Delta \mathbf{r}_{ru}\|_2 \ll r_{su}, r_{sr}$. Using this first-order approximation, we find the second moment of the ephemeris disturbance statistics:

55

$$E\left\{e_s(t_1)e_s(t_2)\right\} \approx \sigma_e^2 \left[\frac{\mathbf{r}_{ur}(t_1)^T \mathbf{r}_{ur}(t_2)}{r_{su}(t_1)r_{su}(t_2)}\right] = \sigma_{es}^2(t_1, t_2) \qquad (4.47)$$

Consequently, the batch covariance matrix $\mathbf{C}$ will have structure:

$$\mathbf{C} = \begin{bmatrix} \mathbf{C}_n + \mathbf{C}_e(t_1) & \mathbf{C}_e(t_1, t_2) & \mathbf{C}_e(t_1, t_3) & \dots \\ \mathbf{C}_e(t_2, t_1) & \mathbf{C}_n + \mathbf{C}_e(t_2) & \mathbf{C}_e(t_2, t_3) & \dots \\ \mathbf{C}_e(t_3, t_1) & \mathbf{C}_e(t_3, t_2) & \mathbf{C}_n + \mathbf{C}_e(t_3) & \ddots \\ \vdots & \vdots & \ddots & \ddots \end{bmatrix} \qquad (4.48)$$

where

$$\mathbf{C}_e(t_i, t_j) = \begin{bmatrix} \sigma_{e1}^2(t_i, t_j) & & 0 \\ & \ddots & \\ 0 & & \sigma_{eS}^2(t_i, t_j) \end{bmatrix} \qquad (4.49)$$

$$\mathbf{C}_n = \begin{bmatrix} \sigma_{n1}^2 & & 0 \\ & \ddots & \\ 0 & & \sigma_{nS}^2 \end{bmatrix} \qquad (4.50)$$

Given matrix $\mathbf{C}$, the ML parameter update is:

$$\Delta\hat{\Theta}_{ML} = \left(\mathbf{H}^T \mathbf{C}^{-1} \mathbf{H}\right)^{-1} \mathbf{H}^T \mathbf{C}^{-1} \Delta\mathbf{Y} \qquad (4.51)$$

In essence, this iterative estimation strategy is the Gauss-Newton technique, where we have pre-multiplied the batch estimation equation (4.28) by the whitening matrix $\mathbf{C}^{-\frac{1}{2}}$ to achieve the ML update. Since the measurements in Equation (4.23) are only mildly nonlinear in $\mathbf{r}_u$, three iterations are typically sufficient to converge to the experimental noise floor. This technique for solving the ML estimation problem requires $O(N^3)$ flops. Many techniques exist for reducing the computation time re-

56

quired by exploiting the sparse structure of the measurement matrix $\mathbf{H}$. One such technique is outlined in Appendix D.

Chapter 5

Solving the Maximum Likelihood Problem with Integer Parameters

5.I Formulating the Problem

All of the techniques discussed so far treat the integer parameters as real numbers in the estimation strategy. In this section, we discuss a technique for solving the maximum likelihood problem assuming an integer parameter set. For this technique, we again assume that the off-diagonal terms of the batch covariance matrix in Equation (4.48), due primarily to ephemeris errors, are negligible. Assume for the time being that our current parameter estimates are close to the ML solution, so that no iteration is necessary and we drop the Δ notation. Consider the batch measurement of Equation (4.28) rewritten as

$$\mathbf{Y} = \mathbf{H}_\theta \theta + \mathbf{H}_z \mathbf{z} + \mathbf{v} \tag{5.1}$$

where $\mathbf{H}_\theta$ and $\mathbf{H}_z$ are the estimation matrices for the real and integer parameters respectively, θ is the matrix of real parameters, $\mathbf{z}$ is the $q \times 1$ matrix of integer

parameters, and $\mathbf{v}$ is the disturbance matrix which has a normal distribution $\mathbf{v} \sim \mathcal{N}(0, \mathbf{C})$. Recall, as discussed in Section 4.II, that for every additional constellation of LEOS tracked, one of the bias parameters will go towards calibrating the frequency-dependent phase-lags of the receiver, and will not have an integer nature. In addition, one of the GPS bias parameters is assumed to be known. Consequently, if one LEO constellation is used to augment GPS, and the total number of satellites tracked is S, we will have $q = S - 2$ integer parameters to estimate. Notice that θ contains the time-varying position and clock estimates, as well as the real-valued bias parameters.

Now, if we treat $\mathbf{z}$ as a vector of real parameters, and find the maximum-likelihood batch solution, the expected values of the solution will be

$$E \begin{bmatrix} \hat{\theta} \\ \hat{\mathbf{z}} \end{bmatrix} = \begin{bmatrix} \theta \\ \mathbf{z} \end{bmatrix} \qquad (5.2)$$

and the covariance on the solution will be

$$Cov \begin{bmatrix} \hat{\theta} \\ \hat{\mathbf{z}} \end{bmatrix} = \begin{bmatrix} \mathbf{H}_\theta^T \\ \mathbf{H}_z^T \end{bmatrix} \mathbf{C}^{-1} \begin{bmatrix} \mathbf{H}_\theta & \mathbf{H}_z \end{bmatrix} \qquad (5.3)$$

Applying the block-matrix inverse formula, the estimate of the integer parameters is found to be normally distributed according to: $\hat{\mathbf{z}} \sim N(\mathbf{z}, \mathbf{P}_z)$ where

$$\mathbf{P}_z = \left[\mathbf{H}_z^T \mathbf{C}^{-1} \mathbf{H}_z - \mathbf{H}_z^T \mathbf{C}^{-1} \mathbf{H}_\theta \left(\mathbf{H}_\theta^T \mathbf{C}^{-1} \mathbf{H}_\theta \right)^{-1} \mathbf{H}_\theta^T \mathbf{C}^{-1} \mathbf{H}_z \right]^{-1} \qquad (5.4)$$

We can consider the least-squares solution $\hat{\mathbf{z}}$ to be generated by $\hat{\mathbf{z}} = \mathbf{z} + \mathbf{u}$ where $\mathbf{u}$ is the disturbance term. Define the whitening matrix $\mathbf{G} = \mathbf{P}_z^{-\frac{1}{2}}$. The maximum likelihood estimation problem can now be framed as

60

$$z_{ML} = \arg \min_{\mathbf{z} \in \mathbf{Z}^{q \times 1}} \| \mathbf{Gz} - \mathbf{G\hat{z}} \|_2 \tag{5.5}$$

.

5.II   Information Smoothing

In practice, batch solutions to (5.1) are difficult to implement. Aside from computational issues, batch algorithms are difficult to administer when satellites are coming in or out of view, or cycle slips occur, while data is being stacked for processing. Information smoothing is preferable for its flexibility in dealing with such situations as well as its computational efficiency. In essence, the information smoother passes the linear Kalman filter forward and backward over the data before updating the parameter set.

We describe the set of parameter updates as

$$\Delta \mathbf{x}(t) = \begin{bmatrix} \Delta \theta(t) \\ \Delta \bar{\mathbf{n}} \end{bmatrix} \tag{5.6}$$

where $\Delta \bar{\mathbf{n}} = [\Delta \bar{N}_2 \ldots \Delta \bar{N}_S]^T$. The parameters of $\Delta \bar{\mathbf{n}}$ are treated as real numbers by the smoothing routine, however, as per the discussion of Section 5.III, all save one are integer valued. We assume, without loss of generality, that the real-valued parameter, which accommodates the difference in phase lag between the LEO and GPS channels, is $\Delta \bar{N}_S$. We model the evolution of parameters between phase measurements as a Markov process

61

$$\Delta \mathbf{x}(t_k) = \Delta \mathbf{x}(t_{k-1}) + \mathbf{w}(t_k) \qquad (5.7)$$

where

$$
\begin{aligned}
E\left\{\mathbf{w}(t_k)\mathbf{w}(t_k)^T\right\} &= \mathbf{Q}(t_k) \\
&= \lim_{\sigma_w \to \infty} \begin{bmatrix} \mathbf{I}_4\sigma_w{}^2 & \mathbf{0} \\ \mathbf{0} & \mathbf{0} \end{bmatrix}
\end{aligned} \qquad (5.8)
$$

This process is based upon the idea that the integers are constant for all phase measurements and that no assumption is made about the user's motion, nor about the clock drift of the receiver, between measurements. We model the phase prediction error of Equation (4.27) with a linear approximation:

$$\Delta \mathbf{y}(t_k) = \mathbf{H}(t_k)\Delta \mathbf{x}(t_k) + \mathbf{v}(t_k) \qquad (5.9)$$

where

$$
E\left\{\mathbf{v}(t_k)\mathbf{v}(t_k)^T\right\} = \mathbf{R}(t_k) = \begin{bmatrix} \sigma_{e1}(t_k)^2 + \sigma_{n1}^2 & \cdots & 0 \\ \vdots & \ddots & \\ 0 & & \sigma_{eS}(t_k)^2 + \sigma_{nS}^2 \end{bmatrix} \qquad (5.10)
$$

Denoting the covariance of our post-measurement estimate $\Delta \hat{\mathbf{x}}(t_k)$ as $\mathbf{P}(t_k)$, the Kalman filtering equations for this system are [27]:

$$\mathbf{P}(t_k)^{-1} = \left(\mathbf{P}(t_{k-1}) + \mathbf{Q}(t_{k-1})\right)^{-1} + \mathbf{H}(t_k)^T\mathbf{R}(t_k)^{-1}\mathbf{H}(t_k) \qquad (5.11)$$

$$\Delta \hat{\mathbf{x}}(t_k) = \Delta \hat{\mathbf{x}}(t_{k-1}) + \mathbf{P}(t_k)\mathbf{H}(t_k)^T\mathbf{R}(t_k)^{-1}\left(\Delta \mathbf{y}(t_k) - \mathbf{H}(t_k)\Delta \hat{\mathbf{x}}(t_{k-1})\right)$$

If phase-lock is attained on a new satellite s during parameter estimation, the initial covariance of the parameter estimate $\Delta \hat{N}_s$ is very large; this can cause computational difficulties. Consequently, we use instead an information form of the Kalman filter ([8], [47]) where we define an information matrix

$$S(t_k) = P(t_k)^{-1} = \begin{bmatrix} P_\theta(t_k) & P_{\theta n}(t_k) \\ P_{\theta n}(t_k)^T & P_n(t_k) \end{bmatrix}^{-1} = \begin{bmatrix} S_\theta(t_k) & S_{\theta n}(t_k) \\ S_{\theta n}(t_k)^T & S_n(t_k) \end{bmatrix} \quad (5.12)$$

and an information vector $v(t_k) = S(t_k)\Delta\hat{x}(t_k)$. These definitions, together with the disturbance model of Equation (5.9) allow us to considerably reduce the smoother computationally. By taking the limit of $\sigma_w \to \infty$, the update equations (5.11) simplify as follows:

$$
\begin{aligned}
S(t_k) &= \begin{bmatrix} 0 & 0 \\ 0 & P_n(t_k)^{-1} \end{bmatrix} + H(t_k)^T R(t_k) H(t_k) \\
&= \begin{bmatrix} 0 & 0 \\ 0 & S_n(t_{k-1}) - S_{\theta n}(t_{k-1})^T S_\theta(t_{k-1})^{-1} S_{\theta n}(t_{k-1}) \end{bmatrix} + H(t_k)^T R(t_k) H(t_k), \\
S(t_0) &= 0
\end{aligned}
\quad (5.13)
$$

$$
\begin{aligned}
v(t_k) &= S(t_k)\Delta\hat{x}(t_{k-1}) + H(t_k)R(t_k)^{-1}\left(\Delta y(t_k) - H(t_k)\Delta\hat{x}(t_{k-1})\right) \\
&= \begin{bmatrix} 0 & 0 \\ 0 & S_n(t_{k-1}) - S_{\theta n}(t_{k-1})^T S_\theta(t_{k-1})^{-1} S_{\theta n}(t_{k-1}) \end{bmatrix} \begin{bmatrix} \Delta\hat{\theta}(t_k) \\ \Delta\hat{n}(t_k) \end{bmatrix} \\
&\quad + H(t_k)^T R(t_k)^{-1}\Delta y(t_k) \\
&= \begin{bmatrix} 0 \\ v_n(t_{k-1}) - S_{\theta n}(t_{k-1})^T S_\theta(t_{k-1})^{-1} v_\theta(t_{k-1}) \end{bmatrix} + H(t_k)^T R(t_k)^{-1}\Delta y(t_k), \\
v(t_0) &= 0
\end{aligned}
\quad (5.14)
$$

In order to emulate the batch solution, the filter is passed forward and backward over the data. For the backward pass, we simply interchange the t_{k-1} and t_k in

63

Equation (5.13), and start with initial conditions $S(t_N) = 0$ and $v(t_N) = 0$. The $S(t_k)$ and $v(t_k)$ from forward and backward passes are linearly combined

$$S(t_k) = S(t_k)^F + S(t_k)^B \tag{5.15}$$

$$v(t_k) = v(t_k)^F + v(t_k)^B \tag{5.16}$$

and the parameter updates are then found according to $\Delta\hat{x}(t_k) = S(t_k)^{-1}v(t_k)$. The position and clock estimates, if desired, are updated according to

$$\begin{bmatrix} \hat{r}(t_k) \\ c\hat{\tau}_k \end{bmatrix} \rightarrow \begin{bmatrix} \hat{r}(t_k) \\ c\hat{\tau} \end{bmatrix} + \Delta\theta(t_k) \tag{5.17}$$

Assuming the noise assumptions are accurate, it makes no difference which $\Delta x(t_k)$ in the sequence $k = 1 \ldots N$ is used to update the constant parameters $\hat{n}$. This is born out in practice. It is simplest to take the parameter updates from the last measurement epoch t_N:

$$\hat{n} \leftarrow \hat{n} + \Delta\hat{n}(t_N) \tag{5.18}$$

The smoothing and updating process is repeated until the elements of $\Delta\hat{x}(t_k)$ become negligibly small. When this condition occurs, we check (as per Section 5.III) to see if we may estimate the integers with acceptable integrity. If this is the case, one final pass of the smoother is initiated to obtain the data necessary for the integer search routine. For those parameters that are integer-valued, we seek to preserve their integer nature in calculating the phase prediction error (Equation (4.26)) so that this information can be exploited in an integer-search operation. Consequently,

on the final smoothing pass, before calculating the phase prediction error of Equation (4.26), the relevant parameters are rounded off:

$$\hat{\bar{n}}_i \leftarrow \lceil \hat{\bar{n}}_i \rfloor, \quad i = 1 \ldots S - 2 \tag{5.19}$$

After the final smoother pass, we find the covariance of the constant parameters

$$\mathbf{P}_n(t_N) = \left(\mathbf{S}_n(t_N) - \mathbf{S}_{\theta n}(t_N)^T \mathbf{S}_\theta(t_N)^{-1} \mathbf{S}_{\theta n}(t_N) \right)^{-1} \tag{5.20}$$

The covariance matrix for the integer-valued parameters, first described in Equation (5.4) can be found from the relevant rows and columns of $\mathbf{P}_n$: $\mathbf{P}_z \leftarrow \mathbf{P}_n(t_N)_{1:S-2,1:S-2}$. Similarly, the preliminary estimates of the integer parameters, as discussed above, are obtained from the estimated bias updates of the final smoother pass

$$\hat{\mathbf{z}} = [\Delta \bar{n}_1(t_N) \ldots \Delta \bar{n}_{S-2}(t_N)] \tag{5.21}$$

We now define $\mathbf{G} = \mathbf{P}_z^{-\frac{1}{2}}$ and we are ready to search for the integer solution as per Equation (5.5).

5.III   Determining the Likelihood of Correct Cycle Ambiguity Resolution

Given our noise assumptions, we may now compare the relative likelihood of two integers vectors, say $\mathbf{z}_1$ and $\mathbf{z}_2$ according to

$$\frac{Prob(\mathbf{z} = \mathbf{z}_1)}{Prob(\mathbf{z} = \mathbf{z}_2)} = exp(\|\mathbf{G}(\mathbf{z}_2 - \mathbf{z})\|_2^2 - \|\mathbf{G}(\mathbf{z}_1 - \mathbf{z})\|_2^2) \qquad (5.22)$$

However, instead of searching through a large set of integer vectors to find the most likely combination, we would ideally like to establish a lower bound on the confidence with which any particular vector of integers can be selected. This confidence is independent of any particular estimate of the integers. When the confidence is sufficiently high, we would like to perform an efficient integer search, considering as few combinations as possible.

As a first step, define the random variable $\bar{\mathbf{z}} = \mathbf{G}\mathbf{z}$, $\bar{z} \sim N(\mathbf{G}\mathbf{z}, \mathbf{I}^{q \times q})$. The maximum-likelihood problem of Equation (5.5) now reads

$$\mathbf{z}_{ML} = \arg \min_{\mathbf{z} \in \mathbf{Z}^{q \times 1}} \|\bar{\mathbf{z}} - \mathbf{G}\mathbf{z}\|_2 \qquad (5.23)$$

The matrix $\mathbf{G}$ is termed the *lattice generator* [1]. It forms the basis of a lattice, $L(\mathbf{G}) = \{\mathbf{G}z \mid \mathbf{z} \in \mathbf{Z}^{q \times 1}\}$ which is conceptually illustrated in Figure 5.1 for $q = 2$. For the lattice $L(\mathbf{G})$, each integer point $\mathbf{z}_i$ is associated with a *Voronoi cell* which contains all the points $\bar{z}$ which are closer to $\mathbf{G}\mathbf{z}_i$ than any other $\mathbf{G}\mathbf{z}_j, j \neq i$. The Voronoi cell for $\mathbf{z}_i$ is $\{\bar{\mathbf{z}} \in \mathbf{R}^{q \times 1} \mid \|\bar{\mathbf{z}} - \mathbf{G}\mathbf{z}_i\| < \|\bar{\mathbf{z}} - \mathbf{G}\mathbf{z}_j\|, j \neq i\}$.

Such a Voronoi cell is illustrated in the Figure 5.1. The confidence with which a particular integer combination may be selected is found by integrating the probability density function (pdf) of $\bar{z}$ over the entire volume of a Voronoi cell. However, since the Voronoi cell is defined by multiple hyperplanes, this integral is difficult to compute. In order to make this computation tractable, we approximate a Voronoi cell with the largest ball which can fit therein. All that we require to approximate the the pdf

66

integral is the radius of this ball, which is illustrated in Figure 5.1 as $\frac{d_{min}}{2}$.
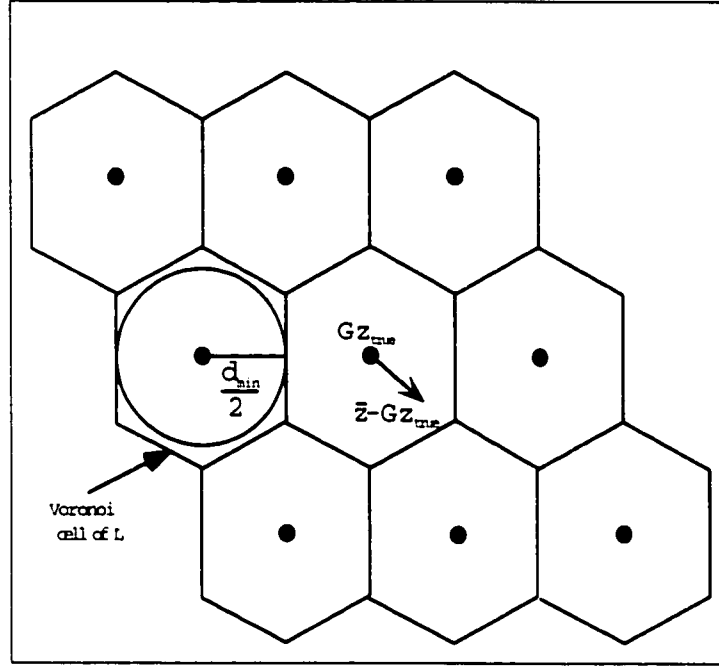
Figure 5.1: Lattice generated by the generator matrix **G**

Consider the set of columns which constitute the lattice generator, $\mathbf{G} = [\mathbf{g}_1 \ldots \mathbf{g}_q]$. We will describe the Gram-Schmidt orthogonalization of **G** as $\mathbf{G}^* = [\mathbf{g}_1^* \ldots \mathbf{g}_q^*]$ where

$$\mathbf{g}_j^* = \mathbf{g}_j - \sum_{i=1}^{j-1} \frac{\mathbf{g}_j^T \mathbf{g}_i^*}{\|\mathbf{g}_i^*\|^2} \mathbf{g}_i^*, \quad j = 1 \ldots q \tag{5.24}$$

It can be shown (see Appendix E) that a lower bound on the value of d_{min} can be found according to:

$$d_{min} \geq min(\|\mathbf{g}_1^*\|_2, \|\mathbf{g}_2^*\|_2, \ldots \|\mathbf{g}_q^*\|_2) \tag{5.25}$$

Consider, as an example, the lattice points generated by the 2-D lattice generator

$$\mathbf{g}_1 = \begin{bmatrix} 0.47 \\ 0.62 \end{bmatrix}, \quad \mathbf{g}_2 = \begin{bmatrix} 0.62 \\ 1.10 \end{bmatrix} \tag{5.26}$$

as shown in Figure 5.2. Since $\mathbf{g}_1$ and $\mathbf{g}_2$ are almost co-linear, the inequality $d_{min} \geq \|g_2^*\|$ clearly provides a very poor lower bound. This situation is typical for the type of geometries encountered in satellite navigation. In order to compute a tighter lower bound on d_{min} we would like the columns of $\{\mathbf{g}_i\}$ to be as linearly independent as possible. Stated differently, we would like to find a matrix, $\bar{\mathbf{G}}$, which generates exactly the same lattice, but for which the columns $\{\bar{\mathbf{g}}_i\}$ are as orthogonal as possible.

The algorithm of Lenstra-Lenstra-Lovatz [1] provides a computationally efficient technique for deriving a new lattice generator matrix $\bar{\mathbf{G}} = \mathbf{GF}$ where $\mathbf{F}$ is a unitary matrix, and all its elements are integer-valued. As a result, $\bar{\mathbf{G}}$ generates exactly the same lattice points as $\mathbf{G}$. However, the columns of $\bar{\mathbf{G}}$, $\{\bar{\mathbf{g}}_i\}$, have some degree of orthogonality, in the sense that

$$\bar{\mathbf{g}}_j = \sum_{i=1}^{j} \mu_{ji} \bar{\mathbf{g}}_i^*, \quad \mu_{jj} = 1, |\mu_{ji}| < \frac{1}{2}, \quad i \neq j \tag{5.27}$$

where $\{\bar{\mathbf{g}}_i^*\}$ are the columns of $\bar{\mathbf{G}}^*$, the Gramm-Schmidt orthogonalization of $\bar{\mathbf{G}}$.

By maintaining some degree of linear independence among the columns $\{\bar{\mathbf{g}}_i\}$, the LLL algorithm tightens the bound on d_{min} which is obtained by the Gram-Schmidt technique, $d_{min} \geq min(\|\bar{\mathbf{g}}_1^*\|^2 \ldots \|\bar{\mathbf{g}}_q^*\|^2)$. The feature is illustrated in Figure 5.2. Notice that the vectors $\bar{\mathbf{g}}_1^*$ and $\bar{\mathbf{g}}_2^*$ are *almost* orthogonal, with the result that $min(\|\bar{\mathbf{g}}_1^*\|^2, \|\bar{\mathbf{g}}_2^*\|^2) > min(\|\mathbf{g}_1^*\|^2, \|\mathbf{g}_2^*\|^2)$. As can be seen, a close bound on d_{min} is established by $\|\bar{\mathbf{g}}_2^*\|$.
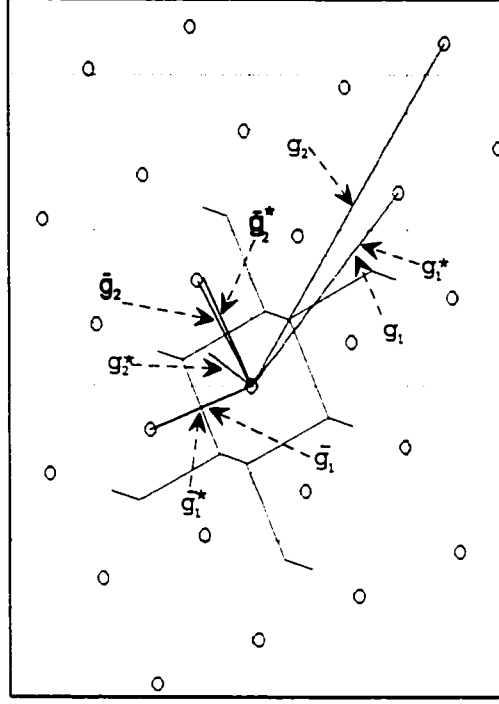
Figure 5.2: Lattice points, lattice generator vectors, and orthogonal basis vectors

Now, $\|\bar{z} - \mathbf{G}z\|^2$ is the sum of q independent normally distributed unit variance random variables. Consequently, this cost has a χ^2 distribution with q degrees of freedom. We denote by $F_{\chi^2}(\chi^2; q)$ the cumulative distribution function of a χ^2 random variable of q d.o.f. Once we have a bound on d_{min}, d, we can find a lower bound on the probability of correct integer selection:

$$Prob\{z_{ML} = z\} \geq F_{\chi^2}\left(\frac{d^2}{4}; q\right) \tag{5.28}$$

This is computed by a lookup into a table describing $F_{\chi^2}(\chi^2; q)$ and is computationally very cheap. Notice that as more measurements are taken over time, and the geometric diversity improves, the magnitude of d_{min} will increase. Consequently, the error involved in integrating the pdf of $\bar{z}$ over a sphere of radius $\frac{d_{min}}{2}$ rather than over

69

the Voronoi cell $\to 0$. Hence, the lower bound on $Prob\{z_{ML} = z\}$ becomes tight[1].

5.IV An Efficient Integer Search Algorithm

We return now to the integer least-squares estimation problem of Equation (5.5).

Replacing $\mathbf{G}$ by $\bar{\mathbf{G}}$, the estimation problem can be reformulated as

$$\bar{z}_{ML} = \arg \min_{z \in \mathbf{Z}^{q \times 1}} (z - \bar{z})^T \mathbf{P}^{-1} (z - \bar{z}) \tag{5.29}$$

where $\bar{z} = \bar{\mathbf{G}}^{-1}\bar{z}$, $\mathbf{P} = (\bar{\mathbf{G}}^T\bar{\mathbf{G}})^{-1}$. The maximum likelihood integer vector which

solves the previous formulation of Equation (5.5) can be found by the transformation

$z_{ML} = \mathbf{F}\bar{z}_{ML}$. Notice that if $\mathbf{P}$ is diagonal, then the expression becomes

$$\bar{z}_{ML} = \arg \min_{z \in \mathbf{Z}^{q \times 1}} \sum_{i=1}^{q} \frac{(z_i - \bar{z}_i)^2}{P_{ii}} \tag{5.30}$$

in which case we can simply find the integers by rounding: $\bar{z}_{ML,i} = \lceil \bar{z}_i \rfloor$. Since $\bar{\mathbf{G}}$

is *almost* orthogonal. $\mathbf{P}$ is *almost* diagonal, and we can use the rounding of $\bar{z}$ as an

initial suboptimal estimate of $\bar{z}_{ML}$, $\bar{z}_{sub}$. Since we have the lower bound $\frac{d_{min}}{2}$ from

Equation (5.25), we know that if $\|\bar{z} - \bar{\mathbf{G}}\bar{z}_{sub}\|_2 < \frac{d_{min}}{2}$ then $\bar{z}_{sub}$ is the global minimum

$\bar{z}_{ML}$. Consequently, the algorithm we employ for attaining z_{ML} is as follows:

- Perform the iterative smoothing technique described in Section 5.III

- Compute $\mathbf{G}$, and $\hat{z}$ and set $\bar{z} = \mathbf{G}\hat{z}$.

---

[1] For highly correlated noise, d_{min} will only increase with geometric diversity; the number of measurements is immaterial. This effect can be accommodated by maintaining off-diagonal elements in the batch correlation matrix, $\mathbf{C}$, as discussed in Section 4.III.

- Perform the LLL on the columns of $\mathbf{G}$ to generate a unimodular matrix $\mathbf{F}$ and create a new lattice generator matrix $\bar{\mathbf{G}} = \mathbf{G}F$ which is almost orthogonal.

- $\mathbf{z}_{sub} \leftarrow \mathbf{F}\lceil \bar{\mathbf{G}}^{-1}\bar{\mathbf{z}} \rfloor$. If $\|\bar{\mathbf{z}} - \mathbf{G}\mathbf{z}_{sub}\|_2 < \frac{d_{min}}{2}$ then $\mathbf{z}_{ML} = \mathbf{z}_{sub}$ and stop.

- $r \leftarrow \|\bar{\mathbf{z}} - \mathbf{G}\mathbf{z}_{sub}\|_2$ and $\bar{\mathbf{z}}_{sub} \leftarrow \mathbf{F}^{-1}\mathbf{z}_{sub}$

- while 1

    - Search for an integral point within ellipsoid $\|\bar{\mathbf{z}} - \bar{\mathbf{G}}\mathbf{z}\|_2 < r$.

    If no such point exists $\mathbf{z}_{ML} \leftarrow \mathbf{F}\bar{\mathbf{z}}_{sub}$ and stop.

    - Let $\bar{\mathbf{z}}_{sub}$ be the integral point found in the previous step. $r \leftarrow \| \bar{\mathbf{z}} - \bar{\mathbf{G}}\bar{\mathbf{z}}_{sub} \|_2$.

    - If $r \le \frac{d_{min}}{2}$ then $\mathbf{z}_{ML} \leftarrow \mathbf{F}\bar{\mathbf{z}}_{sub}$ and stop.

- end.

Note that when we search within the ellipsoid $\|\bar{\mathbf{z}} - \bar{\mathbf{G}}\mathbf{z}\|_2 < r$ we seek an integral point as close to the center of the ellipsoid as possible. An efficient approach to performing this search is discussed in the Appendix G [1].

Once the parameters $\{\bar{N}_s\}$ are identified using any of the techniques discussed above, they can be regarded as constant biases. The receiver uses these estimates in Equation (4.26) to construct prediction error estimates with which to update position estimates with centimeter-level precision in real time. One straightforward method of doing this is

$$\Delta\hat{\theta}(t_k) = \left(\mathbf{H}(t_k)^T \mathbf{R}(t_k)^{-1}\mathbf{H}(t_k)\right)^{-1}\mathbf{H}(t_k)^T\mathbf{R}(t_k)^{-1}\Delta\mathbf{y}(t_k) \qquad (5.31)$$

71

5.V Geometric Interpretation

Having completed a mathematical treatment of the parameter estimation algorithm, this section presents a brief intuitive explanation for the benefits of the LEO signal. Figure 5.3 describes a scenario where a user tracks a single LEO satellite, together with two GPS satellites. For the sake of simplicity, the reference station is ignored, the signals are free of noise, the user receiver clock has no offset from GPS time, and the user as well as the GPS satellites are assumed to be stationary in EBEF coordinates over the course of tracking. Based on the phase measurement of the GPS signals, the user antenna phase center can be placed at any of the vertices of the indicated lattice. The structure of this lattice is determined by the geometry of the GPS satellites, as well as the wavelength of the GPS L1 signals. Since the cycle ambiguity, or bias parameter, for the LEO is not initially known, all the user can directly measure is the change in phase as the LEO moves from one position to another. Each of these measurements place the user on a hyperboloid in space. After several such measurements, the user may be placed at the interSection of all of these hyperboloids. Notice that the user's position estimate is infinitely sensitive on the line perpendicular to the plane of the page. Nonetheless, the information from just a single LEO is sufficient to resolve on which vertex of the lattice the user resides.
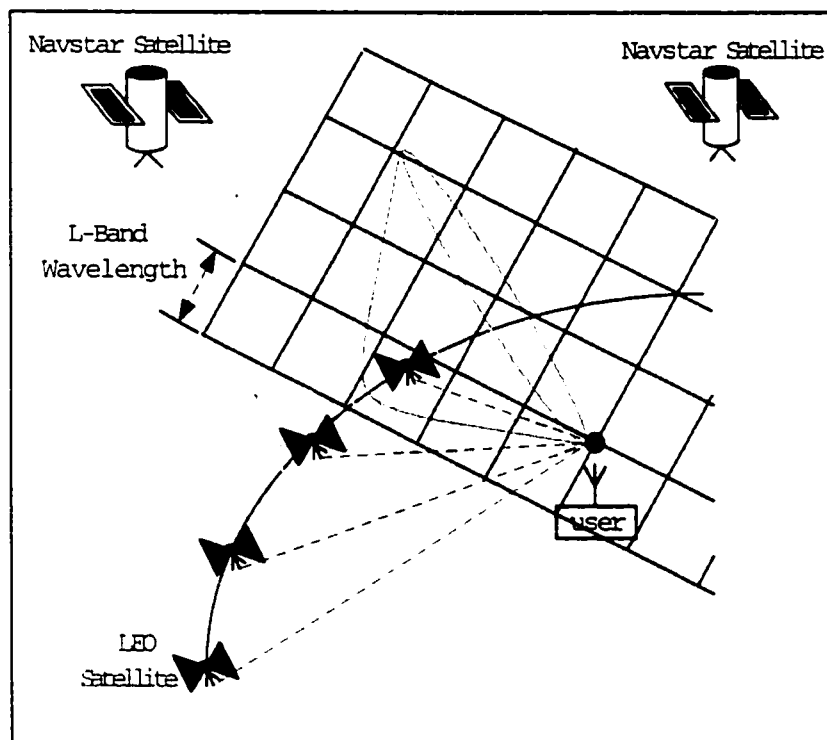
Figure 5.3: Geometric interpretation of the boons of a LEO satellite signal

Chapter 6

Accommodating some Idiosyncratic Systems for Navigation

6.I Satellites with Multiple-Beam Downlinks
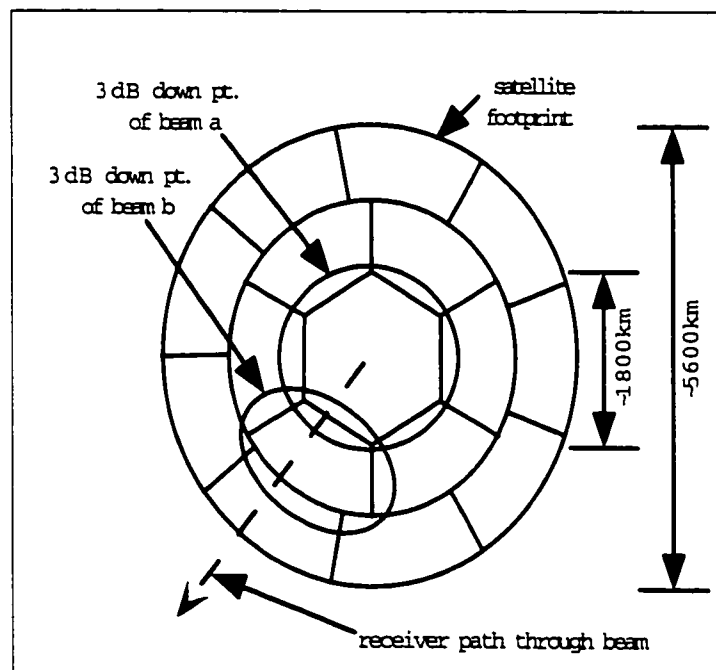
Figure 6.1: Beam configuration on the S-band Globalstar downlink

In Sections 4 and 4.II, it was assumed that each satellite footprint was constructed with a single beam so that continuous carrier-phase data could be accumulated over the duration of tracking. However, rather than transmit a single beam for the satellite's footprint, as in the GPS case, some LEOS transmit multiple beams. As shown in Figure 6.1 which roughly resembles the Globalstar downlink, each beam covers a portion of the satellite footprint, which is nadir stabilized. We may assume that each beam is modulated differently, and has a phase offset relative to adjacent beams. Imagine a receiver moves from beam a to beam b. There arises an interval of a few seconds between reaching the $3dB$-down point of beam b and the $3dB$-down point of beam a. During this interval, the receiver simultaneously tracks both beams. Before hand-over from beam a to beam b at time t_0, the receiver calculates the phase difference between the two beams, $\phi_a(t_0) - \phi_b(t_0)$. The receiver then adds this difference to the phase measured on beam b at some later time t_1. The resultant phase measurement then becomes $\phi_a(t_0) + [\phi_b(t_1) - \phi_a(t_0)]$, which is corrected for any offset between the beams[1].

6.II Compensating for the Effects of a Bent-pipe Communication Payload

We have assumed in Section 4 that the signal arises onboard the satellite. However, for a bent-pipe communication payload, the satellite actually downconverts and then retransmits signals received from ground-based uplink stations. This does not change the conceptual approach, but simply requires that additional terms be taken into account in the estimation strategy. An example of a bent-pipe system configuration is illustrates in Figure 6.2. Consider the phase of the signal generated at the ground

---

[1]This technique has not yet been implemented in practice.

terminal:
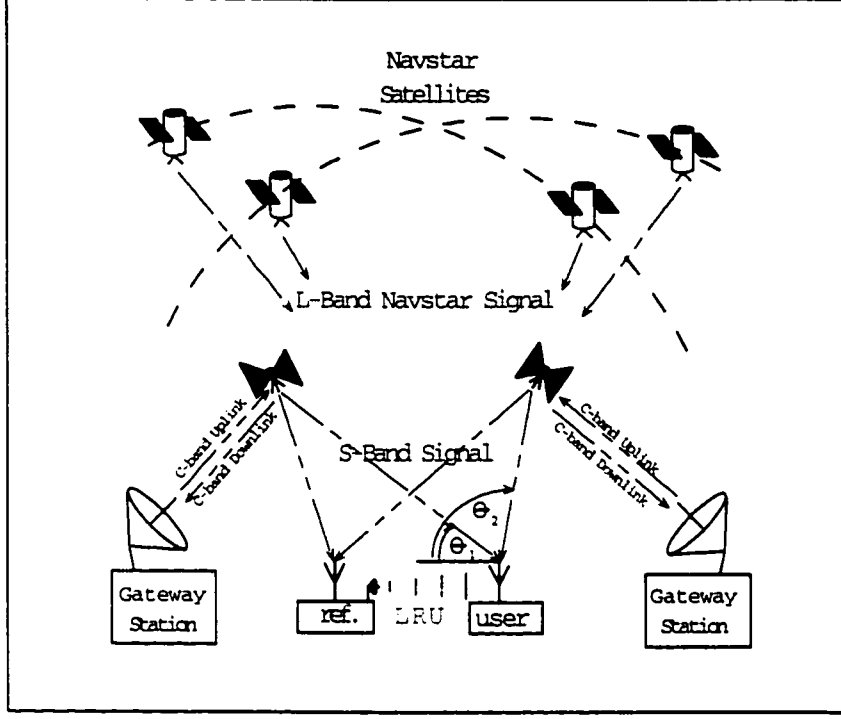
Figure 6.2: System overview displaying bent pipe communication configuration

$$\Psi_g(t_g) = \omega_g \left[t_g + \tau_g(t_g) \right] \tag{6.1}$$

We will ignore τ_g since its effect on the differential phase measurement is negligible. Using similar reasoning to that of Section 4.I, the phase of the uplink signal incident at the satellite at time t_s can be described:

$$\Psi_{gs}(t_s) = \omega_g \left(t_s - \frac{1}{c} p_{gs}(t_s) \right) + \nu_{gs} \tag{6.2}$$

where $p_{gs}(t_s)$ is the distance from the ground terminal to the satellite at time t_s; the

77

expression $t_s - \frac{1}{c}p_{gs}(t_s)$ describes the time at which the transmission was made; and ν_{gs} represents all the phase disturbances on the path from ground to satellite, which will *almost* cancel out in the differential measurement. The satellite downconverter mixes the incident signal with another at frequency $\omega_g - \omega_s$. The phase of the down-converted signal which the satellite transmits is then

$$\Psi_s(t_s) = \omega_s\left[t_s + \tau_s(t_s)\right] - \frac{\omega_g}{c}p_{gs}(t_s) - \omega_g\tau_s(t_s) + \nu_{gs} \qquad (6.3)$$

The phase of the satellite signal output from the LNA of the user's receiver at time t_u is then approximately

$$
\begin{aligned}
\Psi_{su}(t_u) = \; & \omega_s\left(t_u - \frac{1}{c}p_{su}\left(t_u - \frac{p_{su}(t_u)}{c}\right)\right) + \nu_{gs} + \nu_{su} \\
& + (\omega_s - \omega_g)\tau_s\left(t_u - \frac{p_{su}(t_u)}{c}\right) - \frac{\omega_g}{c}p_{gs}\left(t_u - \frac{p_{su}(t_u)}{c}\right)
\end{aligned}
$$

$$(6.4)$$

where ν_{su} contains all the phase disturbances on the satellite-to-user path. Consequently, we find the user's phase measurement corresponding to Equation (4.7)

$$
\begin{aligned}
\phi_{su}(t_u) \; = \; & \omega_s\tau_u(t_u) + \frac{\omega_s}{c}p_{su}\left(t_u - \frac{p_{su}(t_u)}{c}\right) + (\omega_g - \omega_s)\tau_s\left(t_u - \frac{p_{su}(t_u)}{c}\right) \\
& + \frac{\omega_g}{c}p_{gs}\left(t_u - \frac{p_{su}(t_u)}{c}\right) - \nu_{gs} - \nu_{su} - N_{su}2\pi
\end{aligned}
$$

$$(6.5)$$

Similarly, the phase measurement made at the reference at time t_r is

$$\phi_{sr}(t_r) = \omega_s \tau_r(t_r) + \frac{\omega_s}{c} p_{sr}\left(t_r - \frac{p_{sr}(t_r)}{c}\right) + (\omega_g - \omega_s)\tau_s\left(t_r - \frac{p_{sr}(t_r)}{c}\right)$$

$$+ \frac{\omega_g}{c} p_{gs}\left(t_r - \frac{p_{sr}(t_r)}{c}\right) - \nu_{gs} - \nu_{sr} - N_{sr}2\pi \tag{6.6}$$

As discussed in Section 4.I, the user matches the tags on the measurements, and performs the single difference:

$$\phi_s(t) = \phi_{su}(t_u) - \phi_{sr}(t_r) \tag{6.7}$$

Using a Taylor expansion and discarding all insignificant high-order terms, as in Section 4.I, we can recast the measurement in terms of the assigned timetags. The resultant representation of the measurement, corresponding to Equation (4.11) is:

$$\begin{aligned}
\mathcal{O}_s(t) \approx\ & \frac{\omega_s}{c} p_{su}\left(t - \frac{p_{su}(t)}{c}\right) - \frac{\omega_s}{c} p_{sr}\left(t - \frac{p_{sr}(t)}{c}\right) \\
& - \frac{\omega_s}{c} \frac{\partial p_{su}(t)}{\partial t}[\Delta\tau_u(t) + T_u] + \frac{\omega_s}{c} \frac{\partial p_{sr}(t)}{\partial t}[\Delta\tau_r(t) + T_r] \\
& + \omega_s[\tau_u(t) - \tau_r(t)] + (\omega_g - \omega_s)\left[\tau_s\left(t - \frac{p_{su}(t)}{c}\right) - \tau_s\left(t - \frac{p_{sr}(t)}{c}\right)\right] \\
& - \frac{\omega_g}{c} \frac{\partial p_{gs}(t)}{\partial t}[\Delta\tau_u(t) + T_u - \Delta\tau_r(t) - T_r] - \frac{\omega_g}{c} \frac{\partial p_{gs}(t)}{\partial t}\left(\frac{p_{su}(t)}{c} - \frac{p_{sr}(t)}{c}\right) \\
& - \nu_{su} + \nu_{sr} - N_{su}2\pi + N_{sr}2\pi
\end{aligned}$$

$$\tag{6.8}$$

We will consider those terms in the expression which have been introduced by the bent-pipe architecture and cause Equation (6.8) to differ from Equation (4.11). Consider the terms

$$(\omega_g - \omega_s) \left[\tau_s \left(t - \frac{p_{su}(t)}{c} \right) - \tau_s \left(t - \frac{p_{sr}(t)}{c} \right) \right] \qquad (6.9)$$

involving the instabilities of the satellite oscillators. All that has changed from Equation (4.11) is the multiplication factor, which is now $(\omega_g - \omega_s)$ instead of $-\omega_s$. Therefore, the treatment of this term is similar to that of Equation (4.14).

Consider the terms in Equation (6.8) involving $\frac{\partial p_{gs}}{\partial t}$. We rewrite these terms as:

$$- \frac{\omega_g}{c} \frac{\partial p_{gs}(t)}{\partial t} \left[\tau_u(t) - \tau_r(t) \right] + \frac{\omega_g}{c} \frac{\partial p_{gs}(t)}{\partial t} \left[\hat{\tau}_u - \hat{\tau}_r \right]$$
$$- \frac{\omega_g}{c} \frac{\partial p_{gs}(t)}{\partial t} \left[T_u - T_r \right] - \frac{\omega_g}{c} \frac{\partial p_{gs}(t)}{\partial t} \left(\frac{p_{su}(t)}{c} - \frac{p_{sr}(t)}{c} \right) \qquad (6.10)$$

The second can be directly calculated if the position of the ground station and the satellite ephemerides are known; hence it can be actively subtracted out of the measurement. The third term can be ignored, using similar arguments to those of Section 4.I. The fourth term is directly calculable if the receiver knows the satellite ephemeris, the location of the ground uplink, and the rough position of the user using code-phase measurements. Consequently, the fourth term is also calculated and actively subtracted out of the differential measurement. Only the first term must be directly estimated.

Eliminating all terms from Equation (6.8) which are either negligible, or actively subtracted out, the estimate of the resulting measurement corresponding to Equation (4.15) is

$$\bar{\phi}_s(t) \approx \frac{\omega_s}{c} p_{su} \left(t - \frac{p_{su}(t)}{c} \right) - \frac{\omega_s}{c} p_{sr} \left(t - \frac{p_{sr}(t)}{c} \right)$$

$$+ \quad \omega_s \left(1 - \frac{1}{c} \frac{\partial p_{sr}(t)}{\partial t} - \frac{\omega_g}{\omega_s c} \frac{\partial p_{gs}(t)}{\partial t} \right) [\tau_u(t) - \tau_r(t)]$$

$$- \quad (N_{su} - N_{sr}) 2\pi + (\mu_{su} - \mu_{sr}) + (n_{su} - n_{sr}) \tag{6.11}$$

Following the steps outlined in Sections 4.I and 4.II, we find the measurement approximation corresponding to Equation (4.23):

$$\bar{y}_s(t) = p_{su} \left(t - \frac{p_{su}(t)}{c} \right) - p_{sr} \left(t - \frac{p_{sr}(t)}{c} \right) +$$

$$\left(1 - \frac{1}{c} \frac{\partial p_{su}(t)}{\partial t} - \frac{\omega_g}{\omega_s c} \frac{\partial p_{gs}(t)}{\partial t} \right) c\bar{\tau}(t) - \bar{N}_s \lambda_s + n_s \tag{6.12}$$

The observation matrix for the time-varying parameters, corresponding to Equation (4.25), becomes

$$\mathbf{h}_s(t) = \left[\frac{\hat{\mathbf{p}}_{su} \left(t - \frac{\hat{p}_{su}(t)}{c} \right)^T}{\hat{p}_{su} \left(t - \frac{\hat{p}_{su}(t)}{c} \right)} \quad 1 - \frac{1}{c} \frac{\partial \hat{p}_{su}(t)}{\partial t} - \frac{\omega_g}{\omega_s c} \frac{\partial p_{gs}(t)}{\partial t} \right] \tag{6.13}$$

Similarly, the estimate of our prediction error, corresponding to Equation (4.26) becomes

$$\Delta y_s(t) = \hat{p}_{su} \left(t - \frac{\hat{p}_{su}(t)}{c} \right) - p_{sr} \left(t - \frac{p_{sr}(t)}{c} \right) \tag{6.14}$$

$$+ \quad \left(1 - \frac{1}{c} \frac{\partial \hat{p}_{su}(t)}{\partial t} - \frac{\omega_g}{\omega_s c} \frac{\partial p_{gs}(t)}{\partial t} \right) c\hat{\bar{\tau}}(t) - \hat{\bar{N}}_s \lambda_s - \bar{y}_s(t)$$

and we may proceed with the estimation as described in Section 4.II.

6.III   Unstable Oscillators: Calibrating the LEO Oscillator using Navstar Satellites

In this section, we describe how the frequency offset, or clock offset rate of the LEO oscillator can be calibrated using a GPS signal. This algorithm is only necessary for oscillators that have long-term frequency instabilities, or offsets, on the order of $1 : 10^7$. Some of the mathematical steps are closely related to those described in detail above, so these stages have been left out of the explanation. The technique described here has been designed to be implemented completely with software, and requires no additional front-end hardware in the receiver. We will assume a bent-pipe communication architecture for generality; the additional terms can simply be dropped for simpler systems.

We can describe the phase measurements made for a bent-pipe LEO satellite L, and a Navstar satellite N at the reference receiver as:

$$\phi_{Lr}(t_r) = \omega_L \left[t_r + \tau_r(t_r) \right] - \Psi_{Lr}(t_r) - N_{Lr} 2\pi \qquad (6.15)$$

$$\phi_{Nr}(t_r) = \omega_N \left[t_r + \tau_r(t_r) \right] - \Psi_{Nr}(t_r) - N_{Nr} 2\pi \qquad (6.16)$$

In order to cancel out the error due to the receiver's oscillator drift, the microprocessor performs a weighted difference between the phase of the two satellite signals to find a calibration phase

$$\phi_c(t_r) = \phi_{Lr}(t_r) - \frac{\omega_L}{\omega_N} \phi_{Nr}(t_r) \qquad (6.17)$$

The incident phase from each of the the satellites may be described:

$$\Psi_{Lr}(t_r) = \omega_L \left(t_r - \frac{1}{c} p_{Lr} \left(t_r - \frac{p_{Lr}(t_r)}{c} \right) \right) - \frac{\omega_g}{c} p_{gL} \left(t_r - \frac{p_{Lr}(t_r)}{c} \right)$$

$$+ (\omega_L - \omega_g) \tau_L \left(t_r - \frac{p_{Lr}(t_r)}{c} \right) - \mu_{Lr} - n_{Lr} \qquad (6.18)$$

$$\Psi_{Nr}(t_r) = \omega_N \left(t_r - \frac{1}{c} p_{Nr} \left(t_r - \frac{p_{Nr}(t_r)}{c} \right) \right) + \omega_N \tau_N \left(t_r - \frac{p_{Nr}(t_r)}{c} \right) - \mu_{Nr} - n_{Nr}$$

where the subscript g refers to the ground uplink station, discussed in Section 6.II. The resultant expression for the weighted difference is found to be:

$$\phi_c(t_r) = \omega_L \tau_N \left(t_r - \frac{p_{Nr}(t_r)}{c} \right) - \frac{\omega_L}{c} p_{Nr} \left(t_r - \frac{p_{Nr}(t_r)}{c} \right) + \frac{\omega_L}{c} p_{Lr} \left(t_r - \frac{p_{Lr}(t_r)}{c} \right)$$

$$+ \frac{\omega_g}{c} p_{gL} \left(t_r - \frac{p_{Lr}(t_r)}{c} \right) + (\omega_g - \omega_L) \tau_L \left(t_r - \frac{p_{Lr}(t_r)}{c} \right)$$

$$- N_{Lr} 2\pi + \frac{\omega_L}{\omega_N} N_{Nr} 2\pi + \mu_{Lr} - \frac{\omega_L}{\omega_N} \mu_{Nr} + n_{Lr} - \frac{\omega_L}{\omega_N} n_{Nr} \qquad (6.19)$$

The 2nd, 3rd and 4th terms are directly calculated and subtracted from the measurement by the reference receiver which knows the location of the ground uplink station, as well as that of the LEO and Navstar satellite. After subtracting out these terms, the calibration measurement becomes:

$$\bar{\phi}_c(t_r) = (\omega_g - \omega_L) \tau_L \left(t_r - \frac{p_{Lr}(t_r)}{c} \right) + \omega_L \tau_N \left(t_r - \frac{p_{Nr}(t_r)}{c} \right)$$

$$- N_{Lr} 2\pi + \frac{\omega_L}{\omega_N} N_{Nr} 2\pi + \mu_{Lr} - \frac{\omega_L}{\omega_N} \mu_{Nr} + n_{Lr} - \frac{\omega_L}{\omega_N} n_{Nr} \qquad (6.20)$$

For the purpose of this calibration, we consider the LEO's clock offset, τ_L, to be a linear function of time as a result of a frequency offset in the satellite oscillator. Since

83

the GPS clock is stable to $1:10^{13}$, we regard τ_N as constant. The reference receiver calculates the change in calibration phase $\Delta\bar{\phi}_c$ over an interval of roughly one second, Δt, to find

$$\frac{\Delta\bar{\phi}_c}{\Delta t} \approx (\omega_g - \omega_L)\frac{\partial \tau_L}{\partial t} \tag{6.21}$$

from which $\frac{\partial \tau_L}{\partial t}$ can be calculated with good accuracy.

6.IV   LEO Satellites using TDMA Downlinks

It should be noted that the fundamental technique of augmenting GPS with LEOS for geometric diversity is equally applicable to TDMA downlinks, where the LEO satellite signals arrive in bursts of a few μsec. The time from the start of one burst to the start of the next is termed the scan period, T_s. The time duration of each burst is termed the receive time, T_r. It has been demonstrated by Cohen [10] that continuous carrier-phase tracking of GPS C/A code-type signals can be achieved with high integrity for $T_r = 2$ $msec$, and $T_s = 12$ $msec$. Although LEOS signals show more Doppler shift than GPS signals, it is well known in the art that a third order phase-locked loop can be implemented to maintain a running estimate of phase ϕ, phase rate $\frac{\partial \phi}{\partial t}$, and phase acceleration $\frac{\partial^2 \phi}{\partial t^2}$. Hence, the change in phase due to satellite motion can be estimated over T_s to maintain phase lock. Two fundamental limitations on the technique exist. The first concerns the stability of the satellite and receiver oscillators required to guarantee that cycle slips do not occur between bursts. If A is the Allan variance of the limiting oscillator over period T_s, we require

$$\frac{A\omega_s T_s}{2\pi} \ll 1 \qquad\qquad (6.22)$$

For example, for Ka band downlinks for which $\frac{\omega_s}{2\pi} \approx 30\ GHz$, and $T_s \approx 25\ msec$, we require $A \ll 1.3 \times 10^{-9}$. This is achievable with a good quartz oscillator [13], as is shown in Figure 6.3 which displays the Allan variance for various types of oscillators. The second limitation involves aliasing due to the dynamics of the receiver platform. For $T_s = 25\ msec$, for example, the highest frequency component of the platform dynamics should not exceed half of the corresponding sampling frequency, or $20Hz$.
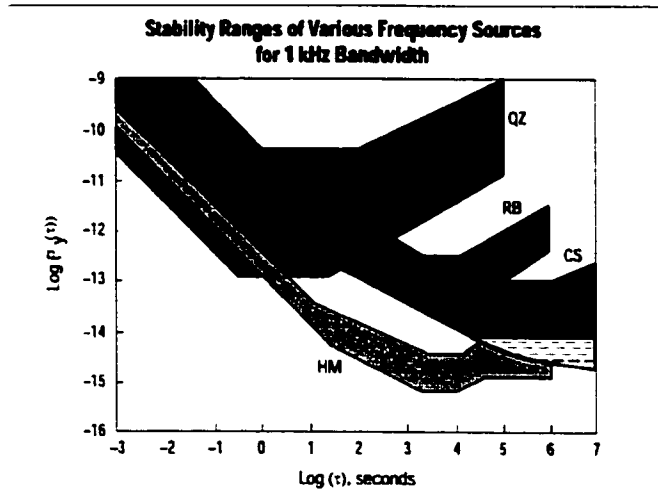
Figure 6.3: The range of Allan Variance values for various time-keeping devices. QZ = Quartz crystal, RB = Rubidium gas-cell, HM = active Hydrogen mazer, CS = Cesium beam

6.V Non-GPS Navigation Signals

In our discussion of the carrier-phase positioning algorithm, we have assumed that LEOS are used to augment the Navstar GPS satellite fleet. It should be noted that Navstar GPS satellites have utility to the extent that they provide:

- Additional carrier-phase signal sources, which ensure that the parameter-estimation problem is over-determined.

- Code-phase navigation signals which allow for correlation of the user and reference receiver clocks to better than $\sim 1 \mu sec$ and also enable the receivers to achieve initial position estimates accurate to the meter-level.

Other navigation satellites exist, and are planned, which could also fulfill both of these functions. Such systems include Russia's Glonass, WAAS, and Europe's proposed Satellite Civilian Navigation System which will include a LEO segment with highly stable downlink frequencies. The technique of exploiting LEO satellites for geometric diversity is equally applicable to these other navigation satellites. For the general case of a mobile user, four such navigation signals should be available. If another means is used to initially synchronize the reference and receiver clocks, specialized code phase navigation signals become unnecessary.

The technique described in Section 4 can resolve integer cycle ambiguities on carrier-phase signals for a mobile user as long as a total of five satellites are in view, at least one of which should be LEO. The primary constraint on which satellite systems can be used is the availability of signal sources. Ideally, to rapidly constrain all the degrees of freedom in the positioning problem, two or more of these satellites should

be in Low Earth Orbit.

6.VI   Non-Differential Position Estimates

The essential technique of augmenting GPS with LEOS for geometric diversity is equally applicable to the non-differential setting. To examine how a user receiver might proceed with non-differential position estimation, consider the first-order expansion of the phase measurement in Equation (4.9)

$$
\begin{aligned}
\phi_{su}(t_u) &\approx \frac{\omega_s}{c} p_{su}\left(t - \frac{p_{su}(t)}{c}\right) + \omega_s \tau_u(t) - \frac{\omega_s}{c}\frac{\partial p_{su}(t)}{\partial t}[\tau_u(t) + T_u] \\
&\quad - \omega_s \tau_s(t - \frac{p_{su}(t)}{c}) - N_{su}2\pi + \mu_{su} + n_{su}
\end{aligned}
$$

Since there is no need to initially estimate and compensate for clock offset, $\hat{\tau}_u$ has been dropped from the expression. The term $\frac{\omega_s}{c}\frac{\partial p_{su}(t)}{\partial t}T_u$ can be ignored with distance-equivalent error of $< 1mm$ for $|T_u| < 0.1\mu sec$ and satellites at $1400\ km$. Consider now $\tau_s(t - \frac{p_{su}(t)}{c})$. For highly stable satellite oscillators, such as atomic oscillators, the user can be conveyed the necessary information to model the clock term. Alternatively, a highly stable clock can be modeled linearly as $\tau_s(t) = \tau_{so} + \tau_{s1}t$. Using the clock-calibration technique described in Section (6.III), the user may directly estimate and subtract out the term $(t - \frac{p_{su}(t)}{c})\tau_{s1}$. Using Ionospheric/Tropospheric models (see Parkinson [38]) and/or dual frequency ionospheric calibration, the user receiver could estimate and largely subtract out the error terms n_{su}, leaving a residual Δn_{su}. Converting the resultant estimate to distance-equivalent form,

87

$$y_{su}(t_u) = p_{su}\left(t_u - \frac{p_{su}(t_u)}{c}\right) + \left(1 - \frac{1}{c}\frac{\partial p_{su}(t_u)}{\partial t}\right)c\tau_u(t_u) - c\tau_{s0} - \lambda_s N_{su} + \frac{\lambda_s}{2\pi}\mu_{su} + \Delta n_{su}$$

$$(6.23)$$

Using one of the Navstar satellites, say satellite 1, as a *reference* satellite for differencing, we make similar redefinitions to those described in Section 4.II

$$
\begin{aligned}
\bar{y}_{su}(t_u) &= y_s(t_u) + \hat{N}_{1u} \\
\bar{N}_{su} &= \left(N_{su} - \frac{\mu_{su}}{2\pi} + \frac{c\tau_{s0}}{\lambda_s}\right) - \frac{\lambda_1}{\lambda_s}(N_{1u} - \frac{\mu_{1u}}{2\pi}) \\
\bar{\tau}_u(t_u) &= \tau_u(t_u) - \frac{\lambda_1}{c}\left(N_{1u} - \hat{N}_{1u} - \frac{\mu_{1u}}{2\pi}\right)
\end{aligned}
$$

$$(6.24)$$

The measurement may then be described

$$\bar{y}_{su}(t_u) = p_{su}\left(t_u - \frac{p_{su}(t_u)}{c}\right) + \left(1 - \frac{1}{c}\frac{\partial p_{su}(t_u)}{\partial t}\right)c\bar{\tau}_u(t_u) - \lambda_s\bar{N}_{su} + \Delta n_{su} \quad (6.25)$$

One may then proceed with a similar estimation strategy to that described in Section 4.II. with the positioning accuracy depending primarily on the magnitude of Δn_{su} as well as ephemeris errors.

Chapter 7

Phase Measurement Firmware

In this section, we describe the technique by which phase is accumulated and measured for the LEO satellite downlinks. The two techniques which will be discussed are designed to to achieve the following objectives:

- The time-tagging of the phase measurements must be precise to $100nS$ in order to achieve distance-equivalent errors less than $1mm$[1].

- The instant of phase measurement must be synchronized with the GPS sampling instant. Any delay between the phase-sampling instant of the GPS receiver and the LEO receiver must remain constant to within $100\ nS$ over the course of tracking the LEO, so that distance-equivalent errors less than $1\ mm$ are maintained.

- The phase-tracking assembly should be implemented without the need for additional hardware, such as phase accumulators or registers which need to be strobed by signals synchronized to the GPS hardware.

---

[1] This error is independent of the baseline - see Section 4.I.

The latter requirement is unusual, and is motivated by the desire that the centimeter-level navigation system should operate on pre-built receiver hardware (such as a portable phone device). While changes to the microprocessor firmware are relatively cost-efficient and easily implemented, changes to device hardware can require considerable additional investment. In addition, as more processing is performed in firmware, rather than hardware, the size, cost and power consumption of receivers goes down.

7.I   Implementing an Open Loop NCO
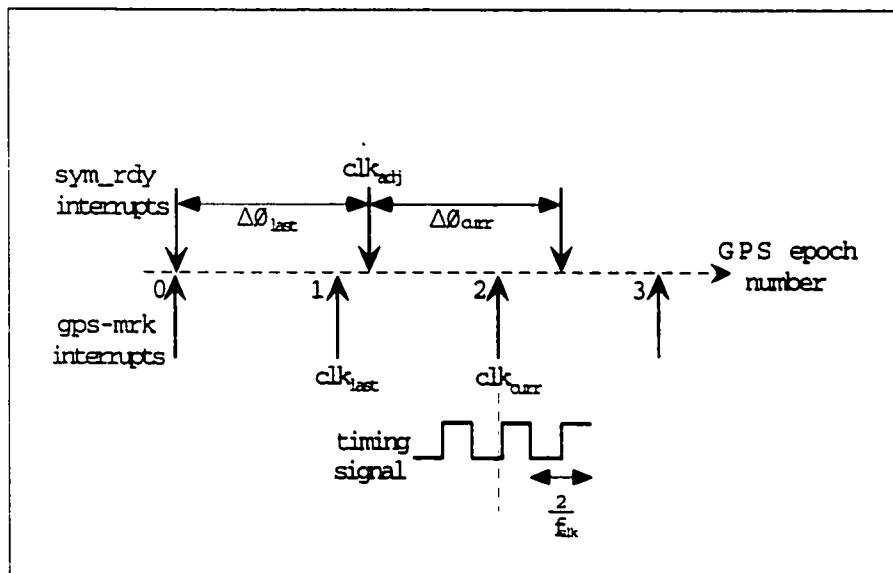
Figure 7.1: Interrupts which drive the open loop model of the NCO implemented in firmware

The first technique involves implementing a firmware model of the hardware NCO, which is driven by the same commands that are uploaded to the hardware NCO. Consider the operation of the LEO NCO, described in Figure 7.2. The phase of the NCO is incremented by $\Delta \phi$ every $\frac{1}{f_o}$ seconds, where the oversampling frequency $f_o = L \times R \times D \times 8$ as described in Section 3.II.E. The phase output by the NCO,

90
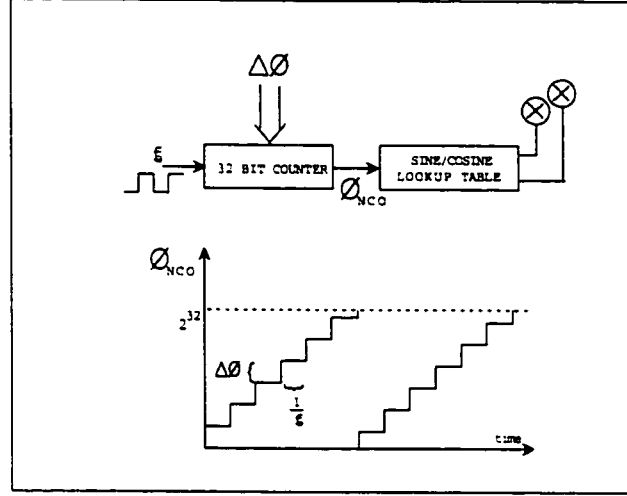
Figure 7.2: Block structure of a generic hardware NCO

as shown in the figure, is modulus 2^{32}, consequently 2^{32} corresponds to 2π in the sine/cosine lookup table. The microprocessor is driven by four signals:

- symbol ready (sym-rdy) - From the LEO correlator hardware discussed in Section 3.II.C.

- millisecond marker (ms-mrk) - This is a digital clock signal, of 50% duty cycle, the leading edge of which marks milliseconds, synchronized to GPS time.

- pulse per second (pps)- This signal is also synchronous to GPS time. This is used to align the initial sampling times of the LEO and GPS receivers.

- Clock signal (clk) - This signal is tied to the oscillator of the GPS receiver. The timing standard used by the LEO microprocessor, as well as by the 32 bit phase accumulator, must be synchronized to this signal. The simplest solution (which we ultimately adopted) is to drive all the LEO hardware using the clk signal of frequency f_{clk}. The microprocessor counter used for phase time-tagging is clocked at $\frac{f_{clk}}{2}$.

91

In this description, we focus attention on the sym-rdy and the ms-mrk signals, around which the phase-measurement routine revolves. The sym-rdy marker is a strobe generated by the LEO hardware at the frequency of $\frac{1}{rate}$, indicating that an output of the LEO accumulator is available. sym-rdy generates an interrupt which initiates an iteration of the phase-locked-loop control law, at the end of which a new $\Delta\phi$ value is uploaded to the 32-bit counter. The time at which this adjustment occurs, measured according to the clk signal, is clk_{adj}.

The phase measurement in the GPS receiver is associated with the leading edge of the ms-mrk signal. In the LEO receiver, the ms-mrk leading edge initiates an interrupt, which records the current time, clk_{cur}, and measures the change in oscillator phase since the last epoch. Consider the time-line of interrupts as shown in Figure 7.1, where we have assumed that $\frac{1}{rate} > 1\ ms$. The labels clk_{last}, clk_{curr}, $\Delta\phi_{last}$ and $\Delta\phi_{curr}$ are assigned assuming the phase increment is being calculated at the 2ms marker.

At each ms-mrk interrupt, the calculation of phase for the open-loop NCO proceeds as follows:

If $clk_{adj} > clk_{last}$

$$\phi_{curr} = \phi_{last} + (clk_{adj} - clk_{last})\Delta\phi_{last} + (clk_{curr} - clk_{adj})\Delta\phi_{curr} \qquad (7.1)$$

else

$$\phi_{curr} = \phi_{last} + (clk_{curr} - clk_{last})\Delta\phi_{curr} \qquad (7.2)$$

7.I.A   Accuracy of the Open Loop NCO

It is not intuitive that an open-loop NCO can maintain a measure of the actual phase which remains accurate enough for centimeter-level navigation. It can be clearly shown (and has been experimentally verified) that this is in fact achievable. Using $f_{clk} = 23.36$ MHz, time-tagging can be performed to a precision of roughly $0.1\mu S$. Consider the case, illustrated in Figure 7.1 at 2ms, where the leading edge of the timing signal occurs just after clk_{curr} is recorded. Since this leading edge will be included in the phase measurement at 3ms, the fractional cycle missed in measuring the current millisecond will be included in the subsequent measurements. Hence errors errors due to time-tagging precision are not cumulative. Consequently, the accumulated timing pulses counted over several ms-mrk interrupts will be accurate to within 2 cycles of f_{clk}. However, since the $\Delta\phi$ are constantly changing, inaccuracy will arise if each $\Delta\phi$ is not applied for the correct period of time. Since the phase acceleration of the LEO downlink doesn't exceed 60 Hz/sec, for the pathological case, this phase error would be $0.06 Hz/ms \times \frac{1}{11.68e3} ms = 5 \times 10^{-6} cycles/ms$ or $10^{-3} cycles$ after tracking phase for 4 minutes. This error is well below the system noise floor.

7.I.B   Numerical Precision

The primary error affecting accuracy of the open-loop NCO is quantization noise. The numerical precision with which the calculations of Equations (7.1, 7.2) are performed can result in considerable quantization errors for 32-bit floating point processors. For example, consider an f_{offset} of roughly $500kHz$ - see Section 3.II.C - tracked for only $10sec$, accumulating a phase of 5×10^6 cycles. Assume now that 24 bits are used for the floating-point mantissa, as is the case for the TMS320 microprocessor.

The quantization error can be modeled as a random variable of uniform distribution between -0.3 and 0.3 cycles, which is added at each phase accumulation of Equation (7.1, 7.2). This numerical precision issue is resolved using extra 32-bit words, and purely integer multiplication in the receiver assembly code as illustrated in Figure 7.3.
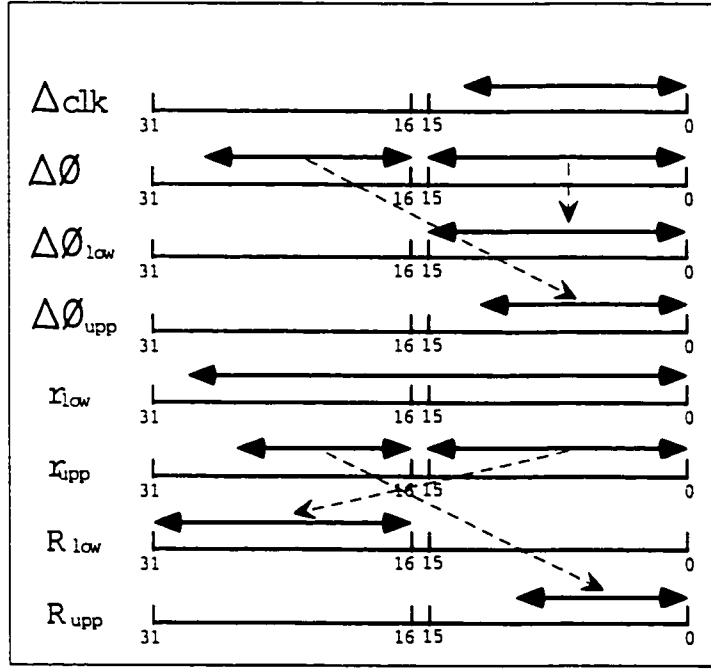
Figure 7.3: Sequence of steps used to avoid quantization noise for the open loop NCO model

The register Δclk stores the number of cycles between ms-mrk interrupts, which requires 14 bits. The register $\Delta \phi$ stores the increment made to the counter upon each leading edge of the oversampling clock, f_o. $\Delta \phi$ requires 29 bits. We initialize a register $\Delta \phi_{low}$ which stores the lower 16 bits of $\Delta \phi$, and $\Delta \phi_{upp}$ which contains the upper 13 bits of $\Delta \phi$, down-shifted. We then perform the integer multiplications:

$$r_{low} = \Delta \phi_{low} \Delta clk$$

94

$$r_{upp} = \Delta\phi_{upp}\Delta clk \tag{7.3}$$

The upper 16 bits of r_{upp} are moved to the lower 16 bits of R_{upp}, the lower 16 bits of r_{upp} are moved to bits 16-31 of R_{low}. The accumulation of the phase is then performed

$$\phi_{low} = \phi_{low} + R_{low} + r_{low} \tag{7.4}$$

and the any carry is stored in c. Then,

$$\phi_{upp} = \phi_{upp} + R_{upp} + c \tag{7.5}$$

ϕ_{low} now stores the fractional component of the phase (2^{32} corresponds to 2π), ϕ_{upp} stores the number of complete cycles. Note that these phase measurements need to be scaled by $\frac{f_{clk}}{2f_o}$, the number of cycles of the oversampling clock for each cycle of the timing signal, in order to obtain the true phase measurement.

7.I.C Resolving Interrupt Timing Issues

Since the ms-mrk service routine and the sym-rdy routine each operate on variables that are changed by the other routine, it is important that the respective interrupts not occur in the midst of crucial operations. The simplest approach is to disable all interrupts while a particular interrupt service routine is running. The result is displayed in Figure 7.4. In this case, the hardware generating the sym-rdy marker is driven by a different clock from that generating the ms marker. Consequently, the markers slide relative to one another. clk_{adj} is set at the end of the sym-rdy service routine. clk_{last} and clk_{curr} are set at the beginning of the ms-mrk service routine. The
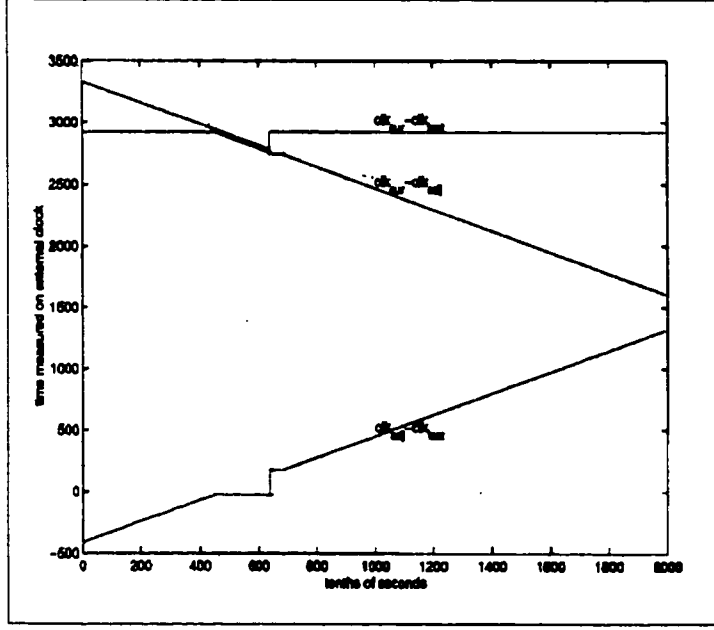
Figure 7.4: Illustrating the complexities of multiple firmware interrupts: a plot of crucial timing signals

large horizontal segment of the curve $clk_{adj} - clk_{last}$ arises since the ms-mrk leading edge arrives soon after the sym-rdy marker, while the sym-rdy service routine is still operating. Since the ms-mrk service routine is only executed once the sym-rdy routine has exited, $clk_{adj} - clk_{last}$ remains constant. The step of roughly 200 cycles at ~ 65 seconds occurs when the ms-mrk interrupt occurs before the sym-rdy interrupt, so that the sym-rdy routine is executed only when the ms routine has exited. Since each ms-mrk needs to be precisely time-tagged, and a delay of the sym-rdy disturbs the PLL control law, this situation is unacceptable. The solution is to re-enable all other interrupts at the start of each service routine, but to disable interrupts when certain crucial operations are underway. In our implementation, there are three such crucial Sections of code, they are:

- The sequence of commands in which variables are combined to update the phase

96

as per Equations (7.1,7.2).

- The commands which record clk_{adj} and upload the new $\Delta\phi$ to the hardware NCO.

- The commands which record clk_{curr} and associate it with the current $\Delta\phi$.

7.I.D   Hardware for Driving the TMS 320 Interrupts

If any ms-mrk interrupt is either missed, or double-counted by the microprocessor, the effect on the phase measurement is catastrophic. Consequently, a noise-free, precise interrupt signal needs to be generated by hardware. The TMS320 will register one interrupt if the relevant pin is held low for one or two falling edges of an internal clock, which operates at a frequency of $\frac{f_{clk}}{2}$. If the pin is held low for more than two falling edges multiple interrupts may be recorded, again with catastrophic effects on phase tracking. In order to generate the correct pulse at each rising edge of the ms signal, which has a 50% duty cycle, the hardware of Figure 7.5 was used. Note that the digital circuitry must be implemented with high-speed bipolar hardware in order to realize the correct pulse shape and duration. This circuitry has been implemented as part of the synchronization circuitry for the receiver pc-board, as discussed in Section 3.II.C.

Note that the delay from the instant of the ms-mrk leading edge to the recording of clk_{cur} in the microprocessor is composed of the digital delay in generating the ms-mrk interrupt pulse, as well as the firmware delay in initializing the interrupt service routine. So long as this delay remains constant over the course of tracking, it is incorporated into the frequency-dependent phase-lag estimated for the LEO front end - see Section 4.II. The only variable delay is that between the leading edge of

97

the ms-mark and the next leading edge of the clock signal, indicated as Δclk in the figure. The hardware maintains this delay below $100nS$.
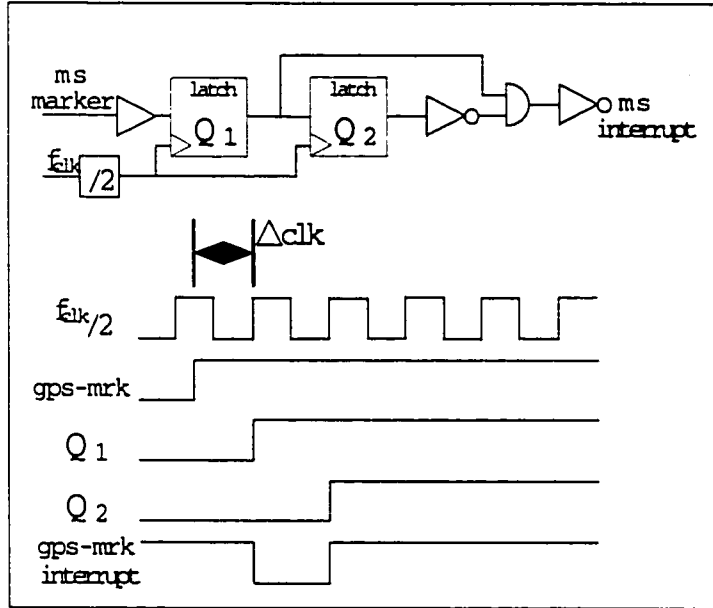
Figure 7.5: Segment of synchronization hardware for generating the millisecond interrupt signal

7.II Implementing the Phase Tracking Assembly in Firmware

While the previous approach is computationally cheap, the primary disadvantage is that the system is not scalable, i.e., a dedicated hardware NCO is necessary for each satellite being tracked. In order to surmount this problem, we have developed a system which implements the entire phase tracking assembly in firmware. The block diagram of Figure 7.6 describes the operation of the software Phase-Locked-Loop (PLL). The description provided here is for the TMS320 Microprocessor operating at a clock speed $f_{clk} = 23.36MHz$, and with the assumption of a maximum if signal bandwidth of 15kHz. It will be clear from the description how the relevant parameters

98
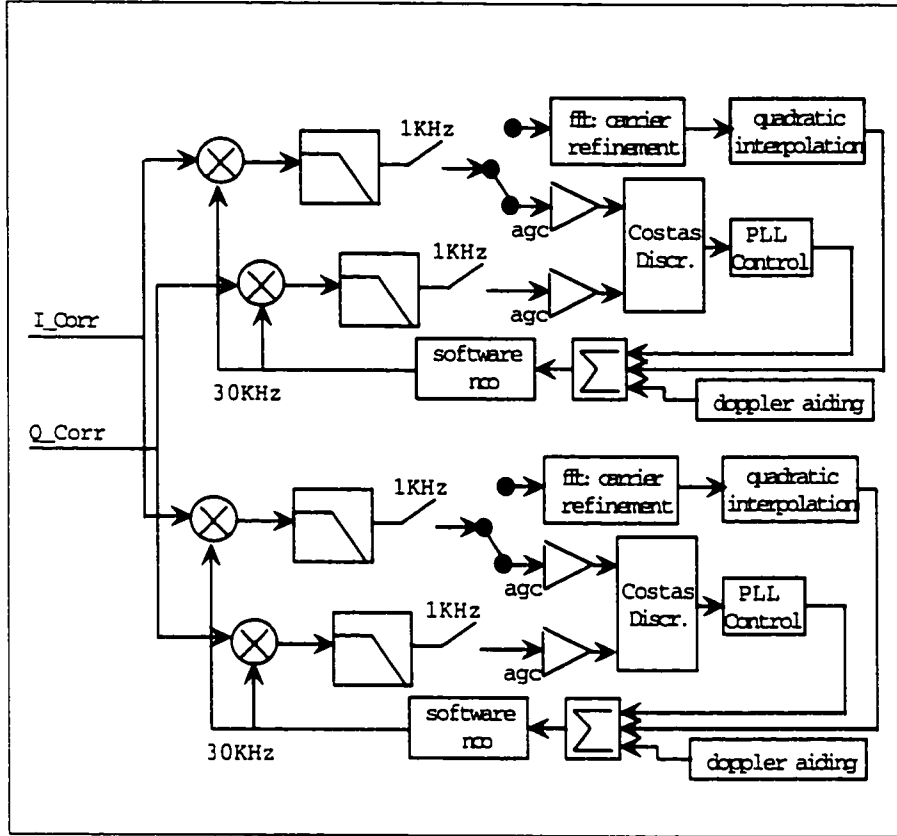
Figure 7.6: Design of a software PLL for tracking multiple Orbcomm satellites

would change for a different hardware and signal configuration. The mixing NCO discussed in Section 3.II.E mixes the incoming signal at a constant frequency $1kHz$ below the lowest expected spectral component of the incoming signal. The correlator codes (see Section 3.II.E) filter out the upper sideband of the mixed signal. The correlator outputs, illustrated as I_{Corr} and Q_{Corr} in Figure 7.6, are sampled at a symbol rate of 30kHz. The three segments of each channel's PLL, which are clocked at 30kHz, and for which code needs to be very efficient are the software NCO, the mixing, and the filtering of the mixed signal.

The NCO is implemented using a cosine lookup table, the filter is implemented using a direct-form II [37] implementation of a $200Hz$ Butterworth lowpass filter. The

99

rate of phase accumulation by the NCO is determined by 3 inputs: the Doppler-aiding parameters, the frequency offset estimated by the carrier refinement algorithm, and the output of the PLL control law. The Doppler-aiding parameters are the coefficients of a third-order polynomial model of the Doppler-shifted frequency as a function of time. This model is derived from the ephemeris prediction software described in Section B. The Doppler-aiding parameters determine the initial frequency of the NCO, which is typically accurate to $100Hz$. The bandwidth of the digital filter must be large enough to accommodate the initial NCO frequency error, but small enough to filter out the signals of other satellites. In this system, the filter is implemented as a third order Butterworth with one-sided passband of $100Hz$. The firmware implementing the mixers, filters and NCO for the two channels executes each iteration in 250 cycles of f_{clk}. Two more channels can be added without exceeding the processing capabilities of the TMS320 microprocessor. The output of the filters is sampled at a rate of $1KHz$. Since the bandwidth of the PLL is roughly 10Hz, the NCO frequency must be refined before the PLL control law can be closed. This refinement is implemented by means of a 128-point FFT [2] of the filtered, downsampled signal, followed by a quadratic interpolation to identify the residual carrier offset. Once the carrier is refined, the phase-offset is sensed with a Costas Discriminator. The AGC is used to achieve unity magnitude for the signal entering the discriminator. Details of the AGC have been left off the diagram for clarity. The gain of the AGC is initially established by averaging over several filtered in-phase $\{I_{f_k}\}$ and quadrature $\{Q_{f_k}\}$ samples:

$$gain_k = \frac{N}{\sum_{j=0}^{N-1} I_{f_{k-j}}^2 + Q_{f_{k-j}}^2} \tag{7.6}$$

Thereafter, the gain is adjusted according to the magnitude of the AGC in-phase,

---

[2]This has a resolution of roughly 4Hz.

$\{I_{agc_k}\}$, and quadrature, $\{Q_{agc_k}\}$, outputs. These measurements are filtered to a bandwidth of roughly $7Hz$ by a logarithmic filter:

$$gain_k = gain_{k-1}\left(1 - \left(I_{agc_k}^2 + Q_{agc_k}^2 - 1\right)0.01\right) \qquad (7.7)$$

The $30k$Hz segment of the PLL is driven by the sym-rdy interrupts, the 1kHz segment is driven by the ms-mrk interrupts. In order to avoid memory conflicts, as discussed above, the phase computation is performed only in the sym-rdy interrupt routine. The ms-mrk interrupt routine records a timestamp clk_{curr}, and the phase associated with that timestamp is found by interpolation.

Chapter 8

Calibrating System Performance

8.I Overview of current and future LEO constellations

Table 8.1 summarizes pertinent technical information for some of the primary LEO constellations under construction, or in orbit [1]. Additional high bandwidth LEO fleets, mostly operating in Ku-band, are planned for launch in the next few years but will not be explicitly discussed here.

	Globalstar	Iridium	Orbcomm	ECCO	FAISAT	LEO One
Altitude(km)	1400	780	820	2035	1000	950
Positioning	GPS	tracking	GPS	unknown	GPS	GPS
Satellites	48	66	35	45	32	48
Downlink	S band	L band	VHF,UHF	S band	VHF,UHF	VHF,UHF
Nav Signals	2	1	1	2	1	1
Multiple Access	CDMA	TDMA FDMA	TDMA FDMA	CDMA	TDMA	FDMA
Inclination (^{o})	52	86.4	45,70,108	0, 62	83, 51	50

Table 8.1: Six of the Big LEO Constellations. The number of visible satellites (Nav Signals) is computed over the CONUS for elevations above 10°

---

[1] Information presented is only that which is available in the public domain. This information is not necessarily up-to-date.

FAISAT, operated by Final Analysis Inc., is geared towards the wireless messaging and remote Internet access markets. They have established partnerships with Raytheon, General Dynamics and L-3 Communications, and are planning to begin operation in 2002. LEO One, operated by dBX Corporation, is pursuing the market of near real-time short messaging. They have established partnerships with DaimlerChrysler and Lockheed Martin, and expect to be operational by 2003. ECCO is designed for satellite telephony and is operated by Constellation Communications, with substantial investment from Orbital Sciences Corporation. The company plans to have 10 operational satellites in equatorial orbit which will begin operation in 2002. These will purportedly be joined by an additional 35 satellites for global coverage at a later date. Orbcomm, operated by Orbital Sciences Corporation and Teleglobe, is geared towards the low data rate messaging market. Their satellites have been in continuous operation since 1998. Iridium, which was pursuing the global mobile telephony market, began operation in 1999, but filed Chapter 11 and ended commercial service in August 2000. However, in October 2000, Boeing has emerged as a potential new operator of the Iridium Satellites. Globalstar is geared towards the global portable telephony and data markets. They began service in 2000. Additional LEO fleets planned for launch in the next few years include Alcatel's Skybridge, MCI's Ellipso, and Eagle River Investment's ICO and Teledesic [2]. Of these constellations, only Orbcomm and Globalstar are currently in operation.

In order for a LEO constellation to rapidly resolve cycle ambiguities with integrity for a mobile user, the following criteria should be fulfilled:

- There should always be one satellite at reasonably high elevation angle available for tracking. Ideally two or more LEO satellites should be continually available.

[2]Teledesic is very likely to be vapor-ware.

- A carrier signal should be traceable for a time period of a few minutes.

- The position of the satellites should be known to good accuracy.

- The SNR ratios should be sufficient for accurate carrier phase estimation.

All of these criteria are fulfilled by the Globalstar Constellation. Carrier phase from one satellite can be tracked for several minutes at a time. In addition, the GPS sensors onboard the satellites enable position estimation to better than 20 meters rms [48].

8.II Satellite Availability
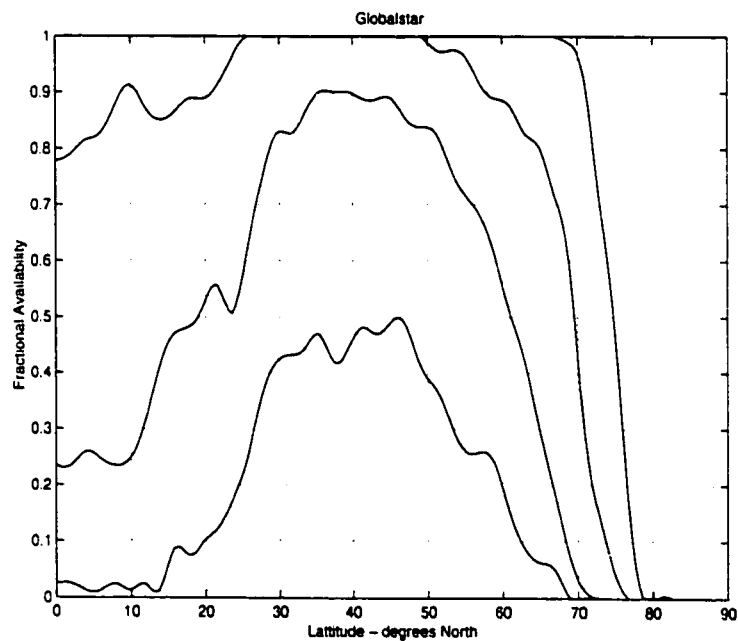
Figure 8.1: Availability study for the Globalstar satellites using Norad TLE's

105
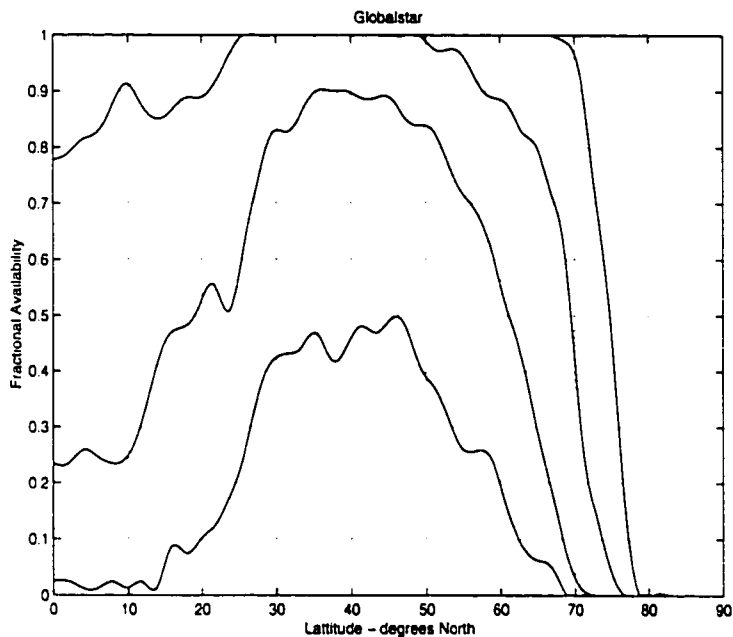
Figure 8.2: Availability study for the Orbcomm satellites using Norad TLE's

Figure 8.1 indicates the fraction of time that one, two, three and four Globalstar satellites are visible above a 10° mask angle. Note that this plot ignores the fact that a satellite may sometimes not be illuminated by a Gateway. This effect depends strongly on longitude and will have a slight impact on signal availability. Note that there are on average two satellites available above 10° elevation over the continental United States. For comparison, we have also included an availability study (Figure 8.2) for the Orbcomm satellites, which is currently the only other operational LEO Constellation - see Table 8.1. Although there are 35 Orbcomm satellites in orbit, the arrangement of this constellation is considerably suboptimal for coverage of the CONUS. The final availability analysis (Figure 8.3) is shown for the combined Orbcomm and Globalstar fleets. Notice that for this system, four LEO satellites are available, almost 100% of the time, at an elevation greater than 10°. All availability studies were conducted

106
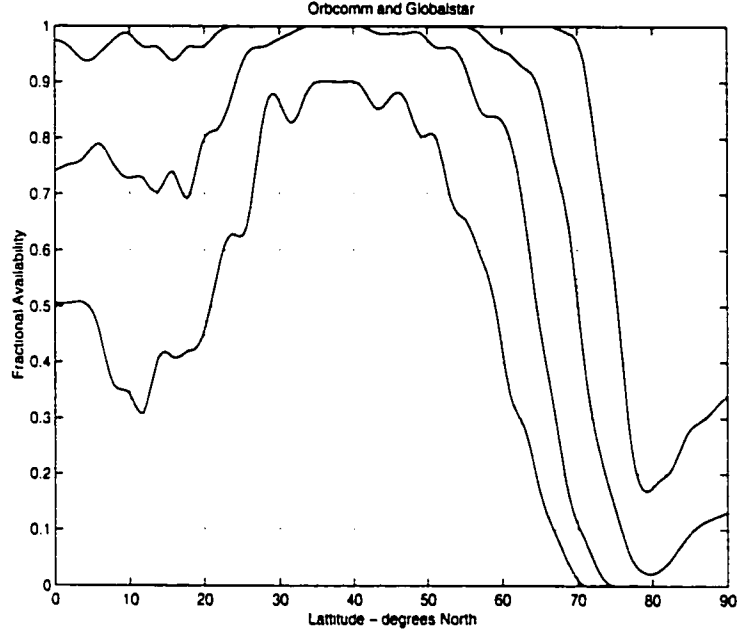
Figure 8.3: Availability study for the Globalstar and Orbcomm satellites using Norad TLE's

using Norad TLE's and projecting the satellite ephemerides for several days.

8.III Integrity with RAIM

In all availability and performance analyses, we assume that the LEOS are functional, and that no cycle slips occur over the tracking duration. For high-integrity applications, this assumption cannot be made, and position solutions would be independently validated via *receiver autonomous integrity monitoring* (RAIM) [39]. In essence, the RAIM algorithm checks if the residual of the least-squares solution at each epoch t, $\| \Delta Y(t) - H(t)\Delta\hat{\Theta}(t) \|_2$, is greater than some threshold T. T is set to meet a *continuity requirement*, i.e., not to exceed the allowed number of false alarms

of system malfunction caused by regular measurement noise. For a given acceptable error radius a, we can only guarantee that RAIM will alert us to position errors $\| \hat{r}_u(t) - r_u(t) \| > a$ using the threshold T for given satellite geometries. Figure 8.4 addresses the availability of such geometries with respect to latitude [3] to alert for radial errors of $1.1m$ while allowing a continuity risk of 2×10^{-6} per 15 *sec.* [4] We assume that GPS is augmented only with the Globalstar Constellation. A conservative phase noise variance of 1.4 *cm*, and phase sampling rate of 5 Hz are assumed.
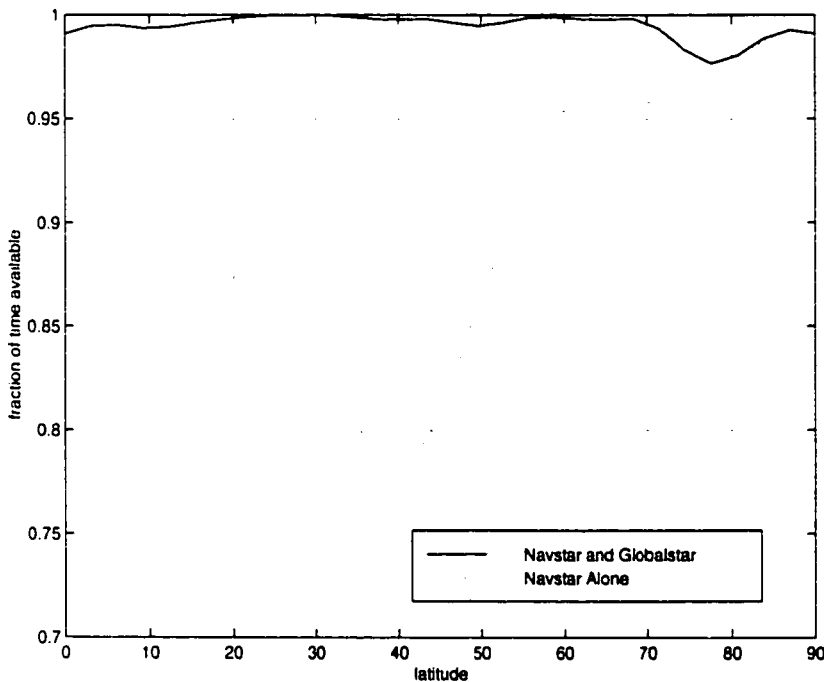
Figure 8.4: Availability of RAIM geometries for GPS alone, and GPS augmented with Globalstar

---

[3] There is a weaker dependence on longitude - these results were for $122.17°$ West.

[4] The requirements for category III automatic aircraft landing are less stringent: A 95% vertical error of 2.2 ft and a continuity risk of 2×10^{-6} per 15 *sec.* The stringent specifications were chosen to illustrate the performance improvement.

8.IV   Primary Error Sources for Precise Navigation

This section gauges those additional sources of error which cannot be directly estimated by the data reduction algorithm of Section 4.I. We provide only enough detail to roughly calibrate the sources of error.

8.IV.A   Receiver Phase-Tracking Errors

A discussion of the performance of a Globalstar receiver is in Appendix C. We will gauge the phase tracking error using Equation (C.9), since the filtering of the Globalstar inner PN sequences does not have a substantial effect on the phase tracking performance. It is prudent, for most implementations of the system, to select a narrow phase-locked loop bandwidth $B_L \approx 10$ Hz. This B_L enables a second-order phase-locked loop with damping ratio $\zeta \approx 0.7$ to track phase acceleration of $100.2\pi rad/sec^2$ with an error < 0.1rad. For a receiver noise figure of roughly 3 dB, the nominal Globalstar transmission achieves $\frac{A^2}{2N_0} = 37.5$ dB-Hz. At $B_L = 10$ Hz, we expect a $1 - \sigma$ phase error due to thermal noise of roughly 0.12 rad.

8.IV.B   Ionospheric Errors

The distance-equivalent group delay due to the ionosphere can be as large 20m at 1575MHz [38]. However, if a differential carrier-phase measurement is taken as in Equation (4.11), and the user and reference are within 10km, the resultant error is governed by local irregularities in the ionospheric structure, which delay the signal to the user and reference station by different amounts. For S-band transmissions,

and a user-reference separation of d km, we estimate the resultant phase error as a normally distributed random process of zero mean and variance $\lambda^2 4.4 \times 10^{-4} d \ rad^2$, where λ is the wavelength in centimeters. This leads to $1 - \sigma$ phase deviations on S-band signals of $0.25 \ rad$ and $0.57 \ rad$ for distances of $1km$ and $5km$ respectively. The corresponding GPS deviations are $0.44 \ rad$ and $0.99 \ rad$ respectively. Appendix H justifies these estimates in more detail.

8.IV.C Tropospheric Errors

Without any form of differential correction, the delays caused by the troposphere at a satellite elevation of 10° are roughly 14m. With differential measurement, and a baseline separation of $d < 10km$, the remaining tropospheric delay can be roughly modeled as a normal distribution $\sim N(0 \ cm, (0.1d)^2 \ cm^2)$ where d is in kilometers.

8.IV.D Ephemeris Errors

Assume we have ephemeris information for a satellite at altitude r_a that is incorrect by Δr_s. For a user and reference station separated by distance d km, the worst possible ephemeris error in calculating (4.26) is $\frac{d\Delta r_s}{r_a}$ [38, 40]. Since the Globalstar satellites have GPS position sensors, it is reasonable to assume that after collecting data for several orbits of a satellite, the ephemeris can be estimated to within 20meters rms [48]. Consequently, for the Globalstar satellites, we expect the variance of ephemeris errors discussed in Section 4.I to be bounded by 1.5cm and 7.2cm for d of 1km and 5km respectively. The ephemerides of the GPS satellites are known to within roughly 10 meters rms; the resulting ephemeris errors are bounded by 0.05cm and 0.25cm respectively. A more precise measure of the error covariance matrix discussed in

Section 4.I was found by Monte-Carlo simulation.

8.IV.E   Multipath Errors

Multipath errors arise when a signal travels over multiple paths from satellite to receiver. Signals that are reflected will be delayed relative to the direct incident signal. While the analysis of multipath for code-phase navigation can be fairly involved (Section 10.II), the analysis for the carrier-phase effect is reasonably straightforward. Namely, the combination of two coherent sinusoids will produce a new sinusoid of a different phase. Studies of the effects of carrier-phase multipath have been conducted for attitude-determination problems [18, 30, 15] and a conservative estimate for the errors on L1 (19 cm wavelength) are 0.5cm. We will also use this as a conservative bound on the errors induced at S-band (12 cm wavelength). Although multipath phase errors tend to be correlated, these errors are still below the noise floor for the simulation, where the predominant correlated errors arise from residual ephemeris errors, which are greater than multipath errors by a factor of 3 and 14 times for baselines of 1 and 5 km respectively. Of course, in severe multipath environments, the induced error can be larger than 5cm. Rather than trying to gauge the most severe effects of multipath as part of the simulation, which we assume is for an outdoor user in a benign environment, we have presented a separate section as part of the experimental work, in which we attempt to gauge the effects of multipath on carrier phase experimentally.

111

8.V Expected performance of a System Using only the Globalstar Constellation

In this section, we discuss a Monte-Carlo simulation which indicates the expected performance of a system augmenting GPS with only the Globalstar Satellites. Separate simulations are conducted for separations between user and reference station of $1km$ and $5km$. The simulations are all conducted assuming the user is in Palo Alto, California, and is capable of seeing satellites above 10° elevation[5].

8.V.A Method for Simulations with the Globalstar Constellation

With each simulation, the experimental setup was varied in the following ways:

- The user was oriented randomly with respect to the reference station, at a distance of either 1km or 5 km.

- Normally distributed, zero-mean random variables were added to the orbital elements of each satellite, consistent with the predicted accuracy of the ephemeris knowledge discussed in Section 8.IV.

- Clock variations for the user and reference receivers were modeled as sequences $\tau_k = b + (h * u)_k$ where the bias b is a uniformly distributed random variable between $-10\mu S$ and $10\mu S$, u is a sampled random process $\sim N(0,1)$, and h is a first-order lowpass Butterworth filter with a cutoff at 10^{-10} Hz and a gain of $1\mu S$.

---

[5]Commensurate results can be obtained all over the CONUS, where the probability of viewing two Globalstar satellites above 10°, assuming no satellite failures, is 100% - see Figure 8.1.

- For both reference and user receivers, a pair of frequency-dependent phase lags were selected - one for the Globalstar satellites and one for Navstar. The phase lags were uniformly distributed random variables, ranging from $[0; 2\pi]$.

- Phase errors were added to the user-reference phase difference of (4.11) for each satellite. The $1 - \sigma$ variances for GPS and Globalstar were consistent with the combined effect of errors discussed in Section 8.IV. [6]

- The assumed time of each experiment was varied, sequentially sampling the interval of 12 hours, or one period of the Navstar Satellites.

- The user is ascribed velocity in a random direction. In order to gauge the performance for different baselines, it was assumed that the user's motion was relatively slow, so that the user-reference separation was roughly constant over the course of tracking.

8.V.B Results for a Mobile User

Figure 8.5 displays the $1-\sigma$ deviation of radial position errors as a function of tracking time for a mobile user. Note that the parameter estimates were found using Equation (4.51) where the integers are treated as real numbers, and no integer search techniques are employed. Each point corresponds to the mean error deviation averaged over 200 simulations.

Figure 8.6a displays the empirical probability distribution of integer errors for a baseline of 1km, assuming a tracking time of 4 minutes. We assume here that the mobile user does not round the integer estimates off, but rather uses the best least-

---

[6]Although these noise components are colored at high sample rates, no attempt was made to color them for the sample rate of 1Hz since aliasing corrupts the spectral density function.
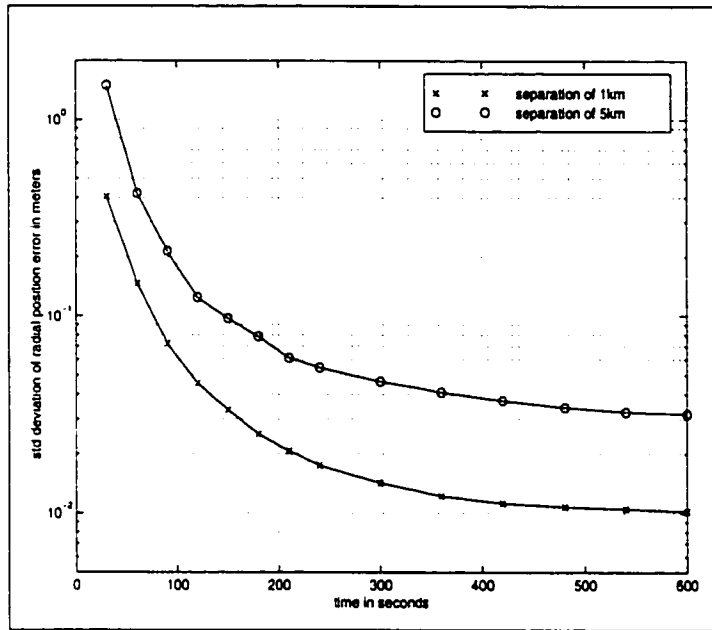
Figure 8.5: Average standard deviation in radial position errors for a mobile user, at 5km and 1km from the reference station, respectively.

square estimate at the time of position determination. Figure 8.6b displays the positioning errors for the last 10 seconds of tracking. Figures 8.7a and 8.7b display the same information for a 5 km baseline.

For scenarios where centimeter-level solutions are sought rapidly, Figure 8.7 should not be misinterpreted as an indication of the probability for selecting the correct integer. Solving the least-squares problem and then rounding generates significantly higher error probabilities than integer-search techniques. Figure 8.8 displays the evolution of the lower bound on the probability of selecting the correct set of integers for the Navstar satellites in view over the tracking period. Each point in this figure represents the worst case for 200 simulations. This lower probability bound is calculated according to the technique discussed in Section 5.III. If the ephemeris errors are the dominant error source, as is the case for this simulation, then once the integers are correctly identified, a user may rely completely on GPS measurements where
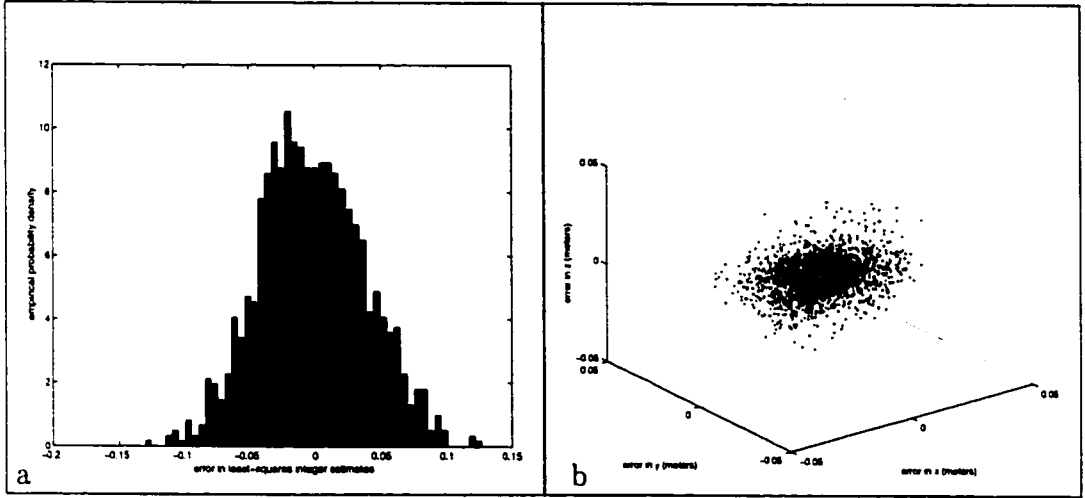
Figure 8.6: a - Estimated probability distribution of integer errors. b - 3-D plot of positioning errors for the last 10 seconds of tracking. Both plots are for baseline displacements of 1 km and a tracking time of 4 minutes.
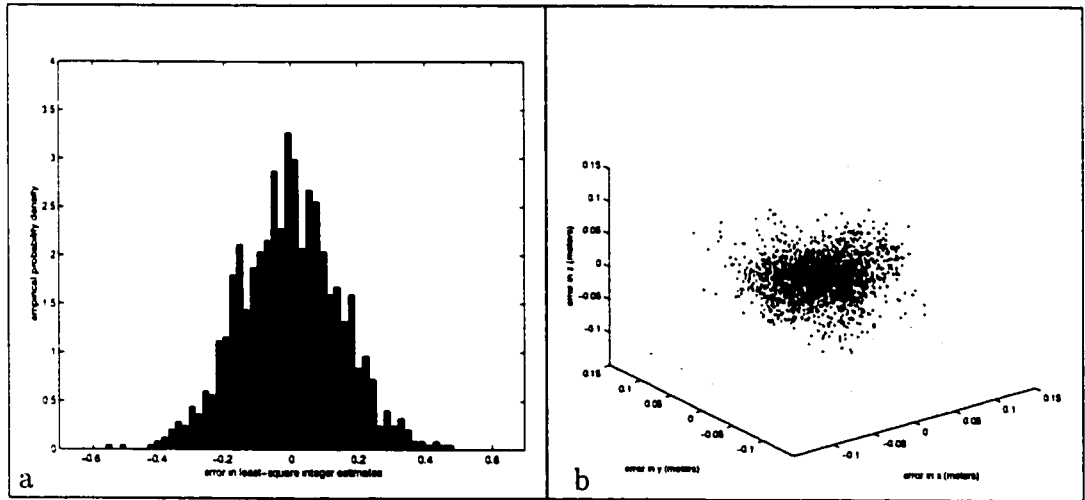
Figure 8.7: a - Estimated probability distribution of integer errors. b - 3-D plot of errors in positioning for last 10 seconds. Both plots are for baseline displacements of 5km and a tracking time of 4 minutes.

ephemeris errors are negligible. Since the measurement errors for each satellite are roughly distributed as $\sim N(0, \sigma_{ns}^2)$, the positioning error deviation for a static user decreases roughly as $\propto \frac{1}{\sqrt{N}}$ where N is the number of measurements taken on each satellite.
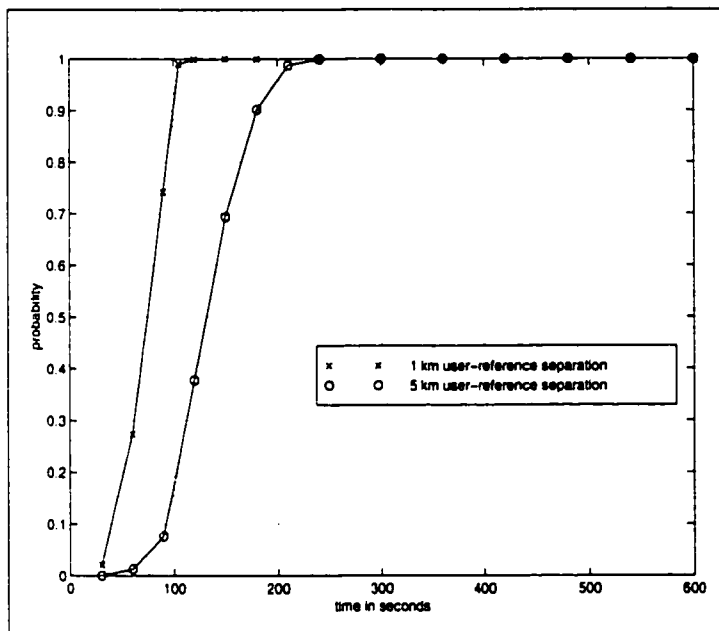
Figure 8.8: Evolution of the Probability of selecting the correct integer set for GPS augmented with Globalstar

Chapter 9

Experimental Setup and Results

9.I Antenna Setup and Calibration

Figures 9.1a and 9.1a illustrate the fabricated Orbcomm antennas used to collect experimental data for Section 9. This antenna is constructed from a three layer board. The top view (a) illustrates the quarter wave transformer striplines discussed in Section 3.I; the bottom view (b) illustrates the junction power splitter, together with a matching stub that was added to improve the the match at 400.1 MHz. The ground plane is in the center of this three-layer board.

In order to calibrate the phase errors due to motion of the antenna phase center with satellite elevation, the UHF antenna was rotated relative to a signal source and the change in phase recorded. The setup was similar to that which we describe in Section 9.IV, except that the multipath environment is benign. Figure 9.2 illustrates the measured phase, the phase correction for the mechanical swiveling of the antenna (assuming the phase center is one centimeter above the surface of the patch), and the resultant antenna phase. Notice that the corrected phase deviates over the $[0^o; 80^o]$ interval by roughly 5° or about 1cm. Since the user and reference antennas have the
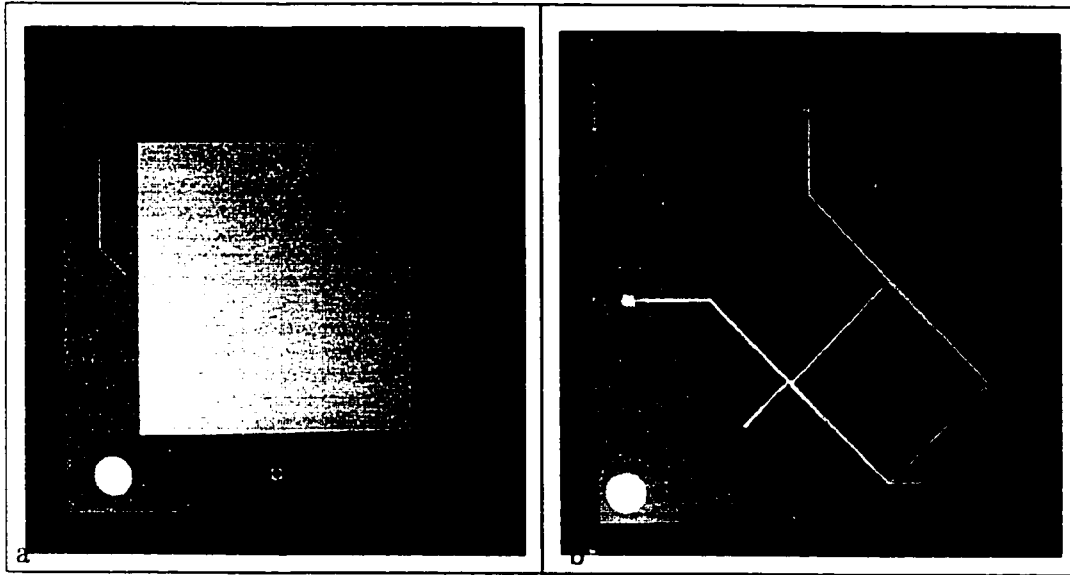
Figure 9.1: Right-hand circularly polarized antennas for the Orbcomm downlink at 400.1MHz. a) Top view - showing quarter wave impedance transformers. b) Bottom view - showing power-combining network.

same orientation for the results of Section 9.III, this phase deviation is differentially corrected.
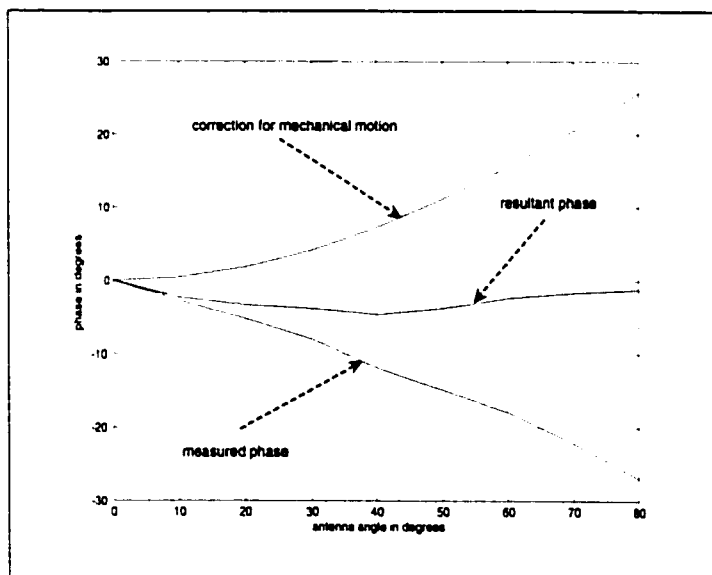
Figure 9.2: Antenna phase calibration by rotation through 80°

9.II   Overview of the Hardware Setup
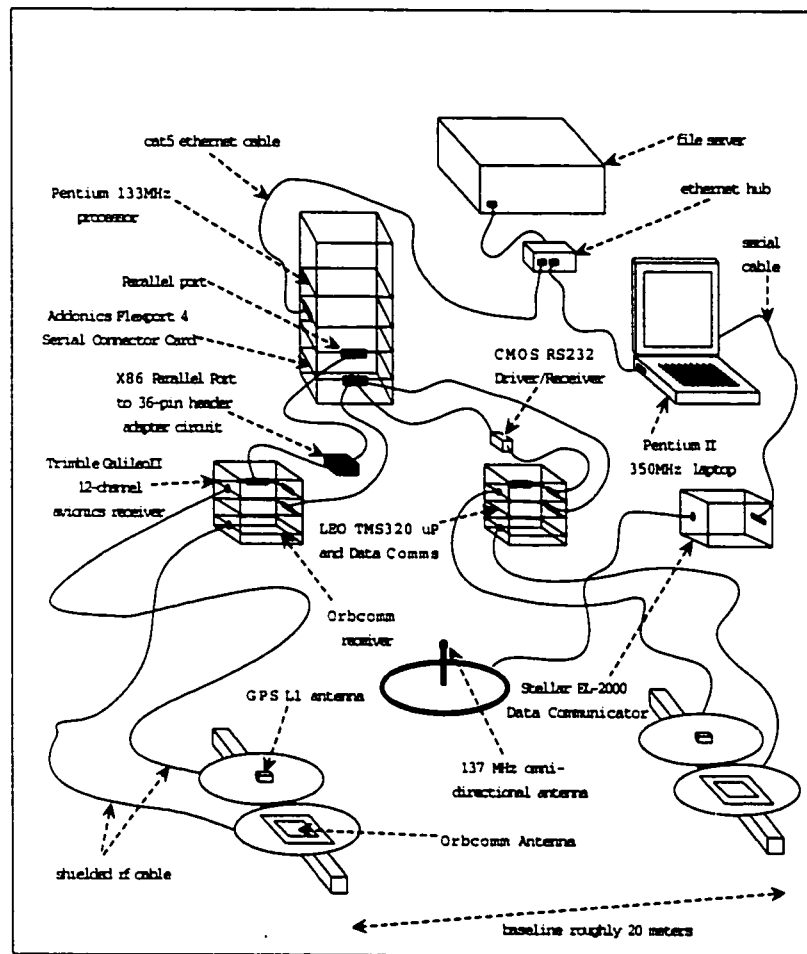
Figure 9.3: Experimental setup

Figure 9.3 provides a schematic overview of the hardware involved in this experiment. We'll track the sequence of data flow through this system. While the memory and computation for this system is distributed over multiple processors, the ultimate objective is a single processor for a user, and a single processor for the reference terminal, as described in Section 3.III.

The first step is the prediction of LEO satellite locations. Keplarian TLE's are downloaded over the Internet from the Norad Tracking Station to the Pentium II

119

350 MHz Laptop running Windows 98 O/S. Orbit prediction software (Appendix B) is run on the laptop in Matlab. This software identifies which Orbcomm satellite is at the highest elevation, and generates a fourth-order polynomial - *Doppler aiding coefficients* - modeling the expected Doppler on the satellites as a function of time. This polynomial, as well as the expected satellites acquisition time, is downloaded, via the file server, to the Pentium 133MHz desktop processor, running Linux 5.1 O/S. The Doppler aiding coefficients are uploaded, via the FlexPort 4 Serial connector card, to the TMS320 microprocessors operating the user and reference Orbcomm receiver. In addition to the Doppler aiding parameters, the Orbcomm receivers also downloads a series of parameters to administer the operation of the TMS 320 and the Sirius ASTR2001 hardware (Section 3.II.E):

- IIR filter parameters for the software PLL

- parameters administering the PLL control law

- data symbol rates for the satellite downlink

- nominal f_{if} entering A/D samplers

- digital gain for I and Q channels

- gains for the DLL and PLL control

- downshift factor to prevent overflow of the correlators

- decimation factor for the accumulators

- cdma codes/symbol matching parameters

- modulation flag, indicating whether BPSK, QPSK or modulation-free

- frequency error bound, indicating greatest possible frequency offset after acquisition before signaling a false lock

Upon the user striking a key on the desktop keyboard, the processor issues a command to both user and reference receivers to initiate acquisition and tracking of the Orbcomm satellite at the specified Doppler - see Section 7.II. Thereafter, the desktop processor will scan the three serial ports, and single parallel port respectively connected to the user LEO, reference LEO, user GPS and reference GPS receivers. The data packets received from the Trimble receivers include the following information:

- GPS millisecond time stamp

- satellite identifier for each satellite being tracked

- estimated SNR for each satellite

- flags indicating phase validity and possibility of cycle slips

- cycle slip counters

- GPS code phase, and code phase Doppler measurements

- carrier phase Doppler

- raw carrier phase measurements, and carrier phase projected to GPS-synchronized timing pulses

- satellite almanac data

- other receiver and satellite status data

The data packets are decoded and parsed by the Pentium processor to generate a file of satellite positions, a file of code-phase measurements, and a file of carrier-phase measurements adjusted to correlate with the GPS-synchronized timing pulses - see Section 7.I.D. Similarly, a data file is generated for phase measurements from the Orbcomm receiver, correlating with the GPS-synchronized timing pulses - see Section 7.II. These timing pulses are also aligned with a slower timing pulse, of rate 1Hz. Upon receiving this timing interrupt, the Orbcomm receivers will transmit a marker over the serial port, so that the phase measurements from user and reference receivers can be aligned by the Pentium processors.

While the Pentium processor administers the navigation receivers, the laptop receives data from a Stellar EL-2000 Data Communicator which tracks the 137 MHz downlink of the Orbcomm satellites. On this data link, the satellites transmit a host of telemetry information, together with the position of the satellites as reported by their on-board GPS receivers. The data packets from the EL-2000 are uploaded to the Laptop using the the *Enhanced Orbcomm Serial Interface Spec 1999*. The data packets are parsed using the *Stellar Satellite Stelcomm* software, operating on the laptop. The GPS-based satellite position data is saved to a file. Using a simple curve fitting technique, this position data is used to update the Orbcomm satellite position estimates obtained from the Norad TLEs.

The satellite position data for the GPS satellites, as well as the user and reference phase measurement files, are then accessed by the Pentium II laptop via the Ethernet. The laptop implements the data reduction algorithms discussed in Section 4.I and applies the smoothing technique discussed in Section 4.II. After completing the the smoothing routine, the algorithm of Section 5.III is used to estimate the probability with which integer ambiguities can be determined. Thereafter, the integer search

routine is implemented.

9.III Results for Tracking a Single Orbcomm Satellite in Conjunction with GPS
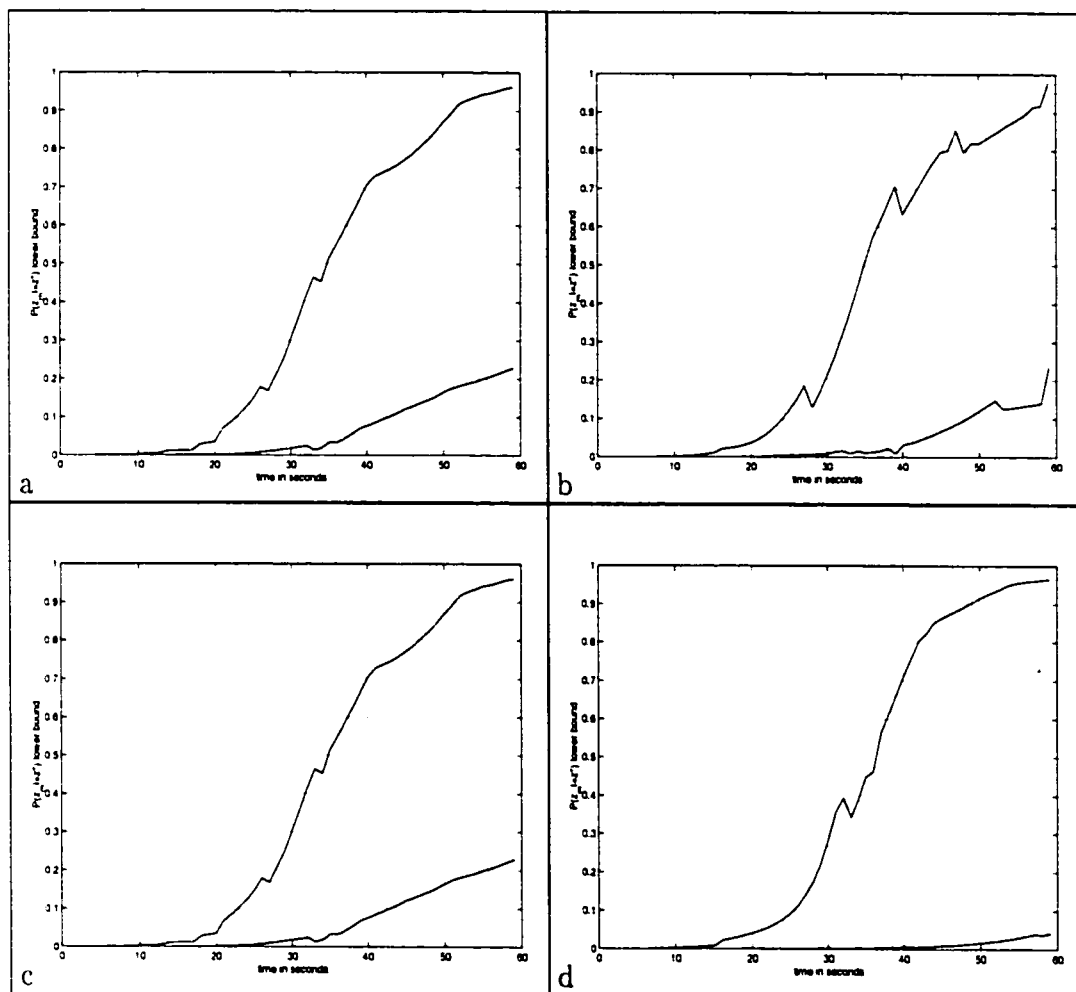
Figure 9.4: Evolution in the lower bound on the probability of selecting the correct set of integers cycle ambiguities. Probability is plotted using the GPS signals alone, as well as for the GPS signals combined with a single Orbcomm satellite signal. The performance enhancement is considerable.

Figures 9.4, 9.5, 9.6 display experimental results for four separate over-passes of single Orbcomm satellites. These passes have been labeled $a - d$. Notice that each

123
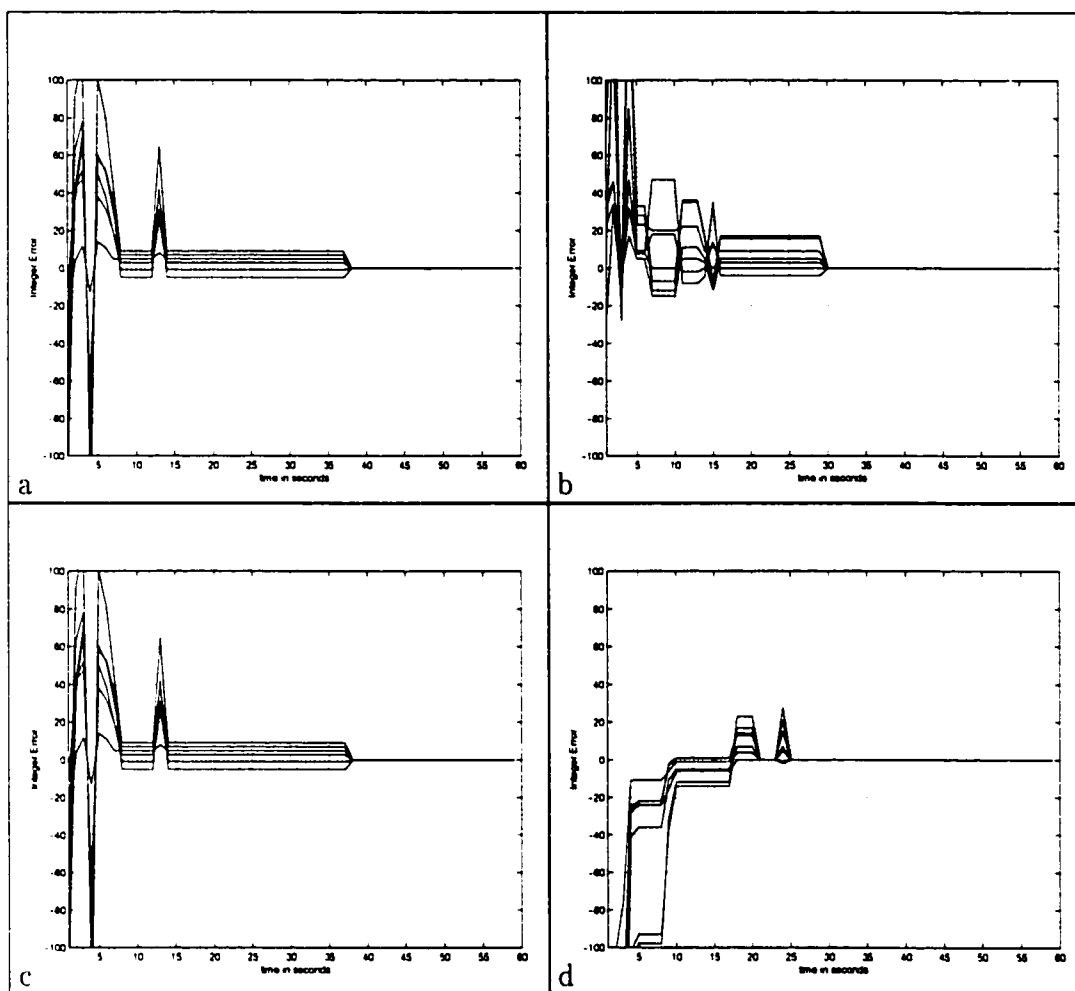
Figure 9.5: Maximum-likelihood integers estimates over 60 seconds of tracking GPS satellites together with a single Orbcomm satellite. Notice that in all cases, the cycle ambiguities are resolved well within one minute.

of the LEO passes were almost directly overhead. This type of pass is, of course, atypical. The evolution of the lower bound of selecting the correct integer illustrates the performance improvement that is achieved with the additional geometry provided by the LEO satellite. Notice that in all cases, cycle ambiguities are resolved in well under one minute, and the resulting position errors fit within a the volume of a tennis-ball.

124
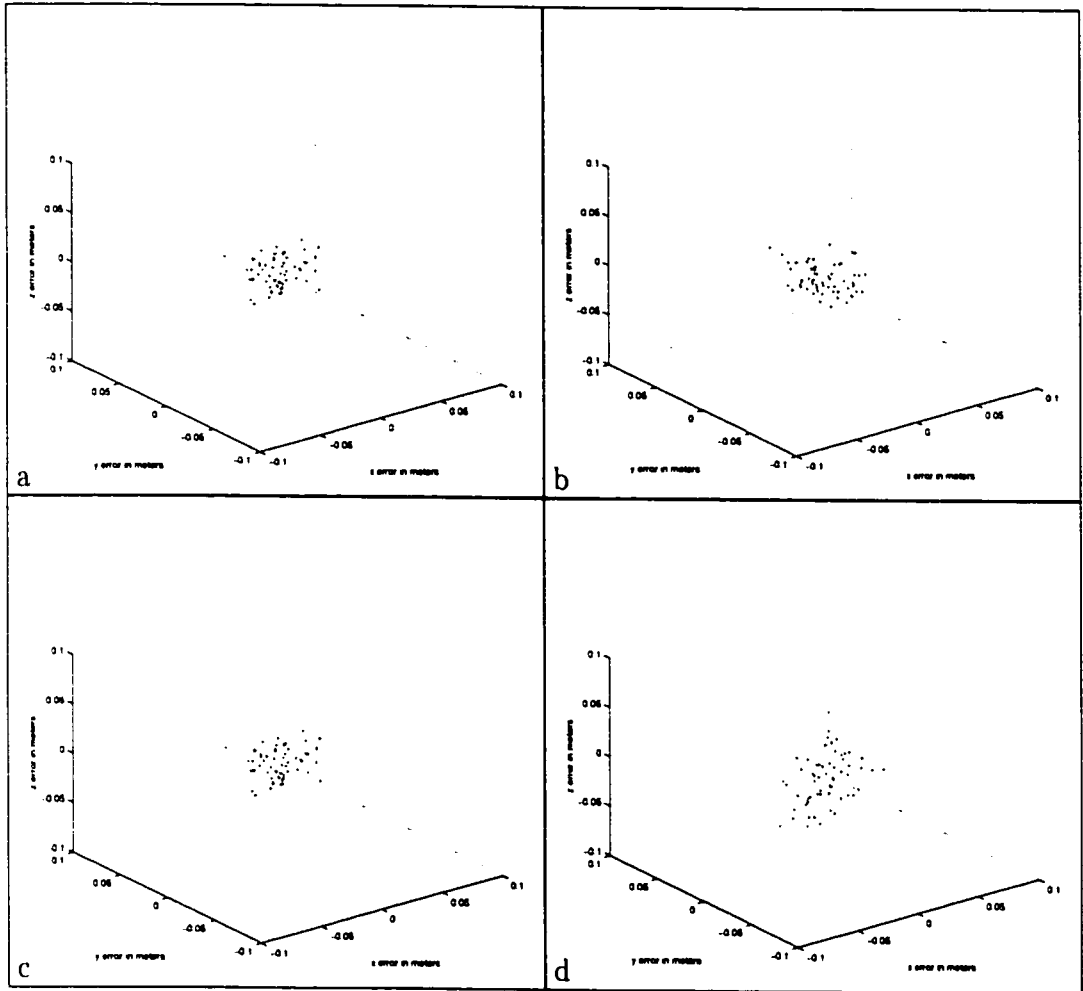
Figure 9.6: Position errors after resolving the cycle ambiguities on GPS and a parameter related to the cycle ambiguity on an Orbcomm satellite. Notice that position errors fit roughly within the size of a golf-ball.

9.IV Calibrating the Effects of Multipath on Carrier Phase Accuracy

The results described above were for stationary antennas, with large ground planes, in a benign multipath environment. In this section, as a note of caution, we will experimentally analyze the phase disturbance caused by multipath on a UHF signal. The experimental setup is illustrated in Figure 9.7. A 400 MHz tone signal is trans-

mitted out of an omni-directional antenna into the patch antenna displayed in Figure 9.1. The separation between the two antennas is maintained by a rigid wooden beam, so that the path length doesn't change as the environment alters. The patch antenna is then rotated through a series of angles from $0°$ to $80°$, and the phase of the transmission coefficient is measured on the network analyzer. The beam was moved to ten different multipath-prone environments and for each, the phase of the transmission coefficient over a range of antenna angles was determined. The results are illustrated in Figure 9.8. The mean and standard deviation for the data are also shown. The results used to calibrate the antenna (in a multipath-free environment) are also shown and have been centered at $0°$ for $0°$ of rotation. Notice that the outer errors relative to this standard are on the order of $40°$. For UHF, this corresponds to a distance-equivalent error of 8.33cm. Based thereupon, we expect, in this environment, errors on the order of 2.12cm and 1.33cm for L1 and S-band respectively.
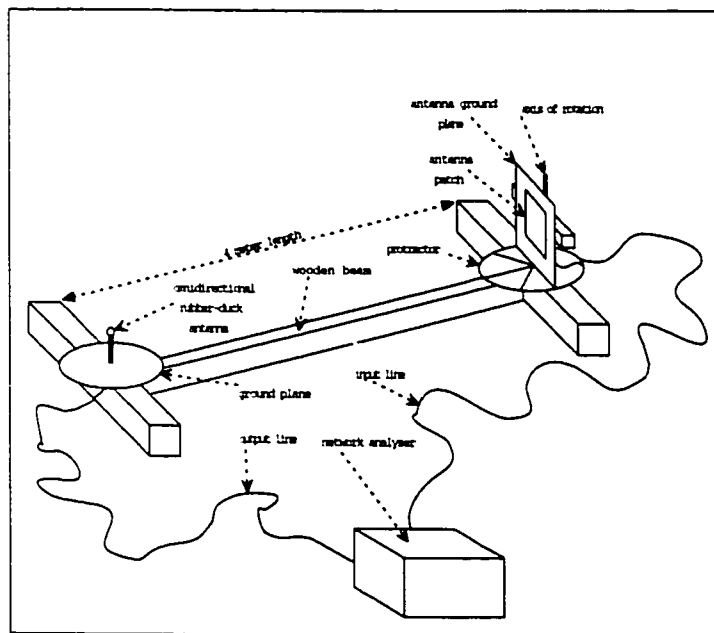
Figure 9.7: Setup for calibrating the effects of multipath on a 400 MHz UHF signal
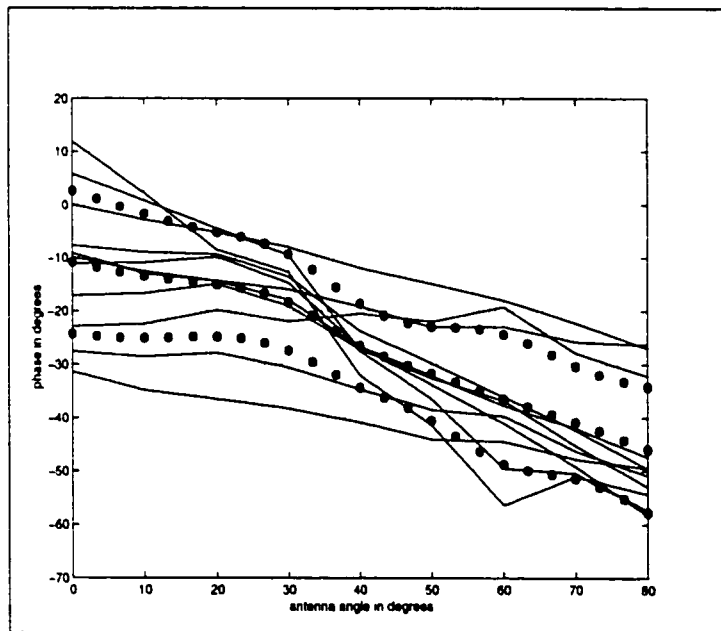
Figure 9.8: Measurement of the incident phase on the Orbcomm UHF patch antenna

Chapter 10

The Use of LEOS in Disadvantaged Environments

10.I Background

In this section we briefly explore other applications of LEOs besides those of centimeter-level carrier-phase outdoor navigation. We will focus primarily on Globalstar, which is a CDMA system, and can as such be used to enhance the performance of GPS for code-phase navigation. We describe the considerable advantages provided by these satellites in lossy environments, or multipath-prone environments. Techniques are described which use Globalstar as a stand-alone system to satisfy the FCC's E911 phase II performance requirements when GPS signals are not trackable, such as indoors.

10.I.A Characterizing the Problem

Figures 10.1 and 10.2 [54, 52, 51], taken from NASA/JPL studies, characterize the indoor effects on L-band (GPS) and S-band (Globalstar) signals. The attenuation on signals within each building is measured relative to the signal power outside, with

a direct line of site to the signal source. Figure 10.2 illustrates the dependence of attenuation on frequency. This data was taken in a farmhouse, which displayed the strongest negative trend, shown as a solid line. In general - as shown by Figure 10.1 - there is no clear trend, however there is considerable fine structure with respect to frequency[1], due to interference from multipath indoors. From fig 10.1, we see that 95% of the S-band signal energy shows less than 30dB of attenuation, in most buildings. Hence, we adopt 30dB of attenuation as our performance objective.
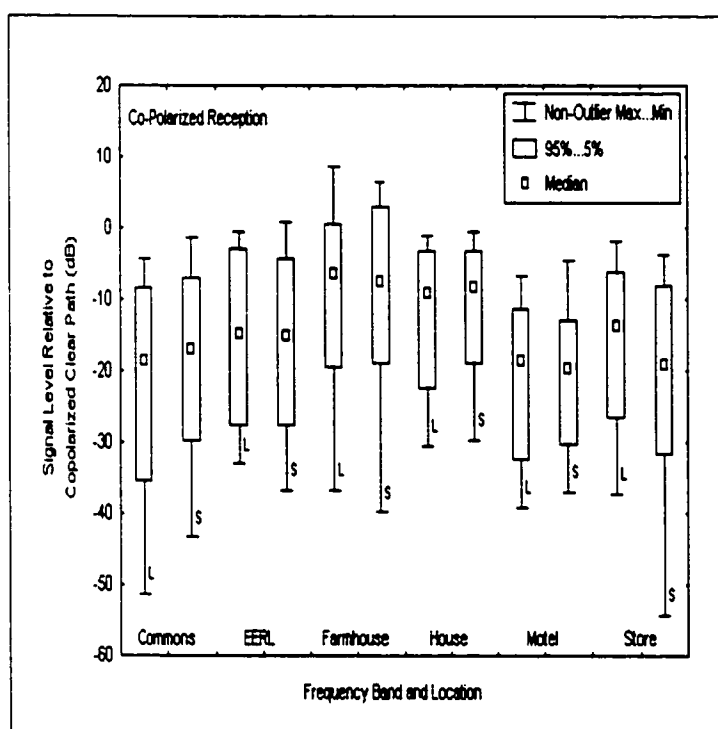
Figure 10.1: Attenuation of L-band and S-band signals in a range of indoor settings

Figure 10.3 describes the fraction of signal energy for which the delay caused by multipath is less than a certain time. Data was taken in a room, a metal shack and the foyer of a large building [53]. For example, consider the foyer of the large building.

---

[1]This fine structure will translate to considerable power variations as the antenna is shifted spatially.
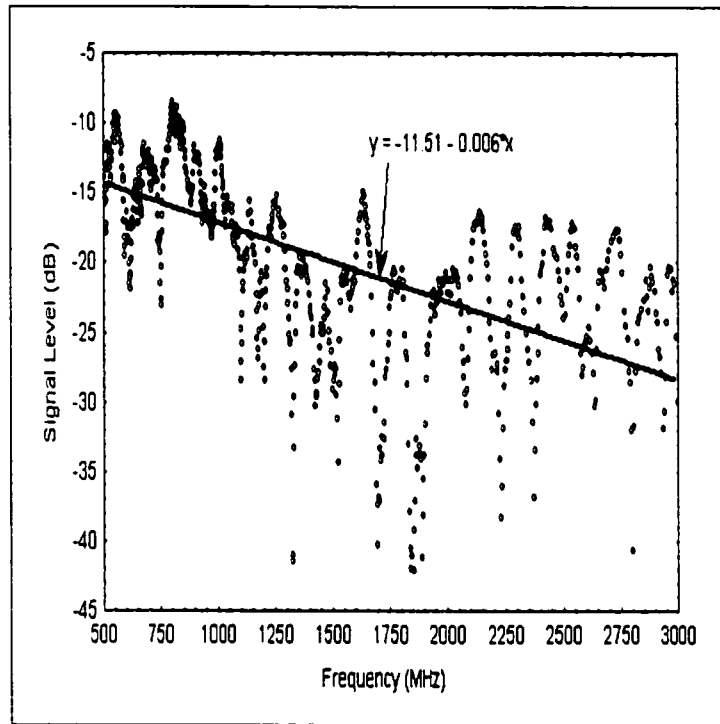
Figure 10.2: Dependence of attenuation on frequency in a farmhouse

The graph indicates that roughly 95% of the signal energy is delayed by less than 100ns.

10.I.B Integrating Attenuated Signals

The SNR of an incident signal is enhanced in inverse proportion to the bandwidth of the DLL filter, or similarly, the post-correlation integration time. There are four fundamental limitations, however, on how long a satellite signal may be integrated:

- *Data.* All techniques for integrating a signal longer than one data symbol period bear a substantial noise penalty. In the case of GPS, which has a 50Hz data rate, the best solution is to feed-forward the GPS data by some other real-time data channel so that a receiver may post-correct the GPS data bit flips. This

131
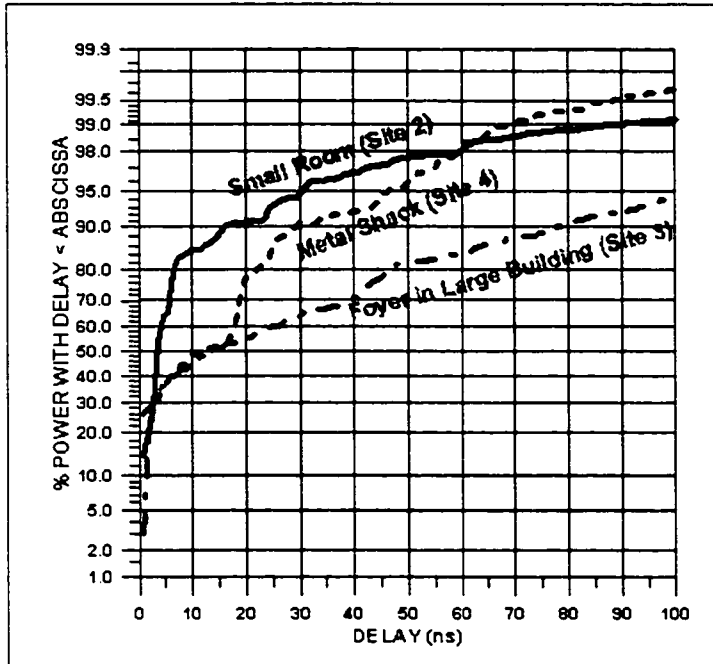
Figure 10.3: Cumulative distribution function of signal energy vs delay

can be achieved, for example, by installing a network of servers at cellular base stations to transmit the additional information [36]. In the case of LEOS this problem can be entirely circumvented, since there are signals which are either of known modulation, or are unmodulated.

- *Oscillator Stability.* Whatever the receiver implementation, the PLL control cannot be updated for the duration that a signal is being integrated. Hence, it is necessary that the local oscillator not drift out of phase by more than π during the integration period. This short-term stability of an oscillator is governed by Allan Variance [13] - see Figure 6.3. A quartz oscillator has an Allan Variance of better than 10^{-10} over periods of 1 second [13], which would accommodate an integration period of roughly 200 msec at S-band.

- *Ephemeris.* A receiver must predict carrier Doppler rate in order to maintain

132

lock on a severely attenuated satellite signal. Although a tracking loop may employ a carrier-refinement algorithm [33] to identity a Doppler *offset*, the Doppler *rate* estimate cannot be updated over the period of integration. If we don't know exactly where the satellite is, we cannot correctly accommodate the change in Doppler over the course of the integration. For the Globalstar satellite altitudes, the ephemeris should be know to within 10 km for 200 msec of integration.

- *Platform Dynamics.* Of course, if the platform is accelerating, this will effect the incident signal phase. The acceleration should be less than $\frac{\lambda}{T^2}$ where T is the integration time, or roughly 3m/sec^2 for S-band at 200msec integration time.

It is straightforward to show that an integration period of 200ms applied to the Globalstar signal can achieve a signal-to-noise ratio greater than 10dB, for signals suffering up to 30dB of attenuation.

10.II   Multipath Mitigation using Bandwidth

10.II.A   The Effect of Bandwidth

We perform a conservative analysis to calibrate the effects of multipath on navigation error. given the bandwidth of a signal. We begin by considering the effects of multipath for the C/A code GPS signal. Based on the data of Figure 10.3, a conservative model assumes the multipath signal has 10dB less power than the direct signal, and is delayed by 100nsec. The effect of this signal is illustrated in Figure 10.4.
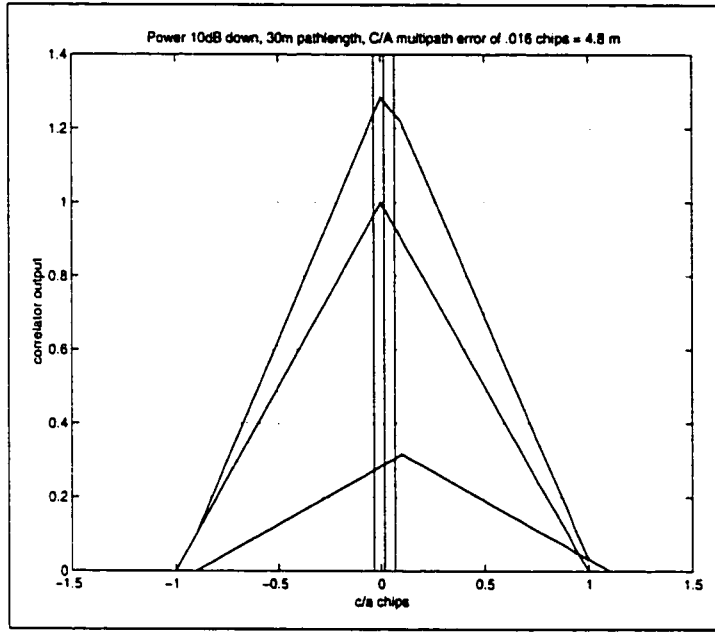
Figure 10.4: Effect of multipath on C/A code correlator, for infinite pre-correlation bandwidth, multipath power down 10dB and delay of 100nsec

The figure describes the output of a correlator which combines the incident GPS C/A code with a locally generated spreading sequence. The pre-correlation bandwidth is assumed to be infinite. The correlator output for a signal without multi-path is symmetrical around 0. The correlator output for the multipath signal is also shown. When the correlator locks onto the combined signal, using an early-late correlator spacing of .1 chips [49, 3] the induced error is .016 chips, or 4.8 meters. Now, consider a wide bandwidth signal of the form

$$
\begin{aligned}
y(t) = & D_{i1}(t)C_{i1}(t)\cos\left((\omega + \omega_0)t + \phi_0(t)\right) \\
& + D_{q1}(t)C_{q1}(t)\sin\left((\omega + \omega_0)t + \phi_0(t)\right) \\
& + D_{i2}(t)C_{i2}(t)\cos\left((\omega - \omega_0)t + \phi_0(t)\right) \\
& + D_{q2}(t)C_{q2}(t)\sin\left((\omega - \omega_0)t + \phi_0(t)\right)
\end{aligned}
\tag{10.1}
$$

This signal is similar to the proposed *Split Spectrum* for modernizing GPS [22, 23,

134
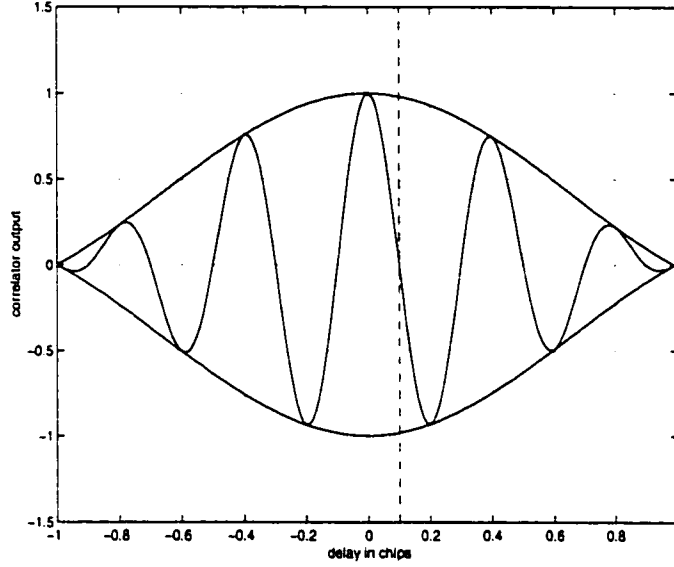
Figure 10.5: Autocorrelation function for the baseband signal derived from y(t), assuming that $\omega_0 = \frac{2.5}{T}$.

2], but it is generalized in that different spreading codes are used for both I and Q, as well as upper and lower sidebands. We assume that upper and lower sidebands arrive at the receiver with similar phase shifts, $\phi_0(t)$. This will restrict ω_0 so as to limit differential ionospheric delay on the upper and lower sidebands. Assume that all codes have a chipping rate, T, a normalized auto-correlation function, $R(\tau)$, and that the cross-correlation energy for different codes is negligible. We may convert to a baseband signal by mixing with $2\cos(\omega(t) + \phi_0(t))$ and lowpass filtering. If T_i, the integration time of the correlator, is an integer multiple of $\frac{2\pi}{\omega_0}$, the autocorrelation function for the baseband signal simplifies to $R_y(\tau) = R(\tau)\cos(\omega_0\tau)$. An example of such an autocorrelation function is illustrated in Figure 10.5 where we assume that the codes $C(t)$ have been filtered to a one-sided bandwidth of $1/T$ Hz and that $\omega_0 = \frac{5\pi}{T}$.

As before, we model multipath as a signal, $m(t)$, with a delay of $\delta = 100ns$.

135

Assuming $\frac{1}{T} = 1\text{MHz}$, the correlation for this delayed signal would be symmetrical around the vertical line at .1 chips, indicated in Figure 10.5. The combined correlation function for the direct signal, $y(t)$, and multipath signal, $m(t)$, would then be $R_y(\tau) + \alpha R_y(\tau - \delta)$ where $\alpha = \frac{max_t\ m(t)}{max_t\ y(t)}$. Notice we have assumed that $m(t)$ is perfectly in phase with $y(t)$. This is conservative since an out-of-phase $m(t)$ would in general cause less distortion of the correlation function. To find the multipath-induced error, assume equality of the early and late correlator outputs:

$$0 = R_y(\tau + \frac{d}{2}) + \alpha R_y(\tau + \frac{d}{2} - \delta)$$
$$-R_y(\tau - \frac{d}{2}) - \alpha R_y(\tau - \frac{d}{2} - \delta) \quad (10.2)$$

Perform a first-order expansion of this equality with respect to τ, and solve for τ, using the fact that R_y is symmetrical around 0, to obtain the pseudorange error due to $m(t)$:

$$\tau_e = \frac{\alpha R_y\left(-\frac{d}{2} - \delta\right) - \alpha R_y\left(\frac{d}{2} - \delta\right)}{R_y'\left(\frac{d}{2}\right) - R_y'\left(\frac{d}{2}\right) + \alpha R_y'\left(\frac{d}{2} - \delta\right) - \alpha R_y'\left(-\frac{d}{2} - \delta\right)} \quad (10.3)$$

If $m(t)$ is substantially delayed, the curvature of R_y at $-\delta$, $R''(-\delta)$ will be negligible. So, for $d \ll 1$, we can approximate $R'\left(\frac{d}{2} - \delta\right) = R'\left(-\frac{d}{2} - \delta\right)$. [2] For $d \ll 1$, we may expand Equation (10.3) to first order in d, to find

$$\tau_e = \frac{-\alpha R_y'(-\delta)}{R_y''(0)} \quad (10.4)$$

As expected, the numerator is proportional to the magnitude of $m(t)$, and the slope of R at the delayed time δ. From Fourier Analysis [37], it is straightforward to show

---

[2]This assertion is reasonable, given the conservatism of the analysis. Distortion of the correlation function caused by $m(t)$ will be most severe when the slope, $R'(-\delta)$ is maximal. In this case, $R''(-\delta)$ would be minimal.

that the denominator is related to the square of the signal's *Gabor Bandwidth*:

$$R''(0) = \frac{\int_{\infty}^{\infty} S_y(f) f^2 df}{\int_{\infty}^{\infty} S_y(f) df} \tag{10.5}$$

where S_y is the power spectral density of $y(t)$, and the denominator arises since R_y is normalized such that $R_y(0) = 1$. Clearly, the worst-case multipath effect is minimized by a signal with larger Gabor bandwidth. Applying Equation (10.4) to the hypothetical signal of Equation (10.1), and assuming a delay $\delta = 100 nsec = 0.1T$, we find τ_e decreases with increasing ω_0:

$$\tau_e = \frac{1}{\omega_0} \frac{\alpha R(\tau)}{1 - \frac{R''(0)}{\omega_0^2}} \tag{10.6}$$

10.II.B   Tracking Wide Bandwidth Signals

We will briefly describe techniques for tracking wide bandwidth signals, applied to the signal structure of Equation (10.1). The first approach, described in Figure 10.6 can be implemented in hardware, and is geared towards real-time positioning. The receiver is based on the idea that each of the codes $C(t)$ can be independently tracked. Precision is provided by the PLL that tracks the *splitting signal* which has frequency ω_0. The DLL tracks the slower codes $C(t)$, and is used to resolve the correct correlation peak from all those present due to the $cos(\omega_0 \tau)$ term in $R_y(\tau)$ - see Figure 10.5. Note in Figure 10.6 that at the output of the code mixers, we show only those terms which will pass through the lowpass filters. Note also, for the sake of clarity, that we have not illustrated early and late correlators which are necessary for an early-minus-late power discriminator in the DLL.

The most thorough approach for multipath mitigation is to sample an entire autocorrelation function, rather than to use only early and late samples. In the case

137
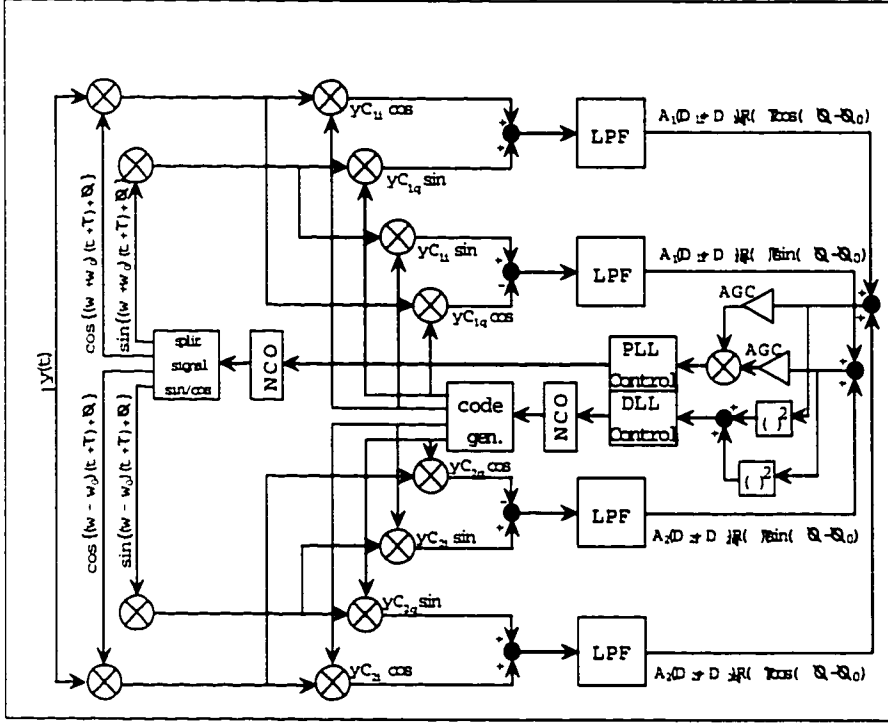
Figure 10.6: Hardware architecture to track the signal of Equation (10.1)

that position can be computed with a couple of seconds delay, such as in E911 applications, the best approach is to use a *software receiver*, which samples a sequence of the downconverted signal, and then processes this using a DSP. The following algorithm describes how the complete autocorrelation function can be generated, in a software receiver, based on samples of a signal $y(t)$. Let ω_{in} be the nominal offset of the sampled incident signal, and let ω_{offset} be the largest possible offset frequency, due to Doppler shift and oscillator frequency drift.

- $R_{max} = 0$

- Create a complex wide-bandwidth code signal

$$y_{code}(t) = (C_{i1}(t) + C_{i2}(t)) \cos(\omega_0 t) +$$

$$(C_{q1}(t) - C_{q2}(t)) \sin(\omega_0 t) + j (C_{q1}(t) + C_{q2}(t)) \cos(\omega_0 t)$$

138

$$+j\left(C_{i2}(t) - C_{i1}(t)\right) sin(\omega_0 t), \quad t = [0 \ \ldots \ T_i]$$

- Compute $F(y_{code})^*$ where F is the Fourier-transform operator, and * is the conjugation operator.

- For $\omega = \omega_{in} - \omega_{offset} : \omega_{in} - \omega_{offset}$ step $\frac{2\pi}{T_i}$

  - Create complex mixing signal

    $$y_{mix}(t) = cos(\omega t) + j sin(\omega t), t = [0 \ \ldots \ T_i]$$

  - Combine the incident and mixing signals

    $$y_{comb}(t) = y(t) y_{mix}(t)$$

  - Compute $R(\tau) = F^{-1}\left(F(y_{code})^* F(y_{comb}(t))\right)$

  - If $max_\tau \mid R(\tau) \mid > R_{max}$,

    $$R_{max} \leftarrow max_\tau \mid R(\tau) \mid, R_{store}(\tau) = R(\tau)$$

- Next ω

Upon exit, $R_{store}(\tau)$ will store the correlation between $y(t)$ and the complex code, for however many code periods are represented in the integration time T_i. $R_{store}(\tau)$ may be further refined by searching over smaller steps of ω. The initial step size for ω must be less then half the Nyquist rate $\frac{2\pi}{T_i}$. Many derivatives of this theme are possible. In addition, the extension to tracking a signal with more than two multiple split signal sidebands is obvious.

10.III Hypothetical DOP and Navigation Error in Stand-alone System

At 30dB of attenuation, it is difficult to measure pseudorange from a GPS signal. This is not necessarily the case for a Globalstar signal, which can be integrated for

200msec. We will briefly consider the performance of a system, indoors, for which only the Globalstar signals are available. Multipath error dominates the noise equation. Based on the preceding analysis, and the hypothesis that wideband signals - of bandwidth roughly 10 MHz - can be used, the pseudorange error due to multipath can be modelled with a $1 - \sigma$ deviation of 0.5 meters.

Monte-Carlo simulations were conducted to estimate the Geometric Dilution of Precision for the system, as a function of tracking interval. Figure 10.7 shows HDOP and VDOP separately. The rapid reduction in the DOP is due to the rapid angular velocity of the GSTR satellites. For each tracking interval, a histogram shows the probability distribution of DOPs which results from tracking Globalstar satellites over that interval. Two pseudorange measurements are assumed for each visible satellite: one at the initiation of tracking, and one at the end of the tracking interval. For example, consider the histograms for the 10 second interval. For a wide range of satellite geometries, a pseudo-range measurement is simulated from all visible satellites at time 0 seconds, and then again at time 10 seconds. As such, each satellite generates the same information as two spatially separated satellites[3]. Since only one estimate of the receiver clock bias is made, the technique requires a stable quartz oscillator (see Figure 6.3), with Allan Variance better than 3.10^{-11} over intervals of roughly 50 seconds[4]. Based on GDOP, and an estimate of pseudoranging error discussed above, we can estimate the associated position errors. Figure 10.8 illustrates the horizontal position error histograms (left) and vertical position error histograms, as a function of tracking interval.

---

[3]We assume that the multipath errors are uncorrelated at the beginning and end of the tracking interval, and as above, we do not account for the fact the satellites may sometimes not be illuminated by a Gateway.

[4]This stability could also be obtained from a signal arising from a cellular base station in E911-type applications
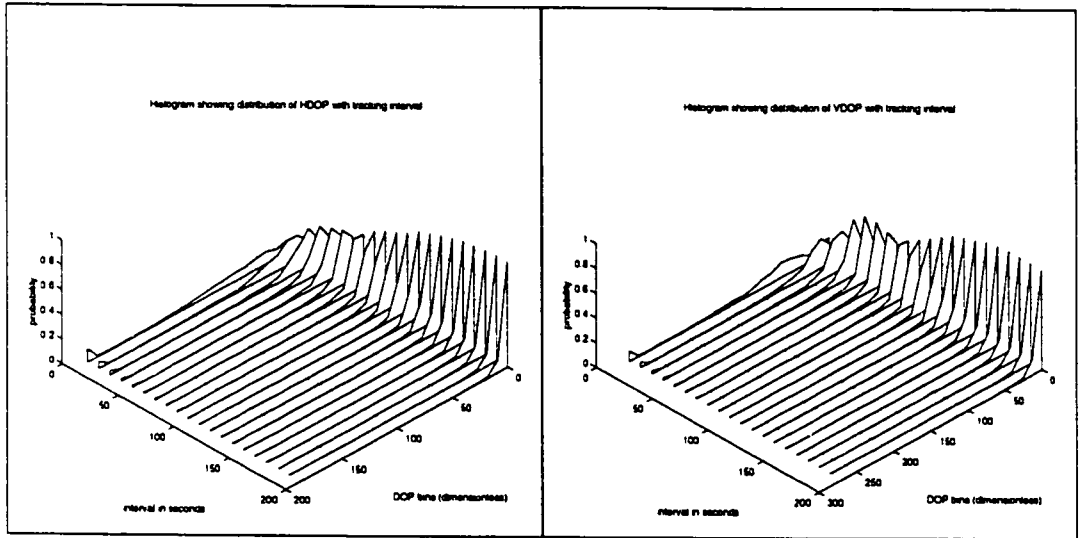
Figure 10.7: Evolution of Globalstar HDOP and VDOP with tracking interval
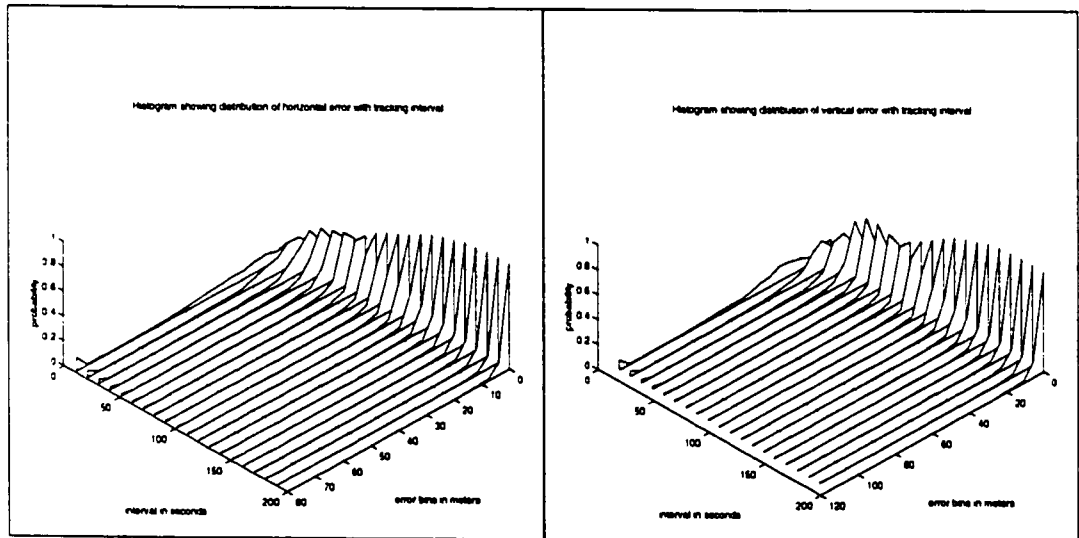
Figure 10.8: Evolution of positioning error with tracking interval, using Globalstar as a stand-alone signal

10.IV Directional Beamforming for Mobile Platforms

An effective method for enhancing the SNR as well as minimizing the effects for multipath is to employ a directional antenna. Two standard techniques for creating

a directional antenna are the use of a parabolic reflector, and the use of a phased antenna array. In the case of moving platforms, such as cars and heavy equipment for agriculture, construction and mining, a dish antenna would be impracticle both because of it's size, and it's inability to track satellites as the line of site changes. Consequently, in this section, we will focus on a beamforming technique, using a phased array antenna. The technique involves digitally combining the signal from multiple antennas so that a beam is formed in the direction of a satellite. The digital combinatorial weights are optimized so that the array antenna has maximal gain in the direction of the satellite, and minimal gain in other directions. Since beamforming may be implemented in a microprocessor, a separate beam can be implemented to track each of the available satellites. This technique can enable an order of magnitude higher data rates from satellite signals. It also facilitates robust lock on attenuated signals, and substantially limits the effects of multipath.
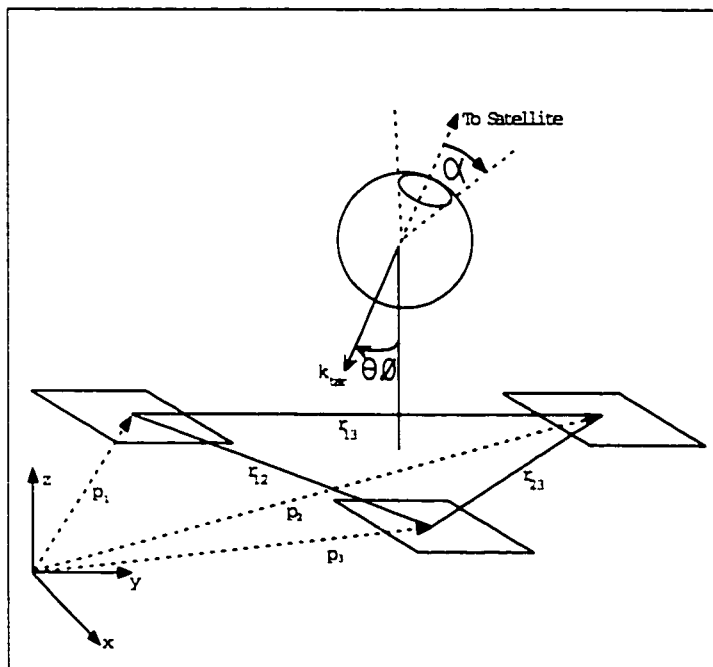
Figure 10.9: Array of antennas on the roof of an auto

142

Figure 10.9 illustrates 3 antennas, with phase centers at positions $\mathbf{p}_1$, $\mathbf{p}_2$ and $\mathbf{p}_3$ respectively. We have described how, by resolving integer cycle ambiguities on satellite signals, the baseline between a user and reference antenna can be precisely determined. Applying a similar technique to the antennas of Figure 10.9 the baselines $\mathbf{r}_{12}$, $\mathbf{r}_{23}$ and $\mathbf{r}_{13}$ can be precisely determined[5]. In addition, the location of the platform can be determined, using code-phase GPS alone, to a precision of a few tens of meters. This attitude and location information, combined with a knowledge of satellite ephemerides, can be used to determine the incident vector $\mathbf{k}$ of a satellite signal. From the coordinates established in Figure 10.9:

$$\mathbf{k} = [sin\theta cos\phi \quad sin\theta sin\phi \quad -cos\theta]^T \tag{10.7}$$

We can describe the electric field of an incident wave as $E(\mathbf{r}, t) = E e^{j(\mathbf{k}^T \mathbf{r} - \omega t)}$. Assume that this wave is incident at multiple antennas $1 \ldots N$, and each antenna output is separately filtered, downconverted and sampled in the receiver front end. Assume that the automatic gain control adjusts all inputs to unity magnitude. Consequently, the sampled signal from antenna n would be:

$$v_n(\mathbf{k}) = e^{j(\mathbf{k}^T \mathbf{p}_n - \omega t)} \tag{10.8}$$

In the microprocessor, a weighted combination of the antenna outputs is formed:

$$y(\mathbf{k}) = \sum_{n=1}^{N} w_n v_n(\mathbf{k}) \tag{10.9}$$

---

[5]The technique is simpler as applied to these antennas since both reference and user receivers are driven by the same clock and the magnitude of the baseline is known

where w_n is a complex weight for antenna n. Our task is to maximize $|\ y(\mathbf{k})\ |$ for $\mathbf{k} = \mathbf{k}_{tar}$, the direction of the satellite being tracked. In addition, we want to keep $|\ y(\mathbf{k})\ |$ as small as possible for all $\mathbf{k}$ which deviate from $\mathbf{k}_{tar}$ by more than α, as shown in Figure 10.9. α Characterizes the width of the beam we are trying to form. Let D constitute the discretized set of $\mathbf{k}$ which lie outside the beam, as shown in the figure by a ball, with a missing cone of vertex angle 2α. For economy of notation, we'll lump all the v_n, $n = 1 \ldots N$ and w_n, $n = 1 \ldots N$ into matrices:

$$\mathbf{w} = \begin{bmatrix} \Re(w_1) & j\Im(w_1) \\ \vdots & \vdots \\ \Re(w_N) & j\Im(w_N) \end{bmatrix} = \mathbf{w}_r + j\mathbf{w}_i \qquad (10.10)$$

$$\mathbf{v}(\mathbf{k}) = \begin{bmatrix} \Re(v_1(\mathbf{k})) & j\Im(v_1(\mathbf{k})) \\ \vdots & \vdots \\ \Re(v_N(\mathbf{k})) & j\Im(v_N(\mathbf{k})) \end{bmatrix} = \mathbf{v}_r + j\mathbf{v}_i \qquad (10.11)$$

The optimization objectives may now be represented as

$$y(\mathbf{k}_{tar}) = 1 \qquad (10.12)$$

$$min_{\mathbf{w}} \sum_{\mathbf{k} \in D} |\ y(\mathbf{k})\ |^2 \qquad (10.13)$$

which translate to

$$\begin{bmatrix} \mathbf{v}_r(\mathbf{k})^T & -\mathbf{v}_i(\mathbf{k})^T \\ \mathbf{v}_i(\mathbf{k})^T & \mathbf{v}_r(\mathbf{k})^T \end{bmatrix} \begin{bmatrix} \mathbf{w}_r \\ \mathbf{w}_i \end{bmatrix} = 1 \qquad (10.14)$$

$$min_{\mathbf{w}} \begin{bmatrix} \mathbf{w}_r^T & \mathbf{w}_i^T \end{bmatrix} \begin{bmatrix} \mathbf{v}_r(\mathbf{k})\mathbf{v}_r(\mathbf{k})^T + \mathbf{v}_i(\mathbf{k})\mathbf{v}_i(\mathbf{k})^T & \mathbf{v}_i(\mathbf{k})\mathbf{v}_r(\mathbf{k})^T - \mathbf{v}_r(\mathbf{k})\mathbf{v}_i(\mathbf{k})^T \\ \mathbf{v}_r(\mathbf{k})\mathbf{v}_i(\mathbf{k})^T - \mathbf{v}_i(\mathbf{k})\mathbf{v}_r(\mathbf{k})^T & \mathbf{v}_r(\mathbf{k})\mathbf{v}_r(\mathbf{k})^T + \mathbf{v}_i(\mathbf{k})\mathbf{v}_i(\mathbf{k})^T \end{bmatrix} \begin{bmatrix} \mathbf{w}_r \\ \mathbf{w}_i \end{bmatrix}$$

$$(10.15)$$

Clearly, the beamforming problem posed may be framed as a quadratic program

$$min_{\mathbf{x}} \ \mathbf{x}^T \mathbf{H} \mathbf{x}$$

$$s.t. \ \mathbf{a}^T \mathbf{x} = b$$

(10.16)

Using the method of Lagrange multipliers, it is straightforward to show that the solution to this problem is:

$$\mathbf{x} = \mathbf{H}^{-1}\mathbf{a}(\mathbf{a}^T \mathbf{H}^{-1}\mathbf{a})^{-1} b \qquad (10.17)$$

The beamforming problem may also be solved in the robust sense, where rather than minimizing the $l-2$ norm of $y(\mathbf{k})$ over all $\mathbf{k} \in D$, we minimize the maximum value of the signal: $max_{\mathbf{k}} \mid y(\mathbf{k}) \mid$, $\mathbf{k} \in D$. This can be framed as a quadratically constrained quadratic program which is straightforward to solve using constrained optimization methods.

$$min \ t$$

$$s.t. \ y(\mathbf{k}) < t, \ \mathbf{k} \in D$$

$$y(\mathbf{k}_{tar}) = 1 \qquad (10.18)$$

The calculation of weights on each antenna input, for each satellite, has to be repeated to accommodate changes in the orientation of the platform, and the position of LEO satellites. A rate of 5Hz would suffice. In order to accommodate these rates

without substantial additional computation, a lookup table could be used to generate weights for a particular bin of satellites look angles. Notice also that each of the antennas shown in Figure 10.9 could be replaced by an array of smaller antennas, or a compound patch, as shown in Figure 10.10 to which exactly the same methodology could be applied.
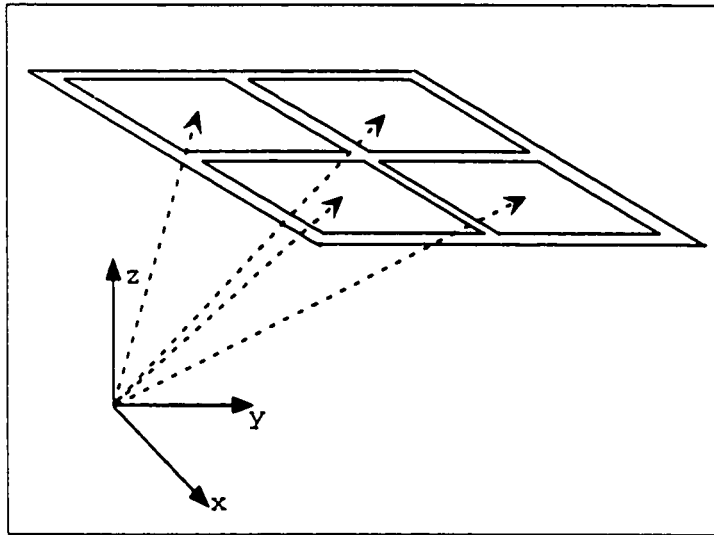
Figure 10.10: An array of small patch antennas used for higher-directivity beamforming
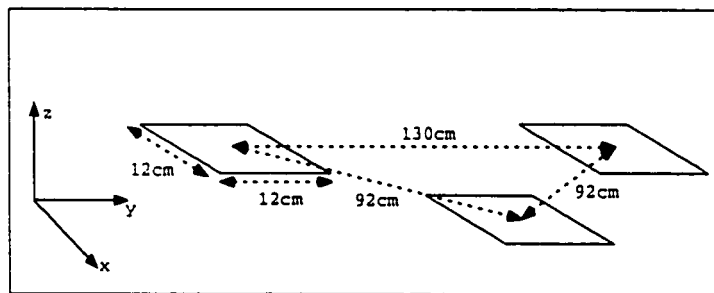
Figure 10.11: A phased array of three compound patch antennas placed on an automobile

The figures below illustrate the performance that can be achieved using various antenna setups. Figure 10.11 assumes that antennas are placed on the trunk of an automobile, with two patches close to the axis around which the trunk opens, and

146
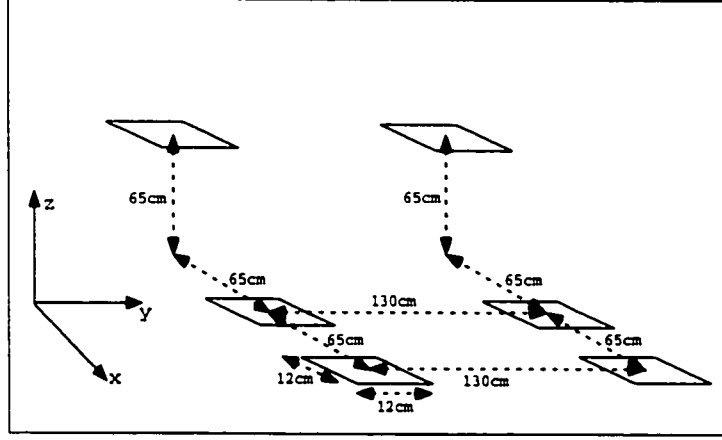
Figure 10.12: A phased array of six patch antennas places on an automobile

one at the rear. Figure 10.12 assumes that six antennas are placed on an automobile, four on the trunk and two on the roof. In both cases, each of the patches consist of four smaller antennas as shown in Figure 10.10. The optimization technique of Equation (10.17) was applied to each configuration in order to generate a vertically oriented beam of beam-width roughly 30°. The results for the configuration of Figure 10.11 are displayed in Figures 10.13 and 10.14. Figure 10.13 is a polar plot of the resultant gain of the phased-array antenna, for $\phi = 0$, and $\theta \in [0; 2\pi]$. Figure 10.14 is a plot of the antenna gain, as a function of look angles θ, ϕ for $\theta, \phi \in [0; 2\pi]$. The directional gain of this array is $12.3dB$. Figure 10.15 and 10.16 are similar plots for the configuration of Figure 10.12. The directional gain for this array is $14.8dB$.
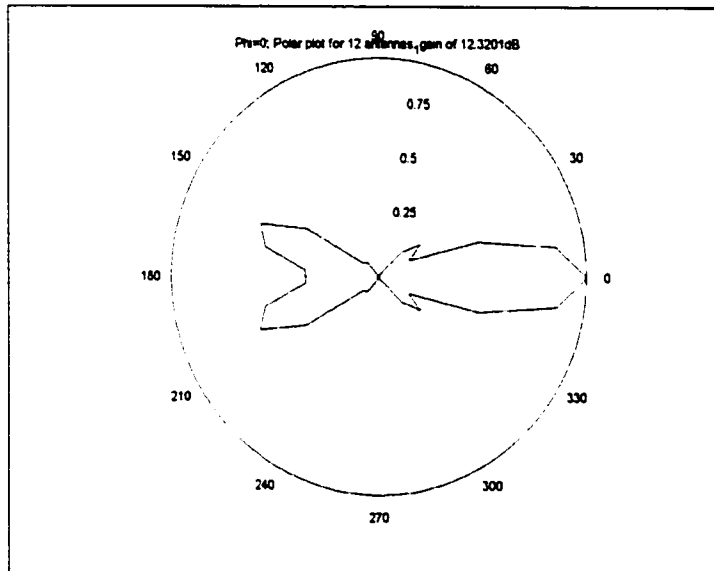
Figure 10.13: Polar gain plot for the antenna array of Figure 10.11
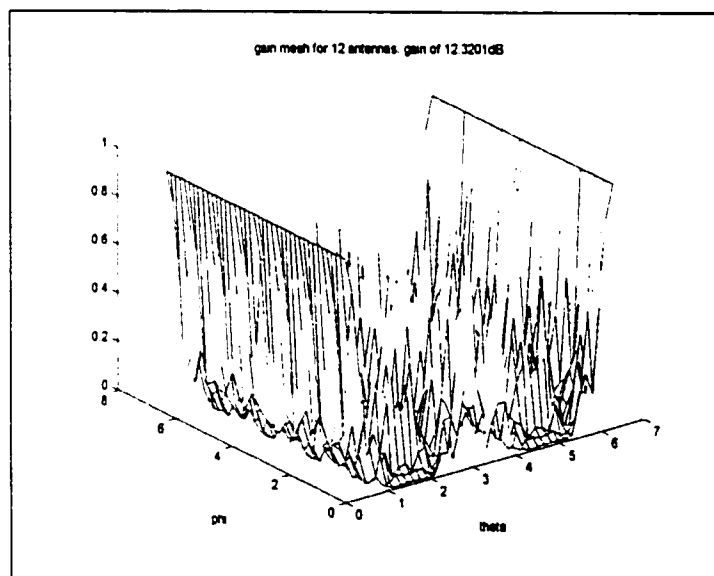
Figure 10.14: Gain as a function of look angles for the antenna array of Figure 10.11

148
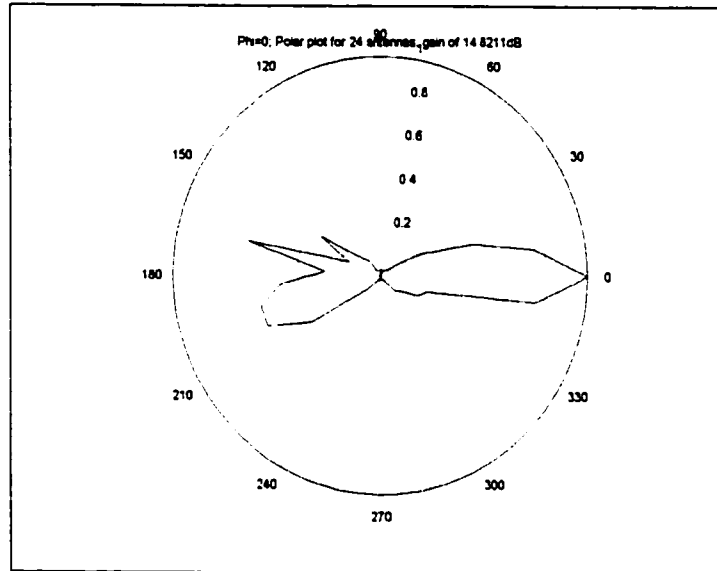
Figure 10.15: Polar gain plot for the antenna array of Figure 10.12
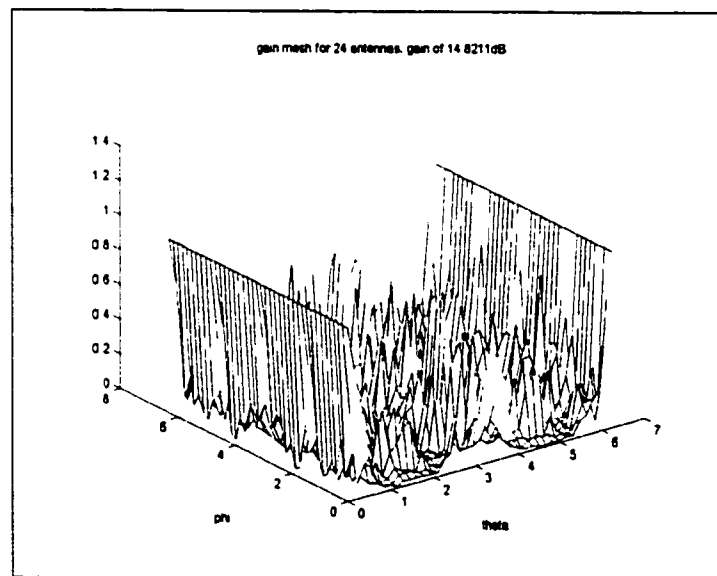
Figure 10.16: Gain as a function of look angles for the antenna array of Figure 10.12

149

Chapter 11

Summary of Contributions

This dissertation spans a wide range of issues. Consequently, we summarize here the contributions of this research. We hope that these provide a solid foundation to realizing the ultimate navigation architecture proposed in Section 2.I.

- Concept Verification: Demonstrated that rapid acquisition of centimeter-level position can be achieved using signals of LEO satellites, designed for non-navigational applications.

- Design and construction of a joint GPS-LEO navigation receiver for cm-level navigation. Components include

  - Digital hardware to synchronize GPS and LEO circuitry so that phase time-tagging errors are below the centimeter level

  - A joint GPS-LEO antenna subsystem where deterministic phase-center separation or drift can be compensated for in software

  - Design of a single pc-board LEO receiver, combining synchronization hardware with rf electronics, that can be co-located with a GPS receiver in a

151

single shielded box.

- Firmware for achieving precise integrated phase measurements using inexpensive data communication receiver hardware, by implementing an open-loop model of the hardware NCO.

- Firmware for performing precise integrated phase measurements on a scalable number of satellites, and with a scalable number of antennas, by implementing the entire signal acquisition and phase-locking operations on the microprocessor.

- Development of a data reduction technique to achieve precision navigation in a joint GPS-LEO satellite system. Techniques include

  - Accommodating frequency-dependent phase lags for each of the different constellations tracked

  - Accommodating the effects long-term oscillator instabilities on the satellite oscillators

  - Ameliorating the effects of LEO satellites ephemeris errors

  - Accommodating the effects of a bent pipe communication architecture

  - Obtaining seamless carrier-phase information using multiple beams in the satellite downlink

  - Obtaining seamless carrier-phase information for TDMA signals

- Development of navigation software for rapid acquisition of centimeter-level position. The technique assumes that frequency-dependent phase-lags are comparable for satellites of the same constellation, and that these are constant over the course of a few minutes of tracking. No assumptions about user motion, or

152

oscillator stability are made. The information smoother component generates estimates of the probability of correct integer resolution, almost in real time. The integer-search component is made efficient by a reduction of the lattice generator matrix based on the Lenstra-Lenstra-Lovatz algorithm.

- Calibration of integrated system performance by Monte-Carlo simulation. This includes

  - Estimating the navigation accuracy, and the lower bound on the probability of correct integer detection, for a joint GPS-Globalstar system.

  - Generating an error model for the joint LEO-GPS satellite system, using ionospheric phase-screen theory to gauge residual ionospheric errors after differential correction.

  - Availability studies for Orbcomm, Globalstar, and a combined GPS-Orbcomm-Globalstar system.

  - Estimating availability of RAIM geometries for a joint GPS-Globalstar system.

- Analyzed techniques by which LEOS can enhance meter-level navigation in high-attenuating, and multipath-prone environments. The techniques include

  - Minimization of multipath effects using high-bandwidth LEO signals

  - Extending integration times to accommodate signal attenuation, and using LEO geometry for position determinations independent of GPS

  - Combining platform attitude with convex optimization of weights for a phased-array antenna in order to boost antenna gain.

Appendix A

Appendix: Hardware and Signal Structure for the Transit Satellites

	Oscar 29	Oscar 27	Oscar 32	Oscar 23	Oscar 25	Oscar 31
Alt (km)	1175	1063	1274	1016	1163	1160
Freq (MHz)	399.968	399.968	399.968	399.968	399.968	399.942
Inclin (deg)	90.335	90.329	90.362	90.369	89.804	89.803

Table A.1: Basic specifications of the six operational Transit satellites

Six Transit satellites were in operation at the time of this research, and their basic specifications are listed in table A.1. Figures A.1a and A.2a illustrate the high-frequency and intermediate-frequency hardware used to track the downlink of these satellites. Rather than exploring in detail the hardware for tracking these satellites, we briefly discuss the key issues affecting the design.

A.I rf And if hardware

The low-noise amplifier and front-end filter [6] of Figure A.1a were laid out using copper-tape microstrip circuitry. The amplifier consisted of two cascoding Toshiba NTE10 transistors, with $f_T = 5GHz$, designed for low noise UHF amplifiers. The

155

noise figure for this amplifier was measured at roughly 3.6dB, which is high and largely due to the suboptimal choice of components for the biasing circuitry and the emitter circuitry for the input transistor [29]. These decisions were made in order to achieve stability, and good 50Ω matches at the amplifier input and output. The bandpass filter consists of a cascaded high-pass and low-pass filter, each designed to achieve 50Ω input/output impedance matches. The insertion loss of this filter is roughly 5dB, due to imperfections in the microstrip layout. The gain response of the circuit in figure A.1a is plotted in figure A.1b.
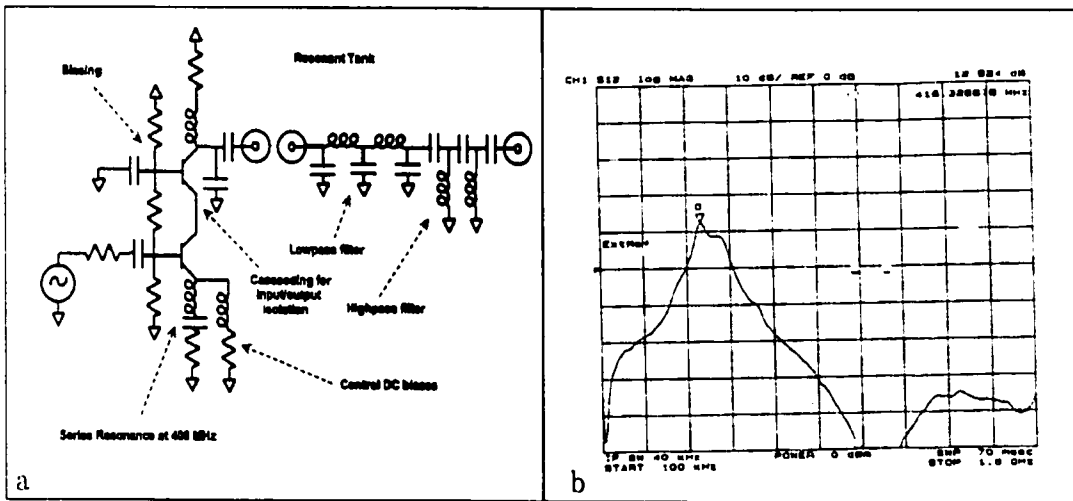
Figure A.1: Circuit design (a) and frequency response (b) of UHF amplifier and band-pass filter for Transit

Figure A.2a illustrates the design of the intermediate frequency amplifier, with gain of roughly 50dB. The op-amps employed were the AD849, with a gain- bandwidth product of roughly 400MHz. The input network is chosen in order to achieve stability, high gain, a low-frequency roll-of, and a 50Ω match at IF. The placement of the resonant tank, between the two feedback-stabilized op-amps, was found to be a robust configuration, which effectively isolated the amplifier characteristics from variations in the source and load impedances. The two resistors, respectively at the output of the

156

Figure A.2: Circuit design (a) and frequency response (b) of an intermediate-frequency amplifier, operating at 12.6MHz and providing gain of 50dB.

first op-amp and at the input of the second op-amp, with the resonant tank between them, could be adjusted to determine the *peaking* of the *if* amplifier's response, which is plotted in Figure A.2b.

A.II   Signal Structure and Tracking

Figure A.3: Symbols used to modulate phase of the Transit UHF downlink

The modulation on the UHF Transit downlink is designed such that the phase deviations above and below 0° average to 0, irrespective of the data modulation. In order to achieve this, the symbols used to modulate phase are illustrated in Figure

157

A.3. These symbols are concatenated in order to represent a data $0 = -+$ or a data $1 = +-$. The resultant signal, which has data rate $200Hz$, may be modeled as:

$$y(t) = Acos(\omega t + \phi(t) + 60^{\circ}d(t)) \tag{A.1}$$

where $d(t) \in \{-1, 0, 1\}$. The downconverted Transit signal, emerging from the receiver front end, is plotted in figure A.4. Ideally, the approach to locking onto such a signal involves a digital phase rotation which eliminates the $60^{\circ}d(t)$ modulation [44]. However, the digital hardware - see Section 3.II.E - was designed for BPSK/QPSK signals, and consequently performed in-phase and quadrature mixing, followed by a Costas phase discriminator. Given the signal structure described above, the in-phase and quadrature signals input to the Costas discriminator would be

$$i(t) = \frac{1}{2}cos(\phi(t)) - \frac{\sqrt{3}}{2}d(t)sin(\phi(t))$$
$$q(t) = \frac{1}{2}sin(\phi(t)) + \frac{\sqrt{3}}{2}d(t)cos(\phi(t)) \tag{A.2}$$

As phase-lock is established, $\phi(t) \to 0$, $i(t) \to \frac{1}{2}$ and $q(t) \to \frac{\sqrt{3}}{2}d(t)$. Despite the residual data present on $q(t)$, phase lock can still be maintained by oversampling the symbols (i.e. assuming a symbol rate higher than the actual rate) and filtering out the data using a narrow-bandwidth PLL. Figure A.5 illustrates the results of such an approach applied to the Transit signal. In this experiment, the $i(t)$ and $q(t)$ symbols were sampled at a rate of $70Hz$, and a symbol rate of $4kHz$ was assumed. Although lock is maintained on the signal, the phase disturbance resulting from the data is too high to meet the centimeter-level performance requirements. The ideal solution to this problem is to employ the software receiver described in Section 7.II to implement a matched filter for the symbols of Figure A.3 and the necessary phase rotation to accommodate $60^{\circ}d(t)$ modulation.

158

Spectrum 10 dB/ REF −4 dBm   −41.668 dBm
484.4675 kHz

RBW 30 Hz   VBW 30 Hz   ATN 6 dB   SWP 3.234 sec
CENTER 484 kHz   SPAN 2 kHz

ExtRef

.	SWP PARAM	VAL
0	484.4675 kHz	−41.668 dBm
1	484.215 kHz	−30.368 dBm
2	484.16 kHz	−43.896 dBm
3	484.2625 kHz	−44.044 dBm
4	484.365 kHz	−38.094 dBm
5	484.06 kHz	−38.311 dBm
6	483.9575 kHz	−43.237 dBm
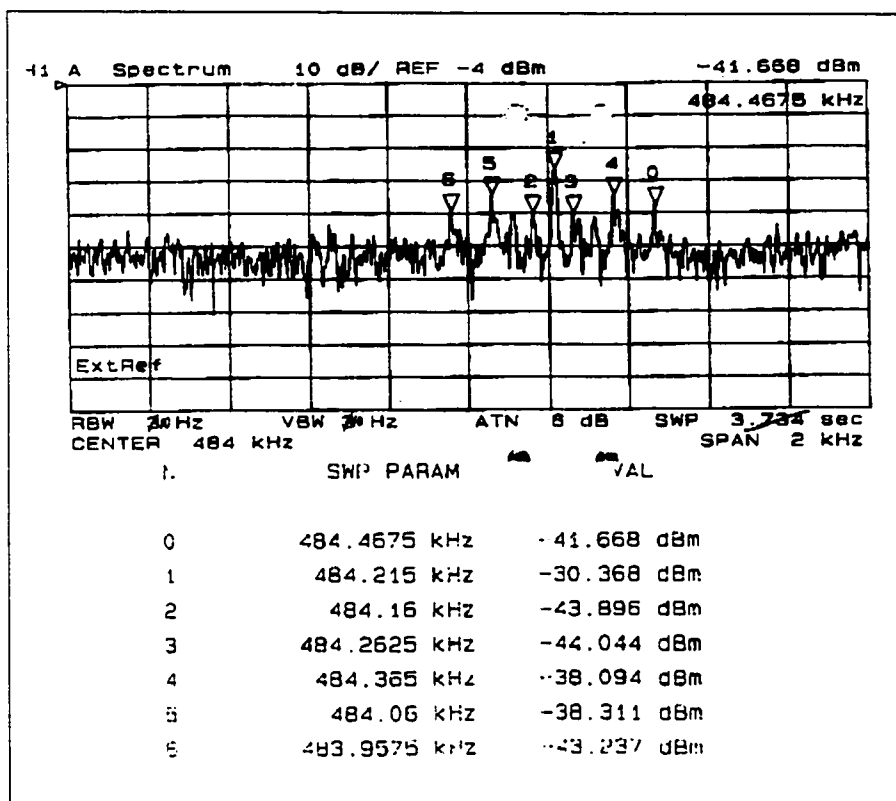
Figure A.4: Downconverted Signal of the Transit Satellites

a
b
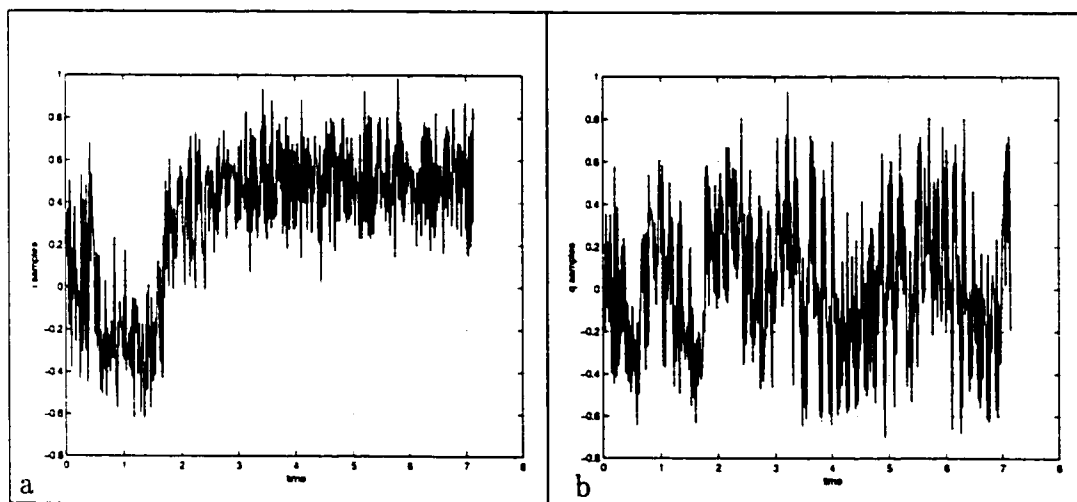
Figure A.5: In-phase (a) and Quadrature (b) symbols input to a Costas Discriminator, used to track the Transit Satellites

159

Appendix B

Positioning with Keplarian TLEs

We discuss here the prediction of satellite location using Keplarian Two Line Elements. Below is a sample TLE for an Orbcomm satellite, which was obtained from *http://celestrak.com/Norad/elements*

ORBCOMM FM 1
1 23545U 95017A 00117.13183812 .00003740 00000-0 10052-2 0 5896
2 23545 69.9753 136.0441 0011334 344.6897 15.3895 14.48757109267363

Orbit prediction software uses these parameters to predict the location of a satellite at some point in time by propagating the orbit around the Earth, using a classical gravity model. The elements which are used by the software, and their column location in each line, are described below

Line 1:

19-20 Julian year for the data epoch (last two digits of year)
21-32 Julian day for the data epoch (including fractional portion of the day)

34-43 First time-derivative of the mean motion

45-52 Second time-derivative of mean motion (decimal point assumed)

54-61 Drag term (decimal point assumed)

Line 2:

09-16 Inclination [deg]

18-25 Right ascension of the ascending node [deg]

27-33 Eccentricity (decimal point assumed)

35-42 Argument of perigee [deg]

44-51 Mean anomaly [deg]

53-63 Mean motion [Revolutions per day]

The procedure for obtaining Earth-Based-Earth-Fixed (EBEF) coordinates from Keplarian TLE's is well-detailed in [50] and will not be fully described here. We will only outline a design decision regarding the precision with which a satellite's orbit is propagated. The use of a spherically symmetric gravitational field for propagating satellite orbits will not achieve precision better than a few kilometers if the data epoch is more than a few hours old. The propagation model can be made more accurate by including higher-order spherical harmonics in the Earth's gravitational model. These higher-order terms have a more substantial effect the lower the satellite's orbital altitude. For our experiments, we used a second-order gravity model, which accounts for the oblateness of the Earth, and involves the following corrections to the ephemeris parameters computed.

$$\Delta u_{rad} = \frac{3}{2} J_2 \mu^{\frac{1}{2}} r_e^2 a^{-\frac{7}{2}} \frac{2 - \frac{5}{2} sin(i_{rad})^2}{(1-e^2)^2} \left(t_{UT,day} - t_{epoch,day} \right) \qquad (B.1)$$

$$\Delta \omega_{rad} = -\frac{3}{2} J_2 \mu^{\frac{1}{2}} r_e^2 a^{-\frac{7}{2}} \frac{cos(i_{rad})}{(1-e^2)^2} \left(t_{UT,day} - t_{epoch,day} \right) \qquad (B.2)$$

$$\Delta m_{rad} = \frac{3}{2} m_{rad} J_2 \left(\frac{r_e}{a} \right)^2 \frac{1 - \frac{3}{2} sin(i_{rad})^2}{(1-e^2)^{\frac{3}{2}}} \qquad (B.3)$$

where u_{rad} is the argument of perigee in radians, ω_{rad} is the longitude of the ascending node in radians, m_{rad} is the mean motion of the satellite in radians, a is the semi-major axis in meters, i_{rad} is the orbital inclination in radians, e is eccentricity of the orbit, $t_{UT,day}$ is the universal time in days, $t_{epoch,days}$ is the Universal Time at which the TLE's were generated, $J_2 = 1.08263 \times 10^{-3}$ is the Earth dynamic form factor. $r_e = 6.378140 \times 10^6$ m is the earth equatorial radius, and $\mu = 2.986005 \times 10^{14} \frac{m^3}{s^2}$ is the Earth's gravity constant.

Appendix C

Tracking the Globalstar Pilot Signal
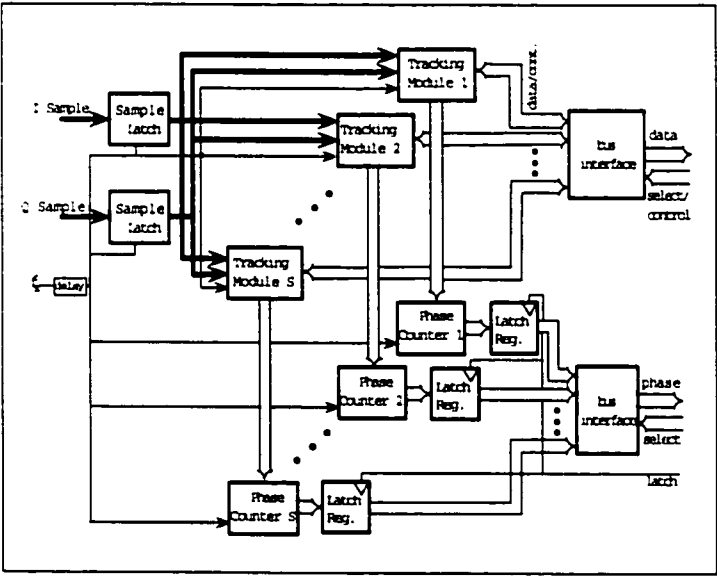
Figure C.1: Correlator assembly for the Globalstar pilot signal

The hardware designed to track the pilot signal of the Globalstar satellites has quadrature mixing at if, as described in Figure 3.3. Figure C.1 describes the architecture for a tracking assembly which is preceded by the scheme of Figure 3.3b. The thick black lines in Figure C.1 represent digitized I and Q samples. The incoming sam-

ples are latched and input to S tracking modules, where S is the maximum number of signals from a particular satellite constellation that one seeks to track. Each tracking module tracks one satellite downlink signal by means of a phase-locked loop. Many different techniques for implementing the tracking modules are known. Our system, implemented on the Sirius Astra chipset, employs a numerically controlled oscillator in the phase-locked loop. We will analyze the phase-tracking behavior with reference to the pilot signal in the Globalstar downlink, which has a modulation scheme

$$
\begin{aligned}
s(t) \;=\; & \frac{A}{\sqrt{2}} D(t) C_I(t) \cos\left(\omega t + \phi(t)\right) \\
+ \; & \frac{A}{\sqrt{2}} D(t) C_Q(t) \sin\left(\omega t + \phi(t)\right) + n(t)
\end{aligned}
\tag{C.1}
$$

where $D(t)$ refers to the outer data sequence modulated on both the in-phase and quadrature signals. $C_I(t)$ and $C_Q(t)$ are respectively the in-phase and quadrature spreading sequences. $n(t)$ Represents thermal input noise, which is assumed to be normally distributed, of zero mean and of uniform spectral density N_o. This signal is constructed according to the modulation block diagram of Figure C.2.

The tracking module designed for the signal structure of Equation (C.1) is illustrated in Figure C.3. Ignoring the effect of front-end gains equally applied to signal and noise, the in-phase and quadrature digital signal entering the tracking module can be described:

$$
\begin{aligned}
I_k \;=\; & \frac{A}{\sqrt{2}} D_k C_{Ik} \cos(\phi_k) + I_{nk} \\
Q_k \;=\; & \frac{A}{\sqrt{2}} D_k C_{Qk} \cos(\phi_k) + Q_{nk}
\end{aligned}
$$
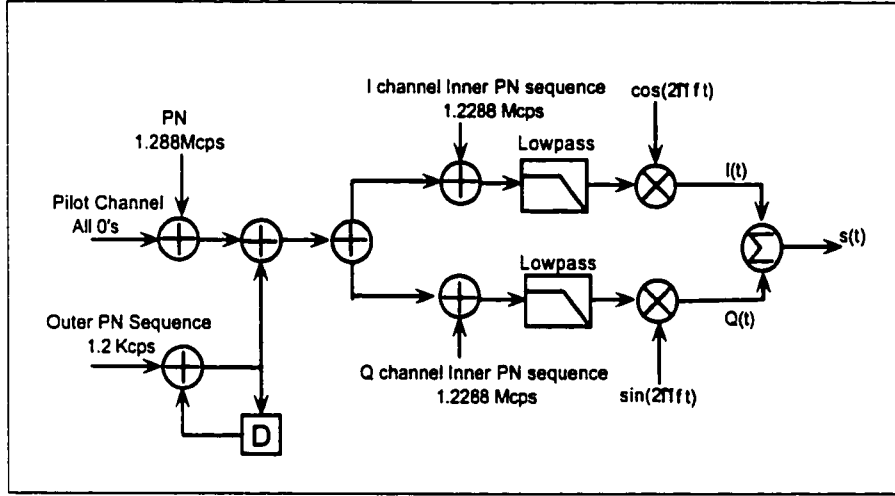
Figure C.2: Modulation scheme for the globalstar pilot signal
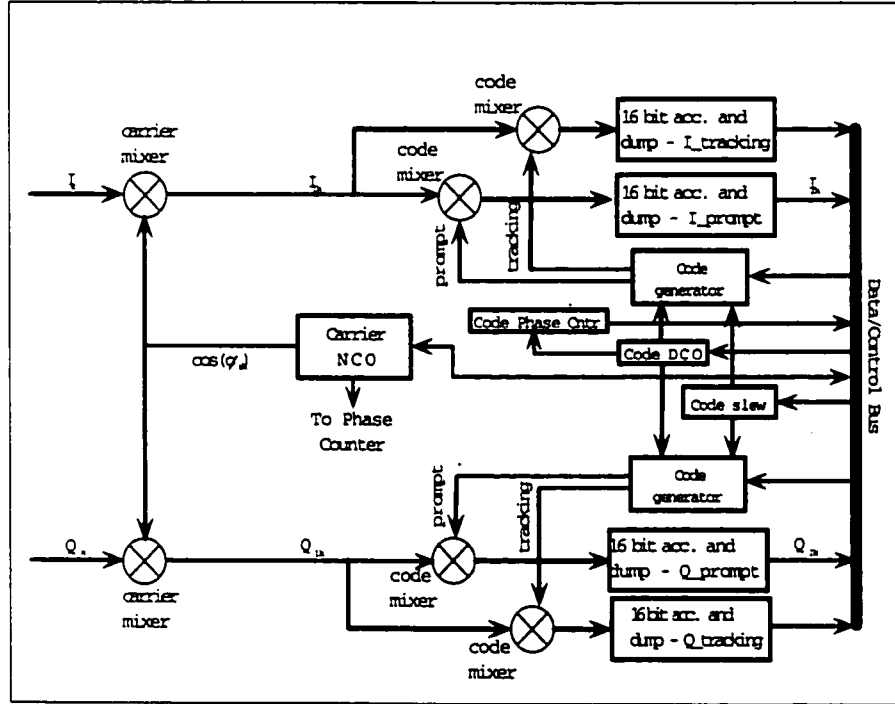
Figure C.3: Tracking module for the Globalstar pilot signal

$$E\left\{I_{nk}^2\right\} = E\left\{Q_{nk}^2\right\} = \frac{N_0 B_c}{2} \tag{C.2}$$

where B_c is the pre-correlation signal bandwidth, determined by the filters. The

167

upper sideband emerging from the carrier mixers has frequency $\sim 2f_0$ and is rejected by the accumulator which has effective bandwidth $\frac{1}{T}$, where T is the period of the inner codes $C_I(t)$ and $C_Q(t)$. Consequently, we consider only the lower sideband of the mixer outputs:

$$
\begin{aligned}
I_{1k} &= \frac{A}{\sqrt{2}}D_k C_{Ik} cos(\phi_k - \phi_{rk}) + I_{1nk} \\
Q_{1k} &= \frac{A}{\sqrt{2}}D_k C_{Qk} cos(\phi_k - \phi_{rk}) + Q_{1nk} \\
E\left\{I_{1nk}^2\right\} &= E\left\{Q_{1nk}^2\right\} \approx \frac{N_0 B_c}{2}
\end{aligned}
\tag{C.3}
$$

Each of these signals is then mixed with a prompt inner code and a tracking inner code, which consists of the difference between early and late code replicas, separated by some number of chips, d, where $d < 2$. The prompt accumulator outputs can be described:

$$
\begin{aligned}
I_{2i} &= \frac{A}{\sqrt{2}}R(\tau_i)D_i \sum_{k=1}^{M} cos(\phi_k - \phi_{rk}) + I_{2ni} \\
Q_{2i} &= \frac{A}{\sqrt{2}}R(\tau_i)D_i \sum_{k=1}^{M} sin(\phi_k - \phi_{rk}) + Q_{2ni} \\
E\left\{I_{2ni}^2\right\} &= E\left\{Q_{2ni}^2\right\} \approx \frac{M N_0}{2 T_c}
\end{aligned}
\tag{C.4}
$$

where $R(\tau_i)$ is the cross-correlation between the incoming code and the generated code for a time misalignment of τ_i. $R(\tau) \approx 1$ once code-lock is achieved. For an inner code period, T, and sample rate f_s, the summation is typically over $M = Tf_s$ samples. This number may be varied to accommodate code Doppler. Assume that over one correlation period, T, the NCO suffers a constant frequency error, $\Delta f_i \ll \frac{1}{T}$,

and a constant phase error, $\Delta\phi_i$. We can then treat the summation in Equation (C.4) as a continuous integral, and find

$$
\begin{aligned}
E\left\{I_{2i}\right\} &\approx \frac{A}{\sqrt{2}} D_i sinc\left(2\pi\Delta f_i T\right) cos(\Delta\phi_i) \\
E\left\{Q_{2i}\right\} &\approx \frac{A}{\sqrt{2}} D_i sinc\left(2\pi\Delta f_i T\right) sin(\Delta\phi_i)
\end{aligned}
\tag{C.5}
$$

For an assumed orbital altitude of 1400 km and transmissions in the S-band, we expect a maximum phase acceleration due to Doppler of $\sim 100.2\pi$ rad/s^2. For $T = 1$ ms, we expect $sinc(2\pi\Delta f_i) > 0.97$ so the factor can be safely dropped. The samples are input to the microprocessor which estimates the phase error and implements a loop filter to achieve desired phase-lock loop performance. Since the signal of Equation (C.1) has a common outer data sequence on the in-phase and quadrature components, a simple Costas Loop discriminator approximates the phase error by multiplying the samples.

$$
\begin{aligned}
\delta\phi_i &= I_{2i}Q_{2i} \\
E\left\{\delta\phi_i\right\} &= \frac{A^2 M^2}{2}\Delta\phi_i
\end{aligned}
\tag{C.6}
$$

From Equation (C.6), we see that the gain of the discriminator is $K = \frac{A^2 M^2}{2}$. In addition, the variance of the discriminator output can be computed

$$
\begin{aligned}
\sigma_{\delta\phi}^2 &= E\left\{I_{2i}^2 Q_{2i}^2\right\} - E^2\left\{I_{2i}Q_{2i}\right\} \\
&= \frac{K^2 N_0}{A^2 T}\left(1 + \frac{N_0}{A^2 T}\right)
\end{aligned}
\tag{C.7}
$$

169

By monitoring the signal amplitudes of the correlator outputs, and varying the loop control accordingly, a specific phase-lock loop transfer function, H, is maintained by the microprocessor. Generally, in selecting the bandwidth of the loop, a tradeoff must be made between rejecting thermal noise on the one hand, and tracking performance on the other. For loop transfer function H, the NCO phase error, which we cannot directly estimate by the technique described in Section (4.II), has variance

$$
\begin{aligned}
\sigma_\phi^2 &\approx \frac{S_n(0)}{K^2} \frac{1}{2\pi} \int_\infty^\infty \mid H(j\omega) \mid^2 d\omega \\
&+ \frac{1}{2\pi} \int_\infty^\infty S_o(\omega) \mid 1 - H(j\omega) \mid^2 d\omega
\end{aligned}
\tag{C.8}
$$

where $S_n(0)$ is the power spectral density near the origin of the thermal noise. The expression assumes that the loop bandwidth, $B_L \triangleq \frac{1}{2\pi} \int_0^\infty \mid H(j\omega) \mid^2 d\omega$, is much smaller than B_c. Since the correlator bandwidth, $\frac{1}{T}$, is also much less than B_c, we can safely approximate $S_n(0) = T\sigma_{\delta\phi}^2$. From Equation (C.7), the phase error variance in Equation (C.8) becomes

$$
\sigma_\phi^2 = \frac{2N_0 B_L}{A^2} \left(1 + \frac{N_0}{A^2 T} \right)
\tag{C.9}
$$

This thermal noise variance is not heavily dependent on there being the same data sequence, $\{D_i\}$, on in-phase and quadrature signal components. For example, for a CDMA signal with QPSK data modulation, we would use a fourth-power loop, rather than the Costas Loop. It has been shown by Lindsey [46] that thermal noise variance could then be approximated: $\frac{2N_0 B_L}{A^2} \left[1 + 3.8 \left(\frac{N_0}{A^2 T} \right) + 7.6 \left(\frac{N_0}{A^2 T} \right)^2 + 8 \left(\frac{N_0}{A^2 T} \right)^3 \right]$.

A phase-counter keeps track of the absolute phase of the NCO locked to each signal.

The phase measurement of the phase counter contains both a fractional and an integer component, where each integer refers to a full 2π phase cycle. There are multiple different means by which the microprocessor can read the phase of the phase counters. Whichever method is employed, for each reading epoch, the time from reading the first phase counter tracking a signal to the last phase counter tracking a signal should span an interval less than a few μsec in order to cause errors below the experimental noise floor. This specification is made concrete in Section 4.I. One method of satisfying this specification is illustrated in Figure C.1. In this configuration, a single latch signal is used to latch the phase of each of the counters in all of the phase-counting assemblies simultaneously. The latched data can then be read sequentially from each of the relevant latches. Phase reading epochs, in which the phase data for all of the signals being tracked is read, occur at frequencies roughly between 1 and 100 Hz, depending on the requirements of the specific navigation application.

Appendix D

Batch Solution via Choletsky Factorization

In order to preserve sparseness, we ignore the off-diagonal terms of the batch covariance matrix of Equation (4.48), to obtain a diagonal matrix $\bar{\mathbf{C}}$[1]. We may pre-multiply the batch measurement equation by the diagonal scaling matrix $\left(\bar{\mathbf{C}}\right)^{-\frac{1}{2}}$ and then solve the least-squares problem. Since $\left(\bar{\mathbf{C}}\right)^{-\frac{1}{2}}$ does not change the block structure of $\mathbf{H}$, we will not explicitly show the pre-multiplication by $\left(\bar{\mathbf{C}}\right)^{-\frac{1}{2}}$, or equivalently assume that $\bar{\mathbf{C}}$ is simply the identity, $\mathbf{I}_{NS}$. We may then solve the least-squares problem of Equation (4.38) by solving

$$\mathbf{H}^T \mathbf{H} \Delta \hat{\Theta} = \mathbf{H}^T \Delta \mathbf{Y} \tag{D.1}$$

The matrix $\mathbf{A} = \mathbf{H}^T \mathbf{H}$ has the block structure

---

[1]Of course, this is not ideal when ephemeris errors are the dominant error sources. However, when baselines between user and reference are only a few miles, and LEOS transmit their position based on real-time GPS position unaffected by S/A, the ephemeris errors are below the experimental noise floor.

$$
\begin{bmatrix}
\mathbf{A}_{1,1} & \mathbf{0} & \cdots & \cdots & \mathbf{A}_{1,N+1} \\
\mathbf{0} & \mathbf{A}_{2,2} & \mathbf{0} & \cdots & \mathbf{A}_{2,N+1} \\
\vdots & \mathbf{0} & \mathbf{A}_{3,3} & & \mathbf{A}_{3,N+1} \\
\vdots & \vdots & & \ddots & \vdots \\
\mathbf{A}_{N+1,1} & \mathbf{A}_{N+1,2} & \mathbf{A}_{N+1,3} & \cdots & \mathbf{A}_{N+1,N+1}
\end{bmatrix}
\tag{D.2}
$$

where the submatrices $\{\mathbf{A}_{i,i}\}$, $i < N+1$ are 4×4, $\{\mathbf{A}_{N+1,i}\}$ are $(S-1) \times 4$ and $\mathbf{A}_{N+1,N+1}$ is $(S-1) \times (S-1)$. We seek a lower triangular matrix, $\mathbf{L}$, such that $\mathbf{L}\mathbf{L}^{T} = \mathbf{A}$, with structure

$$
\mathbf{L} =
\begin{bmatrix}
\mathbf{L}_{1,1} & \mathbf{0} & \cdots & \cdots & \mathbf{0} \\
\mathbf{0} & \mathbf{L}_{2,2} & \mathbf{0} & \cdots & \mathbf{0} \\
\vdots & \mathbf{0} & \ddots & & \vdots \\
\vdots & \vdots & & \mathbf{L}_{N,N} & \vdots \\
\mathbf{L}_{N+1,1} & \mathbf{L}_{N+1,2} & \cdots & \mathbf{L}_{N+1,N} & \mathbf{L}_{N+1,N+1}
\end{bmatrix}
\tag{D.3}
$$

where the submatrices $\{L_{i,i}\}$, $i < N+1$ are 4×4 lower triangular, $\{L_{N+1,i}\}$ are $(S-1) \times 4$ and $\mathbf{L}_{N+1,N+1}$ is $(S-1) \times (S-1)$ lower triangular. This matrix can be found via Choletsky Block Factorization (see [20]), which is achieved with the following algorithm:

- for $j = 1, N+1$

-     for $i = j, N+1$

-        $\mathbf{S} = \mathbf{A}_{i,j} - \sum_{k=1}^{j-1} \mathbf{L}_{i,k} \mathbf{L}_{j,k}^{T}$

-        if $i = j$

-           compute by Choletsky factorization $\mathbf{L}_{j,j}$ s.t. $\mathbf{L}_{j,j}\mathbf{L}_{j,j}^{T} = \mathbf{S}$

-        else

174

-       solve $\mathbf{L}_{i,j}\mathbf{L}_{j,j}^{T} = \mathbf{S}$ for $\mathbf{L}_{i,j}$

-    end

-    end

- end

Once $\mathbf{L}$ is found, $\Delta\hat{\boldsymbol{\Theta}}$ can be found by block back-substitution.

Appendix E

Lower Bound on the Separation of Lattice Vertices

Consider a vertex point in the lattice generated by $\mathbf{G}$

$$\mathbf{v} = \sum_{j=1}^{k} z_j \mathbf{g}_j, \quad k \leq q \tag{E.1}$$

From the Gramm-Schmidt orthogonalization, we have that

$$\mathbf{g}_j = \sum_{i=1}^{j} \mu_{ji} \mathbf{g}_i^* \tag{E.2}$$

where

$$\mu_{ji} = \frac{\mathbf{g}_j^T \mathbf{g}_i^*}{\|\mathbf{g}_i^*\|^2} \mathbf{g}_i^* \tag{E.3}$$

The only term in the expression of Equation (E.1) involving column $\mathbf{g}_k^*$ is $z_k \mu_{kk} \mathbf{g}_k^*$. Consequently, we may recast this expression as:

$$v = \sum_{j=1}^{k} z_i^* \mathbf{g}_j^* \quad where \quad z_k^* = z_k \tag{E.4}$$

177

Therefore,

$$\|v\|^2 = \sum_{j=1}^{k} \|z_j^*\|^2 \|\mathbf{g}_i^*\| \geq \|z_k\|^2 |\mathbf{g}_i^*\|^2 \geq |\mathbf{g}_k^*\|^2 \tag{E.5}$$

However,

$$\|\mathbf{g}_k^*\|^2 \geq min(\|g_1\|^2, \|g_2\|^2 \ldots \|g_q\|^2) \tag{E.6}$$

and the proof is complete.

Appendix F

The Algorithm of Lenstra-Lenstra-Lovatz

Given a lattice $L = \mathbf{LG}$ with $\mathbf{G} = [\mathbf{g}_1 \cdots \mathbf{g}_q]$, the Lenstra-Lenstra-Lovatz algorithm obtains a reduced basis for the lattice as follows:

- Perform a Gram-Schmidt orthogonalization on the vectors $\{\mathbf{g}_i\}, i = 1 \ldots q$

  i.e. compute vectors $\{\mathbf{g}_i^*\}, i = 1 \cdots q$ recursively:

  $\mathbf{g}_j^* = \mathbf{g}_j - \sum_{i=1}^{j-1} \frac{\mathbf{g}_j^T \mathbf{g}_i^*}{\|\mathbf{g}_i^*\|^2}, \ j = 1 \ldots q$

- $\{\mathbf{g}_i^*\} i = 1 \cdots q$ will form an orthogonal basis for the space spanned by $\mathbf{G}$.

  Clearly, any vector $\mathbf{g}_j$ can be formed from a linear combination of the vectors $\{\mathbf{g}_i^*\}$

  $\mathbf{g}_j = \sum_{i=1}^{j} \mu_{ji} \mathbf{g}_i^*, \mu_{ji} = \frac{\mathbf{g}_j^T \mathbf{g}_i^*}{\|\mathbf{g}_i^*\|^2}, \ i = 1 \ldots j - 1, \mu_{jj} = 1$

- For $j = 1 \cdots q$, and given j, for $i = 1 \cdots j - 1$, replace $\mathbf{g}_j$ by $\mathbf{g}_j - \lceil \mu_{ji} \rfloor \mathbf{g}_i$

- Repeat the Gram-Schmidt orthogonalization on the new set $\{\mathbf{g}_i\}, \ i = 1 \ldots q$

- If there a subscript j violating $\|\mathbf{g}_{j+1}^* + \mu_{(j+1)j} \mathbf{g}_j^*\|^2 \geq \frac{3}{4} \|\mathbf{g}_j^*\|^2$ then

  interchange $\mathbf{g}_j$ and $\mathbf{g}_{j+1}$ and return to the first step. Otherwise, stop.

- $\mathbf{G} = [\mathbf{g}_1 \cdots \mathbf{g}_q]$ is the reduced generator matrix for the lattice L.

Appendix G

Searching for an Integral Point Inside an Ellipsoid

We describe hear an approach to searching for an integral point, $\mathbf{z}$, within the ellipsoid set $\{\mathbf{z} \in \mathbf{Z}^{q \times 1} | \|\mathbf{y} - \mathbf{Gz}\| < r\}$. Consider the case that $\mathbf{G}$ is a lower-triangular matrix,

$$
\mathbf{G} = \begin{bmatrix} g_{11} & & \mathbf{0} \\ \vdots & \ddots & \\ g_{q1} & \cdots & g_{qq} \end{bmatrix}
\tag{G.1}
$$

In this case, the inequality $\|\mathbf{y} - \mathbf{Gz}\|_2 < r$ expands to

$$
(y_1 - g_{11}z_1)^2 + (y_1 - g_{21}z_1 - g_{22}z_2)^2 + \cdots (y_q - g_{q1}z_1 - \cdots g_{qq}z_q)^2 < r^2
\tag{G.2}
$$

From the first term,

$$
\lceil \frac{y_1 - r}{g_{11}} \rceil \leq z_1 \leq \lfloor \frac{y_1 + r}{g_{11}} \rfloor
\tag{G.3}
$$

From the second term

$$(y_1 - g_{21}z_1 - g_{22}z_2)^2 < \qquad r^2 - (y_1 - g_{11}z_1)^2$$

$$\left\lceil \frac{y_1 - g_{21}z_1 - \sqrt{r^2 - (y_1 - g_{21}z_1)^2}}{g_{22}} \right\rceil \leq z_2 \leq \left\lfloor \frac{y_1 - g_{21}z_1 - \sqrt{r^2 - (y_1 - g_{21}z_1)^2}}{g_{22}} \right\rfloor \qquad \text{(G.4)}$$

So, in general, we have

$$l_i \leq z_i \leq u_i \qquad \text{(G.5)}$$

where

$$
\begin{aligned}
l_i &= t_i - r_i \\
u_i &= t_i + r_i \\
t_i &= y_i - \sum_{j=1}^{i-1} g_{ij}z_j \quad i = 1 \cdots q \\
r_1 &= 1 \\
r_{i+1}^2 &= r_i^2 - \left(y_i - \sum_{j=1}^{i} g_{ij}z_j \right)^2 \quad i = 1 \cdots q - 1
\end{aligned}
\qquad \text{(G.6)}
$$

Consequently, the search can be efficiently performed as follows:

- find the unitary matrix Γ such that ΓG is lower triangular

- make the redefinitions $\mathbf{y} \to \Gamma \mathbf{y}$, $\mathbf{G} \to \Gamma \mathbf{G}$

- for $i = 1 \cdots q$

    if $l_i > u_i$ no such integral point exists. stop.

    $z_i = \left\lceil \frac{u_i + l_i}{2} \right\rfloor$

- end.

By finding points as close to the center of the ellipsoid as possible, we are able in general to find smaller values for $\|\mathbf{y} - \mathbf{Gz}\|_2$ at each iteration. For more details, see [1].

Appendix H

Estimating the Effects of Ionospheric Irregularity
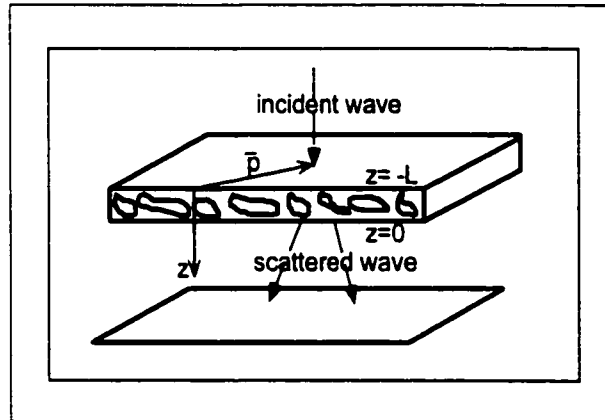
Figure H.1: Ionospheric phase-screen model

One may estimate the non-deterministic components of ionospheric error using *ionospheric phase-screen theory* [28]. This model is illustrated in Figure (H.1). Consider a signal, originating from ∞, which is incident on the ionosphere at point **p**. The emerging waveform is described by the baseband equivalent $u_0(\mathbf{p}, t) = A_0 e^{-j\phi(\mathbf{p}, t)}$. The irregularity slab is considered to act as a thin screen, which changes the phase of the emerging waveform by the amount

$$\phi(\mathbf{p}) = -\lambda r_e \int_{-L}^{0} \Delta N(\mathbf{p}, z, t) \, dz \qquad (\text{H.1})$$

where r_e is the classical electron radius, $\Delta N(\mathbf{p}, z, t)$ is the deviation in average electron content, λ is the wavelength and L is the length of the slab. The temporal phase variations caused by turbulence, or the time dependence of ΔN, have been studied in multiple Geostationary satellite beacon experiments [28]. While the effects vary considerably with time of day, and solar cycle, in all cases the PSD of phase scintillations has negligible content at high frequencies. For user and reference station clocks correlated to within $20\mu Sec$, it is evident that the temporal variation of ΔN is a negligible error source, so the t dependence can be dropped. The spatial variations, however, are crucial. In order to quantify the spatial effects, one must make an empirically guided assumption about the fractional deviations in electron content $\frac{\Delta N(\mathbf{p})}{N_0}$. It is reasonably assumed [9] that over the slab thickness L, $\frac{\Delta N(\mathbf{p},z)}{N_0}$ is a Gaussian random field of zero mean. Multiple satellite probe measurements [25], [11] have examined this issue. All suggest that, over a range of roughly 70m to 7km and assuming isotropic irregularities, the three-dimensional spatial power spectral density of $\frac{\Delta N(\mathbf{p})}{N_0}$ has a power-law dependence: $\Phi_{\frac{\Delta N}{N_0}}(\kappa) = \Phi_0 \kappa^{-\alpha}$ where α can range roughly between 2 and 4 [9, 11].

To find the effect of these irregularities on the signal $u_0(\mathbf{p})$ as it propagates downwards, the field can be computed using Kirchoff's diffraction formula [28]. Under the forward scattering assumption[1], the Fresnel diffraction results in:

$$u(\mathbf{p}, z) = \frac{jk A_0 \lambda^2}{2\pi z} \int \int e^{\left[-j\left(\phi(\mathbf{p}') + \frac{k}{2z}|\mathbf{p}-\mathbf{p}'|\right)\right]} \, d^2\mathbf{p}' \qquad (\text{H.2})$$

[1] Forward scattering assumes that the wave is scattered into a small angular cone centered around the direction of propagation.

186

where k is the scalar wave vector. Applying to this propagation law the assumption of a Gaussian distribution in phase, it can be shown [28], that for small phase fluctuations, the power spectral density of phase deviations for receivers placed at z is:

$$\Phi_{\angle u}(\kappa_\perp) = 2\pi\lambda^2 r_e^2 \cos^2\left(\frac{\kappa_\perp^2 z}{2k}\right) L\Phi_{\frac{\Delta N}{N}}(\kappa_\perp, 0) \qquad \text{(H.3)}$$

Assigning a precise formulation for $L\Phi_{\frac{\Delta N}{N}}(\kappa_\perp, 0)$ is difficult since the ionospheric irregularities vary substantially with time of day and solar activity [21]. However, to err on the side of conservatism, we match our model to data for high scintillation activity at $\kappa_\perp = 2\pi 0.2 \ rad.km^{-1}$ and assume a rolloff of $\alpha = 2$ for larger $\kappa_\perp$. The factor $\cos^2\left(\frac{\kappa_\perp^2 z}{2k}\right)$, which leads to diffraction nulls at specific altitudes, was dropped. The resultant power spectral density, for $\kappa_\perp \in [0.4\pi; \infty) rad.km^{-1}$ is

$$\Phi_{\angle u}(\kappa_\perp) \approx \frac{2.8 \times 10^{-3}\lambda^2}{\kappa_\perp^2} \ rad.km \qquad \text{(H.4)}$$

for λ in cm. If we assume, again conservatively, that all the phase variations at the position of the user and reference station are uncorrelated, then we can estimate the variance in ionospherically-induced phase differences for a user and reference station separated by horizontal distance d km.

$$E\left\{(\angle u)^2\right\} = \int_{\frac{2\pi}{d}}^{\infty} \frac{2.8 \times 10^{-3}\lambda^2}{\kappa_\perp^2} \ d\kappa_\perp \qquad \text{(H.5)}$$

187

Bibliography

[1] A.Hassibi. Integer paramter estimation in linear models with application to GPS. Technical Report ECS-9222391, Information Systems Laboratory, Stanford University, 1996.

[2] P.Fenton A.J van Dierendonck, M.Schumpert. Acquisition, tracking and mitigating multipath using the proposed split spectrum c/a-code at 12. *Proceedings of ION-GPS 98*, pages 1895–1903, 1998.

[3] T.Ford A.J van Dierendonck, P.Fenton. Theory and performance of narrow correlator spacing in a GPS receiver. *Navigation*, 39(3):265–283, 1992.

[4] C.A. Balanis. *Antenna Thoery*. John Wiley and Sons, 2nd edition, 1997.

[5] B.S.Pervan. *Navigation Integrity for Aircraft Precision Landing Using the Global Positioning System*. PhD thesis, Stanford University, 1996.

[6] J.J. Carr. *Secrets of RF circuit design*. McGraw-Hill, 1996.

[7] C.C.Counselman. *US Patent no. 5,384,574: System for Determining Position from Suppressed Carrier Radio Waves*. Western Atlas International, Inc., January 1995.

189

[8] B.S.Pervan C.E.Cohen and B.W. Parkinson. Integrity in cycle ambiguity resolution for GPS-based precision landing. *Third International Conference on Differential Satellite Navigation Systems (DSNS-94), London, UK*, 1994.

[9] C.L.Rino and J.Owen. Numerical simulations of intensity scintillation using the power law phase screen model. *Radio Science*, 19(3):891–908, May-June 1984.

[10] C. E. Cohen. *Attitude Determination Using GPS*. PhD thesis, Stanford University, 1992.

[11] D.J.Fang and C.H.Liu. Statistical characterization of equatorial scintillation in the Asian region. *Radio Science*, 19(1):345–358, 1984.

[12] D.T.Knight. *US Patent no. 5,296,861: Method and Apparatus for Maximum Likelihood Estimation Direct Integer Search for Carrier Phase Attitude Determination Systems*. Trimble Navigation Ltd., March 1994.

[13] C.C. Hodge D.W. Allan, N. Ashby. The science of timekeeping. Technical Report Application Note 1289, Hewlett Packard, 1997.

[14] C. E. Cohen et al. *US Patent no. 5,572,218: System and Method for Generating Precise Position Determinations*. IntegriNautics, Palo Alto, Calif., June 1995.

[15] C.E.Cohen et al. Real-time cycle ambiguity resolution using a pseudolyte for precision landing of aircraft with GPS. *Second International Conference on Differential Satellite Navigation Systems (DSNS-93)*, March-April 1993.

[16] C.E.Cohen et al. Flight test results of autocoupled approaches using GPS and integrity beacons. *ION GPS-94, Salt Lake City, Utah*, September 1994.

190

[17] C.E.Cohen et al. Real time flight testing using integrity beacons for GPS category III precision landing. *NAVIGATION: Journal of the Institute of Navigation*, 41(2), July 1994.

[18] E.G. Lightsey et al. Applications of gps attitude determination to gravity gradient stabilized spacecraft. *AAIA GNC, AIAA Paper93-3788, Monterey, CA*, August 1993.

[19] M.Rabinowitz et al. A system using leo telecommunication satellites for rapid acquisition of integer cycle ambiguities. *IEEE PLANS 98*, April 1998.

[20] G.H. Golub and C.F. van Loan. *Matrix Computations*. Johns Hopkins University Press, 3rd edition, 1996.

[21] J.Aarons. Global morphology of ionospheric scintillations. *Proceedings of the IEEE*, 70(4):360–378, 1982.

[22] A.J. Van Dierendonck J.J. Spilker Jr. Proposed new civil gps signal at 1176.45 mhz. *Proceedings of ION GPS99*, pages 1717–1725, 1999.

[23] B.W. Parkinson J.J. Spilker Jr., E.H. Martin. A family of split spectrum gps civil signals. *Proceedings of ION GPS98*, pages 1905–1914, 1998.

[24] J.Jung. High integrity carrier phase navigation for future laas using multiple civilian gps signals. *Proceedings of ION-GPS 1999*, pages 727–736, September 1999.

[25] J.P.McCLure and W.B.Hansen. A catalog of ionospheric F region irregularity based on OGO-6 retarding potential analyzer data. *Journal of Geophysical Research*, 78:7431, 1973.

[26] J.J. Spilker Jr. Tropospheric effects on GPS. *Global Positioning System: Theory and Applications*, pages 517–546, 1996.

[27] R.E. Kalman and R.S. Bucy. New results in linear filtering and prediction. *ASME Transactions, Journal of Basic Engineering*, 83:95–108, 1961.

[28] K.C.Yeh and C.H. Liu. Radio wave scintillations in the ionosphere. *Proceedings of the IEEE*, 70(4):pp 324–359, 1982.

[29] T.H. Lee. *The Sesign of CMOS Radio-Frequency Integrated Circuits*. Cambridge University Press, 1 edition, 1998.

[30] E.G. Lightsey. Spacecraft attitude control using gps carrier phase. *AIAA: Global Positioning System: Theory and Applications*, 2, 1995.

[31] S.A. Long and M.D. Walton. a dual-frequency stacked circular disc antenna. *IEEE Transactions on Antennas and Propagation*, AP-27:270–273, March 1979.

[32] B.W.Parkinson M.Rabinowitz, C.E.Cohen and J.J.Spilker. Some capabilities of a joint gps-leo navigation system. *Proceedings of the Institute of Navigation ION GPS-2000*, September 2000.

[33] B.W.Parkinson M.Rabinowitz, K.Gromov and C.E.Cohen. Architectures for joint gps/leo satellite carrier phase receivers designed for rapid robust resolution of carrier cycle ambiguities on mobile platforms. *Proceedings of the Institute of Navigation ION GPS-2000*, September 2000.

[34] C.E.Cohen M.Rabinowitz and B.W.Parkinson. The application of leos to cycle anbiguity resolution on navstar transmissions for kinematic carrier-phase positioning. *Institute of Navigation, ION97*, 1(1), September 1997.

192

[35] C.E.Cohen M.Rabinowitz and B.W.Parkinson. Patent application: Resolving integer cycle ambiguities with LEO satellites. Technical Report 60/041,184, Application: US Patent and Trademark Office, March 1998.

[36] M.Moeglein N.Krasner. An introduction to snaptrack server-aided gps technology. *Proceedings Of IONGPS98*, pages 333–342, 1999.

[37] A.V. Oppenheim and R.W.Schafer. *Discrete-Time Signal Processing*. Prentice-Hall, Inc., 1989.

[38] B.W. Parkinson. GPS error analysis. *Global Positioning System: Theory and Applications*, 1:469–483, 1994.

[39] B.W. Parkinson and P. Axelrad. Autonomous integrity monitoring using the pseudorange residual. *Navigation: Journal of the Institute of Navigation*, 35(2), 1988.

[40] B.W. Parkinson and P.K. Enge. Differential gps. *Differential GPS*, 1:3–50, 1995.

[41] B.W. Parkinson and J.J. Spilker Jr. Gps operation and design. *Global Positioning System: Theory and Applications*, 1:29–56, 1995.

[42] P.F.Macdoran and D.J.Spitzmesser. *US Patent no. 4,797,677: Method and Apparatus for Deriving Pseudo Range for Earth Orbiting Satellites*. US Patent: Istac, Incorporated, January 1989.

[43] D.M. Pozar. *Microwave Engineering*. John Wiley and Sons, 2nd edition, 1998.

[44] J.G. Proakis. *Digital Communications*. McGraw-Hill, 3nd edition, 1995.

[45] R.R.Hatch. *US Patent no. 4,963,889: Method and Apparatus for Precision Attitude Determination and Kinematic Positioning.* Magnavox Government and Industrial Electronics Company, October 1989.

[46] S.Lindsey and M.Simon. *Telecommunications Systems Engineering.* Prentise-Hall, 1973.

[47] R.F. Stengel. *Optimal Control and Estimation,* volume 1. Dover Publications, Inc., 1994.

[48] T.P.Yunck. Orbit determination. *Global Positioning System: Theory and Applications,* 2:pp 559–592, 1995.

[49] A.J van Dierendonck. GPS receivers. *Global Positioning System: Theory and Applications,* 1:329–408, 1995.

[50] J.R. Wertz. *Spacecraft attitude determination and control.* D.Reidel Publishing Company, 1985.

[51] G.W. Torrence W.J. Vogel. Propagation measurements for satellite radio reception inside buildings. *IEEE Transactions on Antennas and Propagation,* 41(7):954–961, July 1993.

[52] H.P. Lin W.J. Vogel, G.W. Torrence. Slant-path building penetration measurements at l- and s-band. Technical Report EERL Technical Report EERL-95-301, The University of Texas, Electrical Engineering Research Laboratory, 1995.

[53] J. Goldhirsh W.J. Vogel. Propagation effects for land mobile satellite systems: Overview of experimental and modeling results. Technical Report Reference Publication 1274, NASA, 1992.

[54] H.P.Lin W.J.Vogel, G.W.Torrence. Into building fading at l- and s-band for satellite pcs. *Proceedings of the Nineteenth NASA Propagation Experimenters Meeting (NAPEX XIX) and the Seventh Advanced Communications Technology Satellite (ACTS) Propagation Studies Workshop (APSW VII), (JPL Publication 95-15), Fort Collins, Colorado*, June 1995.

[55] S.S. Zhong and Y.T. Lo. Single element rectangular microstrip antenna for dual freqeuncy operation. *Electronics Letters*, 19:pp 298–300, 1983.